

Measurement of Spin Correlation in Dileptonic Top Quark Pair Decays with the CMS Experiment

Von der Fakultät für Mathematik, Informatik und
Naturwissenschaften der RWTH Aachen University zur Erlangung
des akademischen Grades eines Doktors der Naturwissenschaften
genehmigte Dissertation

vorgelegt von

Diplom-Physiker Felix Höhle

aus Wuppertal

Berichter: Univ.-Prof. Dr. rer. nat. Achim Stahl

Univ.-Prof. Dr. rer. nat. Werner Bernreuther

Tag der mündlichen Prüfung: 2. Juli 2015

Diese Dissertation ist auf den Internetseiten der
Universitätsbibliothek online verfügbar.

*Gewidmet meiner Mutter,
Gisela Höhle.*

Kurzfassung

Der Large Hadron Collider am Forschungszentrum CERN bei Genf ist zur Zeit der leistungsfähigste Teilchenbeschleuniger der Welt. Im Jahr 2011 erreichten die Proton-Proton-Kollisionen eine Schwerpunktsenergie von $\sqrt{s} = 7 \text{ TeV}$ bei einer instantanen Luminosität von bis zu $\mathcal{L} = 4,07 \cdot 10^{33} \text{ cm}^{-2}\text{s}^{-1}$. Das CMS Experiment zeichnete bei dieser Schwerpunktsenergie eine integrierte Luminosität von $\mathcal{L}_{\text{int}} = 5,55 \text{ fb}^{-1}$ auf, welche einer Menge von ungefähr 850.000 Top-Quark-Paar Ereignissen entspricht. Diese werden überwiegend durch Gluon-Gluon-Fusion erzeugt, die Top-Quark-Paare mit gleichem Spin bevorzugt. Daher ergibt sich eine von Null verschiedene Asymmetrie für die Anzahl der Top-Quark-Paare mit gleichem und ungleichem Spin. Aufgrund der sehr kurzen Lebensdauer der Top-Quarks zerfallen diese bevor sie hadronisieren. Daher werden die Spin-Eigenschaften nicht verwaschen und die anfängliche Helizität der Top-Quarks hat Einfluß auf die kinematischen Größen der Zerfallsprodukte. Verteilungen, die aus den kinematischen Variablen der Zerfallsprodukte gebildet werden, sind deswegen abhängig von der Asymmetrie der Top-Quark-Spins. Die Standardmodell Vorhersage für diese Asymmetrie beträgt $A_{\text{SM}} = 0,31$. Eine sensitive Variable für Spin-Korrelationen ist die Differenz des Azimuts, $\Delta\phi$, der Leptonen in dileptonischen Top-Quark-Paar Zerfällen. Diese Arbeit präsentiert eine Messung der Asymmetrie A , die mit der Standard Modell Vorhersage verglichen wird. Die Messung wird anhand der in 2011 vom CMS Experiment aufgezeichneten und validierten Proton-Proton-Kollisionen durchgeführt, welche einer integrierten Luminosität von $5,0 \text{ fb}^{-1}$ entsprechen. Es werden Top-Paar-Zerfälle betrachtet, wobei das Top-Quark über ein W Boson schwach in ein Elektron oder Myon zerfällt. Mit Hilfe einer optimierten Selektion werden diese Ereignisse aus den aufgezeichneten Daten selektiert und insgesamt 11.638 Ereignisse nach dieser Selektion analysiert. Untergrund Prozesse werden mit Hilfe von Monte Carlo Generatoren und Daten basierten Methoden abgeschätzt und modelliert. Die $\Delta\phi$ Verteilung der selektierten Ereignisse wird mittels eines Template Fits untersucht, der die Ähnlichkeit zur Standardmodell Erwartung und einem alternativen Modell mit verschwindender Spin-Korrelation, $A = 0$, ermittelt. Anschließend werden verschiedene systematische Unsicherheiten betrachtet und deren Einfluss auf die Messung abgeschätzt. Als finales Ergebnis wird eine Asymmetrie von $A = 0,24 \pm 0,03 \text{ (stat.)} \pm 0,07 \text{ (sys.)}$ in Daten gemessen, die innerhalb der Unsicherheiten mit der Standardmodell Erwartung vereinbar ist.

Abstract

The Large Hadron Collider close to Geneva is the world most powerful particle accelerator with a center of mass energy of $\sqrt{s} = 7 \text{ TeV}$ and providing instantaneous luminosity of up to $\mathcal{L} = 4.07 \cdot 10^{33} \text{ cm}^{-2}\text{s}^{-1}$ during 2011. The CMS experiment recorded during this run period a dataset of an integrated luminosity of $\mathcal{L}_{\text{int}} = 5.55 \text{ fb}^{-1}$ corresponding to 850,000 top quark pair events. These are predominantly produced by gluon-gluon fusion preferring top quark pairs with same spin. Therefore, the spin directions of top quark pairs are correlated and the asymmetry between the number of top quark pairs with same and not same spin is not vanishing. The top quarks decay before hadronization takes place due to their high mass. Hence, the kinematics of their decay products are influenced by their helicity and the initial spin asymmetry is accessible via their decay products. The Standard Model predicts an asymmetry of $A_{\text{SM}} = 0.31$ for proton-proton collisions at $\sqrt{s} = 7 \text{ TeV}$. The difference of the azimuth, $\Delta\phi$, of the two leptons in dileptonic top quark pair decays is sensitive to spin correlations and provides access to the asymmetry.

This thesis presents a measurement of the asymmetry A and tests its Standard Model prediction. The 2011 dataset of proton-proton collisions is investigated. The data contains validated collisions corresponding to an integrated luminosity of 5.0 fb^{-1} . The asymmetry is extracted from top quark pair events, which decay electroweak into electrons and muons as signal signature. The signal event yield is enriched by an optimized selection with a final set of 11,638 candidate signatures. Event yields and differential distributions of background processes are modeled by Monte Carlo methods and normalized by data-driven methods. The obtained $\Delta\phi$ distribution of the selected events is investigated by a template fit, which quantifies the similarity to Standard Model expectation and a model of vanishing spin correlation. Finally, the influence of several systematic uncertainties on the measurement is studied. An asymmetry of $A = 0.24 \pm 0.03 \text{ (stat.)} \pm 0.07 \text{ (sys.)}$ is measured in data, which is compatible with the Standard Model expectation within the given uncertainties.

Contents

1	Introduction	1
2	Theory	3
2.1	The Standard Model of Particle Physics	3
2.2	Top Quark Physics	4
2.2.1	Top Quark Pair Production	4
2.2.2	Top Quark Decay	8
2.3	Spin Correlation Observables in Top Quark Pairs	11
3	The CMS Detector and the Large Hadron Collider	15
3.1	The Large Hadron Collider	15
3.2	The CMS Detector	18
3.2.1	The CMS Coordinate Conventions	19
3.2.2	The CMS Tracking System	19
3.2.3	The Calorimeters	21
3.2.4	The Solenoid	24
3.2.5	The Muon System	24
3.2.6	The Trigger System	25
3.2.7	Luminosity Measurement	26
4	Collision Data and Event Simulation	27
4.1	Collision Data	27
4.2	Event Simulation	27
4.2.1	Matrix Element Generators	27
4.2.2	Detector Simulation	28
4.2.3	Pile-up Simulation	28
4.3	Top Quark Event Simulation	29
4.3.1	Matrix Element Generators	29
4.3.2	Non Standard Model Spin Correlation Production	30
4.3.3	Systematic Top Samples	30
4.3.4	Validation of private samples	31

5	Event Reconstruction	33
5.1	Muons	34
5.2	Electrons	34
5.3	Jets	35
5.3.1	The Anti- k_T Algorithm	36
5.3.2	Jet Energy Corrections	36
5.3.3	b -Tagging	37
5.4	Missing transverse energy	38
5.5	Particle Flow	38
6	Selection	39
6.1	Background Processes	39
6.1.1	QCD Processes	39
6.1.2	W Boson Processes	40
6.1.3	Drell-Yan Processes	41
6.1.4	Diboson Processes	41
6.1.5	Single Top Processes	41
6.2	Object Selection	42
6.2.1	Selection of muons	42
6.2.2	Selection of electrons	43
6.2.3	Selection of jets	44
6.2.4	Selection in Transverse Missing Energy	44
6.3	Event selection	44
6.3.1	Trigger selection	45
6.3.2	Lepton pair selection	45
6.3.3	Jet and MET selection	45
6.4	Applied Monte Carlo Corrections	45
6.4.1	Pile-up Reweighting procedure	46
6.4.2	Lepton trigger and identification efficiency	47
6.5	Data-driven Background Estimation	47
6.5.1	Drell-Yan background estimation	47
6.5.2	Fake lepton estimate	50
6.6	Distortion of Spin Correlation Effects by the Selection	51
6.7	Comparison of Data and Monte Carlo Simulation	51
7	Spin Correlation Extraction	61
7.1	Applied Template Fit	61
7.1.1	Fit Function and Templates	61
7.1.2	Technical Implementation	63
7.2	Template Fit Validation	63
7.3	Template Fit Result	66

8	Systematic Uncertainties	69
8.1	Tau Polarization Modeling	71
8.2	Result of Systematic Uncertainties	76
9	Conclusion	79
10	Outlook	83
A	Samples and Datasets	85

Chapter 1

Introduction

In November 2009 a new era of high energy physics began with the start of the Large Hadron Collider (LHC) at CERN. The LHC provides proton-proton collisions with an energy at the terascale. The enormous luminosity puts processes with a relatively small cross section, like the top quark pair production, in a reachable experimental range. The large amount of data, collected by the Compact Muon Solenoid (CMS) experiment, provides the opportunity to study rare interactions or particle properties in great detail. Due to the high collision energy of several TeV and bright luminosity, the LHC provides collisions containing top quarks nearly every second. With such a high rate of top quark events a detailed study of the top quark properties is possible. Furthermore, an investigation of the spin properties especially of top quark pairs is reachable for the first time. At LHC's collision energies the Standard Model predicts a not vanishing correlation of roughly 30 % between the individual spins of a top quark pair. This spin correlation is measurable by angular observables of the top quark pair decay products. The study of these angular observables is a strong test of the Standard Model since top quark pairs are produced by perturbative QCD reactions and subsequently decay electroweak. Furthermore, several beyond the Standard Model (BSM) models impose significant deviations in angular distributions and a relevant difference from the Standard Model expectation could eventually uncover new physics.

This analysis presents a first measurement of top quark spin correlations at $\sqrt{s} = 7 \text{ TeV}$ using the dileptonic decay channel with data recorded by the CMS experiment. A dedicated simulation strategy is developed in order to model top quark pair events with uncorrelated top quark spins. This scenario is needed to test the collected data against a non Standard Model expectation of spin correlations. A dedicated dileptonic selection is presented, optimized and validated. This selection considers the dileptonic top quark pair decay modes containing an ee -, $e\mu$ - or $\mu\mu$ -pair as corresponding signal channels. Contributions of background processes are challenging to estimate, since the corresponding cross sections are large and moreover, the rejection rate of the analysis exceeds the available statistics by several orders of magnitude. Thus, data-driven techniques are applied to model the background event yields. Processes mimicking additional leptons

like QCD processes and events containing a W boson are modeled by a matrix element technique. Furthermore, the Drell-Yan contribution is estimated via a method, which investigates the Z resonance. The spin correlation strength is extracted by a simultaneous template fit in the three signal channels. The collected data is examined with a scenario corresponding to Standard Model expectation and an alternative scenario assuming uncorrelated top quark spins. The fit estimates globally the ratio of these two hypotheses in all signal channels simultaneously. Furthermore, common and dominant systematic uncertainties are considered and their influence on the measurement is investigated.

A short summary of the Standard Model and a more detailed description of top quark physics and top quark spin correlation is given in Chapter 2. The experimental setup of LHC and the CMS experiment are described in Chapter 3. Details of the investigated collision data and event simulation are outlined in Chapter 4 followed by a summary of reconstructed physics objects used in this analysis, given in Chapter 5. Chapter 6 describes the applied selection and estimation of background event yields. In Chapter 7 the applied template fit, its validation and the obtained result are discussed. The uncertainties of the measurement are estimated in Chapter 8 and the relevant results of this analysis are summarized in Chapter 9. Parts of this analysis have been published in [126] as a conference report of the Physics Analysis Summary [127].

This analysis uses natural units, as it is common practice in particle physics. Therefore, $\hbar = c = 1$. In this convention the commonly used units are:

$$[\text{Energy}] = [\text{Mass}] = [\text{Momentum}] = [\text{Time}]^{-1} = [\text{Length}]^{-1} = \text{eV} \quad .$$

Chapter 2

Theory

The theory of particle physics was developed in the early 20th century starting with quantum mechanics and relativity. In the early 1960s Gell-Mann introduced the eight-fold way [1] which led to the Standard Model of particle physics [2]. In general, the Standard Model is a quantum field theory and one of the most important achievements in particle physics during the 20th century. This chapter introduces the Standard Model of particle physics and closes with a more detailed discussion of spin correlation of top quark pair events.

2.1 The Standard Model of Particle Physics

The Standard Model is a quantum field theory and describes subatomic processes and couplings in great detail and is validated by numerous high precision measurements. The prediction of a second and third generation of quarks and leptons and their later experimental confirmation by the Stanford Linear Accelerator Center [3, 4] was one of its greatest achievements in the 20th century. The later discovery of the Z and W bosons by the UA1 [5, 6] and UA2 [7, 8] experiment at CERN led to a broad acceptance in the scientific community. The Standard Model assumes that all matter consists of fermions, which interact via three forces. These forces are described by four types of exchange particles, which are bosons, see Table 2.1. There are each six fermions and quarks, which have each an antiparticle with negative additive quantum numbers and same properties like spin and mass. Their properties are shown in Table 2.2. Each interaction is related to a corresponding charge: color for the strong interaction, electromagnetic charge q_{el} .

Table 2.1: The three interaction forces and their corresponding bosons.

boson	interaction	distance [m]	spin [\hbar]	$q_{\text{el.}}$ [e]	mass [GeV/c^2]
photon γ	electromagnetic	∞	1	0	0
W^\pm/Z	weak	$\ll 10^{-16}$	1	$\pm 1, 0$	$\approx 80.4/91.2$
8 gluons	strong	10^{-15}	1	0	0

Table 2.2: The three generations of the Standard Model denoted by I, II and III. Electromagnetic charge Q , weak isospin T_3 and the hypercharge Y . These three quantities are related via the Gell-Mann-Nishijima formula, $Q = T_3 + Y/2$, see [9]. Antiparticles are not shown.

fermions	I	II	III	$Q [e]$	T_3	Y	color
quarks	$\begin{pmatrix} u \\ d \end{pmatrix}_L$	$\begin{pmatrix} c \\ s \end{pmatrix}_L$	$\begin{pmatrix} t \\ b \end{pmatrix}_L$	2/3	1/2	1/3	rgb
	u_R	c_R	t_R	-1/3	-1/2	1/3	rgb
	d_R	s_R	b_R	2/3	0	4/3	rgb
				-1/3	0	2/3	rgb
leptons	$\begin{pmatrix} \nu_e \\ e \end{pmatrix}_L$	$\begin{pmatrix} \nu_\mu \\ \mu \end{pmatrix}_L$	$\begin{pmatrix} \nu_\tau \\ \tau \end{pmatrix}_L$	0	1/2	-1	-
	$\nu_{e,R}$	$\nu_{\mu,R}$	$\nu_{\tau,R}$	-1	-1/2	-1	-
	e_R	μ_R	τ_R	0	0	0	-
				-1	0	-2	-

for the electromagnetic interaction and the weak isospin T_3 for the weak interaction. Considering the weak interaction fermions are arranged in left-handed isospin doublets and two right-handed isospin singlets. The mathematical formalism is a combined symmetry group of $SU(3)_C \otimes SU(2)_L \otimes U(1)_Y$. Quarks and leptons can be transformed to their mass eigenstates using the Cabibbo-Kobayashi-Maskawa (CKM) matrix and Maki-Nakagawa-Sakata (MNS) matrix respectively. The electroweak exchange particles W^\pm and Z are massive in contrast to photons and gluons. The measured masses especially of the top quark, W and Z boson are introduced by a spontaneous symmetry breaking of the electroweak symmetry group with the Higgs field [10, 11, 12]. The recent discovery of a Higgs boson like particle [13, 14] confirms this mechanism.

2.2 Top Quark Physics

This section summarizes the key properties of top quarks, their production and decay. With a mass of $m_{\text{top}} = 173.34 \pm 0.27 \text{ (stat.)} \pm 0.71 \text{ (syst.) GeV}$ [15], which is similar to the mass of a gold nucleus, top quarks are the most massive elementary particles. A detailed description of its production and decay is given in two dedicated subsections and in [16, 17].

2.2.1 Top Quark Pair Production

At the LHC top quark pairs are produced by proton-proton collisions. In 2011 the proton beams collided with $\sqrt{s} = 7 \text{ TeV}$ and produced a large variety of physics processes, see Figure 2.1.

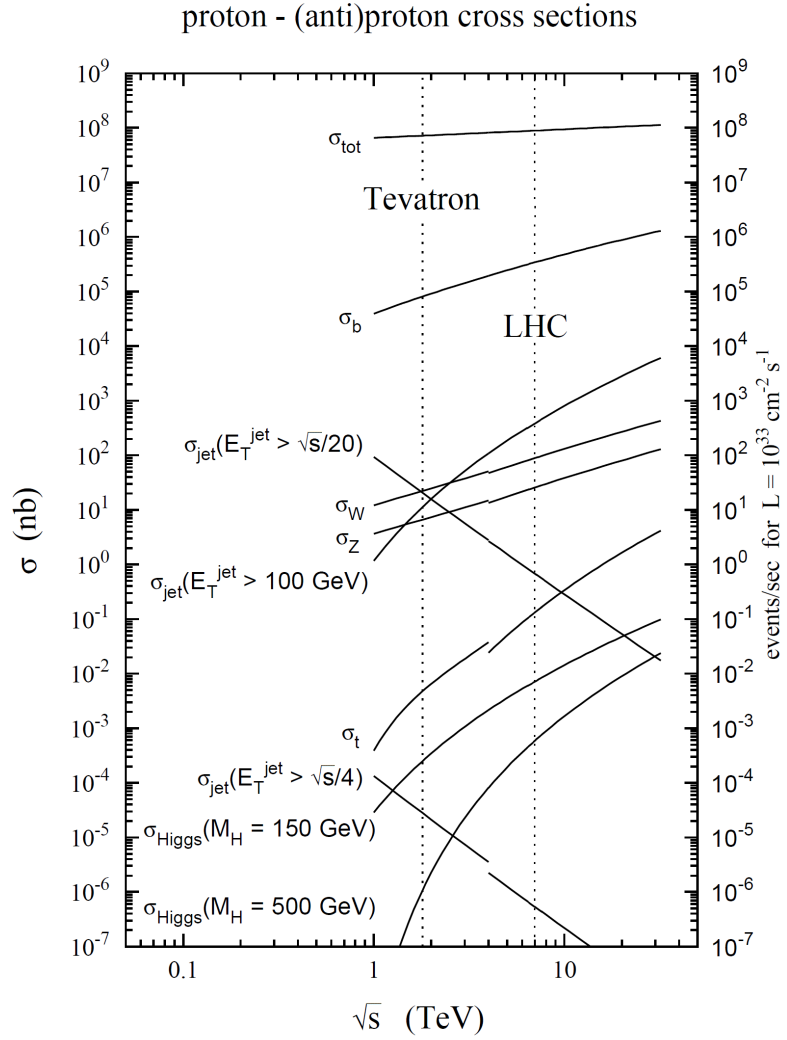


Figure 2.1: The total proton-(anti)proton cross section and production cross sections of selected final states, like b and t quark production, based on [18]. The dashed lines indicate the center of mass energies of Tevatron, $\sqrt{s} = 1.96 \text{ TeV}$, and LHC, $\sqrt{s} = 7 \text{ TeV}$, in 2011.

Due to the substructure of each proton, in every collision the participating proton constituents, called partons, have a different total proton momentum fraction x resulting in a unique momentum transfer Q . The probability of a parton to carry a specific fraction x_i of the total proton momentum is given by the parton density function (PDF) $f_i(x_i, Q^2)$. These probabilities are strongly dependent on the type of parton, see Figure 2.2. Therefore, several parton-parton or gluon interactions are possible resulting in a large variety of processes.

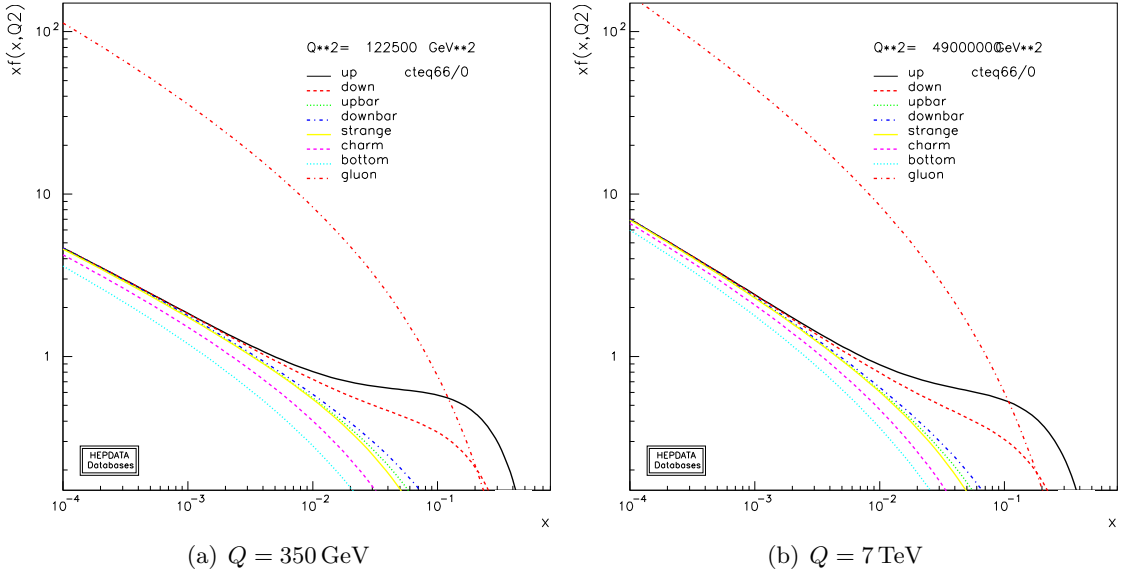


Figure 2.2: PDFs shown in terms of $xf(x, Q^2)$ for a resolution scale of $Q^2 = (350 \text{ GeV})^2$, see a) and $Q^2 = (7 \text{ TeV})^2$ see b). The PDF estimations are generated by the Durham HEP Databases [19].

A selection of electroweak processes are shown in Figure 2.3. These dilute the top quark events and are discussed in Chapter 6. The cross section of some similar processes and/or dominant processes are listed in Figure 2.1. With the assumption $x_1 = x_2$, a minimal momentum fraction $x_{1,2} = 2.5\%$ at $\sqrt{s} = 7 \text{ TeV}$ is necessary to produce a top quark pair. The probability density for gluons dominates all other probability density functions, see Figure 2.2. In total, roughly 80% of the top quark pairs are produced by gluon-gluon fusion and 20% by quark-antiquark annihilation [16, p. 668]. The different production channels are shown in Figure 2.4 and Figure 2.5. The matrix elements for these production channels, averaged and summed over the spins and colors of the initial and final partons, are derived with the Feynman rules and the following equations are

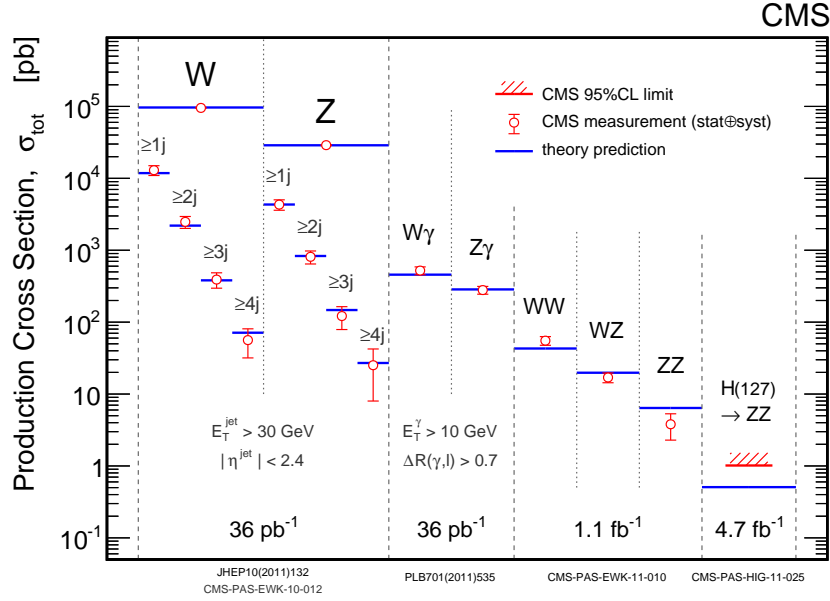


Figure 2.3: Electroweak cross sections measured by the CMS experiment using different integrated luminosities at $\sqrt{s} = 7 \text{ TeV}$ [20].

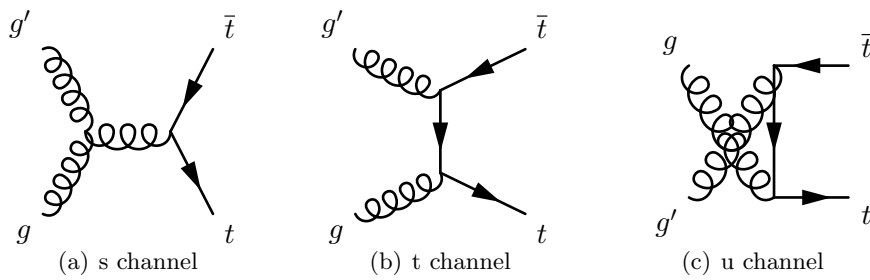


Figure 2.4: Top quark pair production Feynman graphs for gluon-gluon fusion.

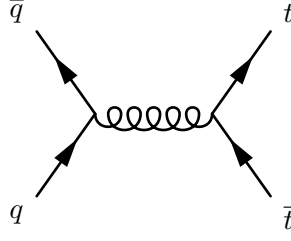


Figure 2.5: Quark-antiquark annihilation.

obtained:

$$\begin{aligned}
 |\overline{\mathcal{M}}|^2(gg \rightarrow t\bar{t}) &= (4\pi\alpha_S)^2 \left(\frac{(p_1 + p_2)^4}{24(p_1 \cdot p_3)(p_2 \cdot p_3)} - \frac{3}{8} \right) \\
 &\quad \cdot \left(4 \frac{(p_1 \cdot p_3)^2 + (p_2 \cdot p_3)^2}{(p_1 + p_2)^4} + \frac{4m_t^2}{(p_1 + p_2)^2} - \frac{m_t^4(p_1 + p_2)^4}{(p_1 \cdot p_3)^2(p_2 \cdot p_3)^2} \right), \\
 |\overline{\mathcal{M}}|^2(q\bar{q} \rightarrow t\bar{t}) &= (4\pi\alpha_S)^2 \frac{8}{9} \left(2 \frac{(p_1 \cdot p_3)^2 + (p_2 \cdot p_3)^2}{(p_1 + p_2)^4} + \frac{m_t^2}{(p_1 + p_2)^2} \right),
 \end{aligned}$$

where p_1 and p_2 , and p_3 and p_4 correspond to the momenta of the initial and final partons, respectively. These different production channels do not produce all helicity states of top quark pairs equally. The gluon-gluon fusion channel produces nearly exclusively top quark pairs with top quarks of the same helicity state up to an invariant mass of roughly $m_{t\bar{t}} = 800 \text{ GeV}$, see Figure 2.6. The dominance of the gluon-gluon fusion and the suppressed probability of $m_{t\bar{t}} > 800 \text{ GeV}$ leads to a dominant production of top quark pairs with the same helicity. Therefore, the Standard Model expects an inequality of helicity states of top quark pairs, which motivates the investigation of spin correlations. More details are given in the following Section 2.3. In total all these production mechanisms add up to a total top quark pair production cross section of $\sigma_{pp \rightarrow t\bar{t}} = 161.9 \pm 2.5 \text{ (stat.)} \pm 5.1 \text{ (syst.)} \pm 3.6 \text{ (lumi.) pb}$ [22, 23]. Figure 2.7 shows an overview of the top quark pair cross section for different \sqrt{s} .

2.2.2 Top Quark Decay

Top quarks decay predominantly weak into a W boson and b quark. The branching ratio of this decay is given in the Standard Model by the ratio of CKM matrix elements:

$$B_{W,b} = \frac{|V_{tb}|^2}{|V_{tb}|^2 + |V_{ts}|^2 + |V_{td}|^2} = |V_{tb}|^2 = 99.82\%, \quad (2.1)$$

assuming three quark families, the unity of the CKM matrix and using $V_{tb} = 0.9991$, see [16, Eq. 11.27]. The top decay width is given by:

$$\Gamma(t \rightarrow bW) = \frac{G_F m_t^3}{\sqrt{2} 8\pi} \left(1 - \frac{m_W^2}{m_t^2} \right)^2 \left(1 + 2 \frac{m_W^2}{m_t^2} \right), \quad (2.2)$$

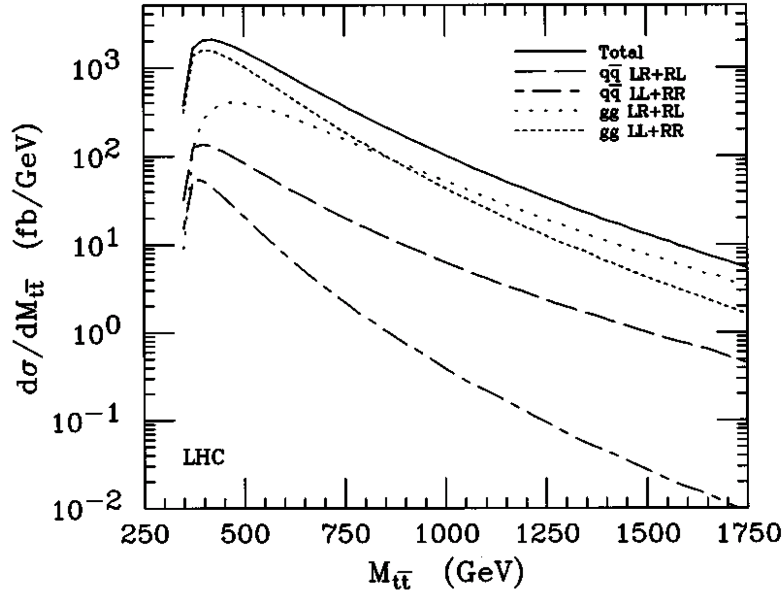


Figure 2.6: Top quark pair production helicity states for quark-antiquark annihilation and gluon-gluon fusion [21, Fig. 4].

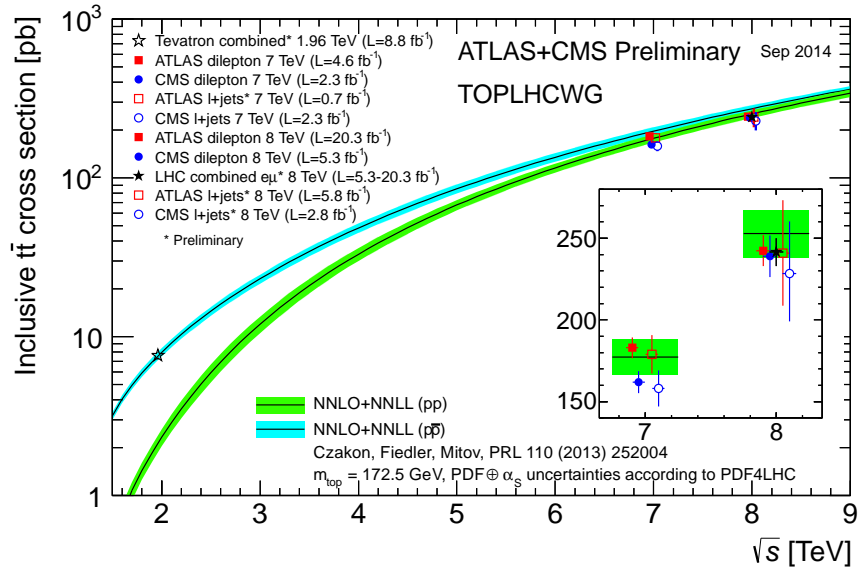


Figure 2.7: The top quark pair production cross section for proton-proton and proton-antiproton collisions depending on the center of mass energy \sqrt{s} [22, 24].

neglecting the b quark mass and considering only the lowest order of perturbation theory. Inserting its high mass a very short lifetime of $\tau_t = 4.2 \cdot 10^{-25} \text{ s}$ is obtained, which is significantly smaller than the hadronization time of $\tau_{\text{had.}} \approx 1/\Lambda_{\text{QCD}} \approx 10^{-23} \text{ s}$ [17]. The time scale needed for depolarization of the top quark spin, which is of the order $m_t/\Lambda_{\text{QCD}}^2 \gg 1/\Gamma_t$, implies the transmission of the polarization to its decay products [17]. The top quark decays are classified according the subsequent W boson decays. A decay is

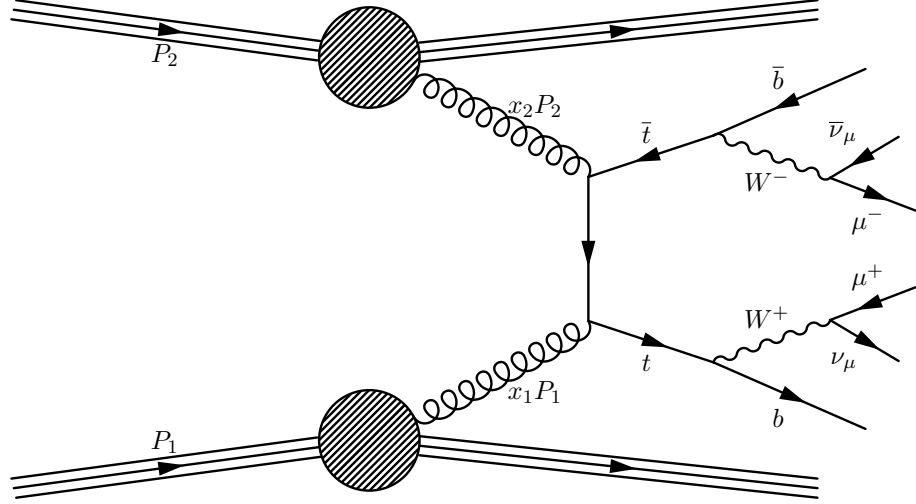


Figure 2.8: A dileptonically decaying top pair produced by gluon-gluon fusion in a proton-proton collision.

called leptonic if the resulting W boson decays into a lepton and neutrino, and hadronic is defined respectively by a decay into quarks. All relevant Standard Model decays of a top quark pair are listed in Table 2.3. These possible decay channels are subdivided in three groups: full hadronic, semileptonic and dileptonic, respectively to the combination of W boson decays. An example of a dileptonic decay of a top quark pair produced in proton-proton collisions is given in Figure 2.8. This dileptonic decay channel provides a bright signature with two high energy leptons and a reasonable branching ratio of $B_{\text{dilep.}} = 11 \%$. An improvement in statistics and a reasonable signature has the semileptonic channel with only one high energy lepton and a branching ratio of $B_{\text{semilep.}} = 44 \%$. The full hadronic decay has the same branching ratio but its signature is very similar to processes from hadronic interactions, called QCD processes, see also Section 6.1.1, and therefore, hard to distinguish from the huge backgrounds, see Figure 2.1. This analysis focuses on the dileptonic channel with muons and electrons in the final state. The final states containing τ leptons are not considered as signal in this analysis. Hadronically decaying τ leptons have a similar signature to QCD processes and leptonic τ decays introduce an additional neutrino. Requiring a full kinematic reconstruction of a top quark pair event these neutrinos lead to several ambiguities of kinematic event reconstructions. Hence, top quark pair decays to one or two τ leptons are classified as additional top

Table 2.3: Decay channels and branching ratios of top quark pair events derived from [16].

$t\bar{t} \rightarrow W^+ b \quad W^- \bar{b}$			W^+ decay				
			$e^+ \nu_e$	$\mu^+ \nu_\mu$	$\tau^+ \nu_\tau$	$u\bar{d}$	$c\bar{s}$
			1/9	1/9	1/9	3/9	3/9
W^- decay	$e^- \bar{\nu}_e$	1/9	1/81	1/81	1/81	3/81	3/81
	$\mu^- \bar{\nu}_\mu$	1/9	1/81	1/81	1/81	3/81	3/81
	$\tau^- \bar{\nu}_\tau$	1/9	1/81	1/81	1/81	3/81	3/81
	$\bar{u}d$	3/9	3/81	3/81	3/81	9/81	9/81
	$\bar{c}s$	3/9	3/81	3/81	3/81	9/81	9/81

quark pair background. Therefore, the total fraction of top quark pair events considered as signal events has a branching ratio $B_{t\bar{t}\text{signal}} = 4.94\%$ resulting in a signal cross section of $\sigma_{\text{signal}} = 8.00 \text{ pb}$. Since this analysis investigates an integrated luminosity of $\mathcal{L}_{\text{int}} = 5.0 \text{ fb}^{-1}$, the total amount of signal events in data is expected to be roughly 40,000.

2.3 Spin Correlation Observables in Top Quark Pairs

The Standard Model predicts a preferred top-quark-pair production, where the t and \bar{t} have the same helicity. An according asymmetry between the two possible helicity states is defined as:

$$A = \frac{N(\text{LL} + \text{RR}) - N(\text{RL} + \text{LR})}{N(\text{LL} + \text{RR}) + N(\text{RL} + \text{LR})} \quad (2.3)$$

where R and L denote the helicity state of one of the top quarks. Close to the production threshold of nearly 350 GeV the top quark pair system is predominantly generated by gluon-gluon fusion via its 1S_0 state, and by the 3S_1 state of quark-antiquark annihilation, see Figure 2.6. The 1S_0 state of gluon-gluon fusion prefers same helicity state top-quark pairs, where the spins tend to be antiparallel, while considering the quark-antiquark annihilation's 3S_1 state opposite helicities are favored. The Standard Model (SM) expects at $\sqrt{s} = 7 \text{ TeV}$ an asymmetry of $A = 0.31$ in pp collisions, see [25, Table 1]. The measurement of the ATLAS collaboration [26] is in agreement with this expectation and also previous measurements of the DZero (D0) [27] and Collider Detector at Fermilab (CDF) [28] experiment at Tevatron confirm the theoretical calculations. The lacking hadronization and the conserved angular momentum in decays transfers the initial spin information of the decaying top quarks to their daughter particles. The kinematic properties of the resulting W boson and b quark and their subsequential decay products are

Table 2.4: The spin-analyzing power, κ_i , of the different top-quark-decay products [29]. Antiparticles have the opposite sign.

f	l^+, \bar{d}, \bar{s}	ν_l, u, c	b	W
κ_f	1	-0.31	-0.41	0.41

correlated to the initial top quark spin. Therefore, a measurement of the kinematic properties of the top-quark decay particles is able to test the prediction of spin correlation in top quark pair events.

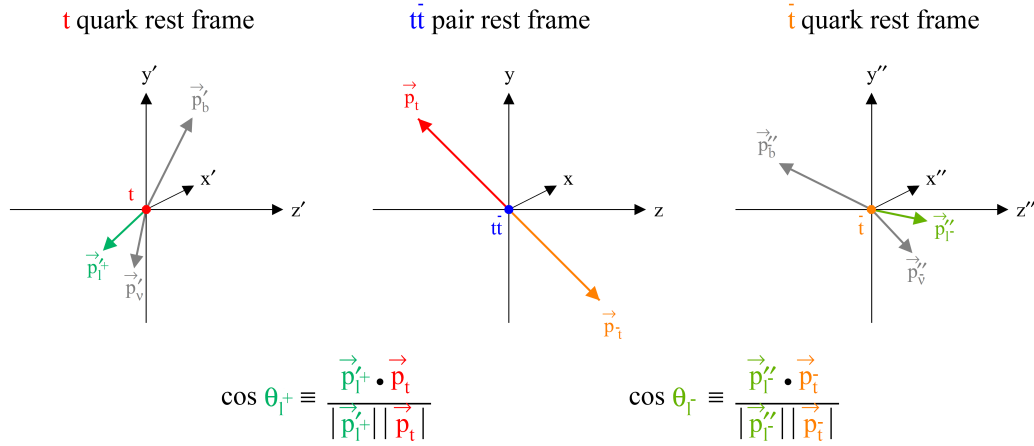
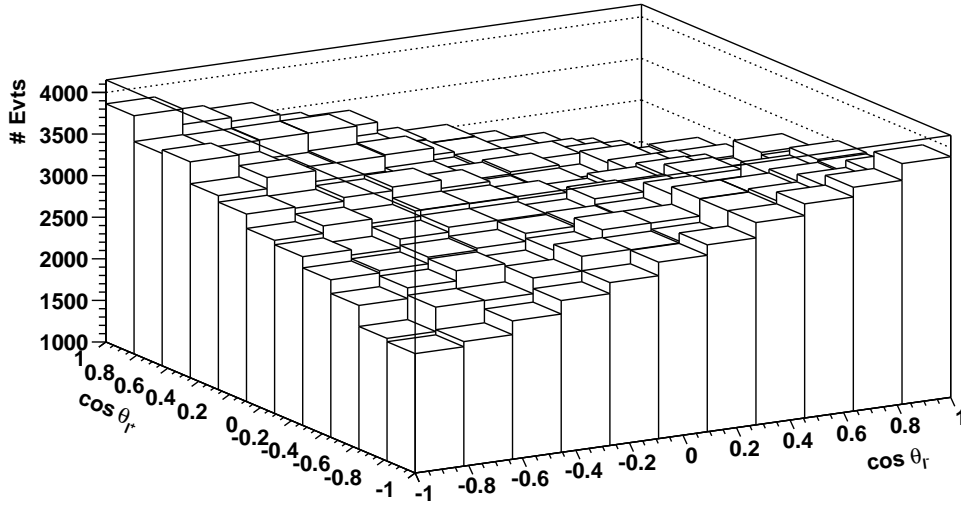
Within this analysis two angular distributions are used as spin correlation variables. The intrinsic top-pair-spin correlation of the simulated samples is tested by the double differential distribution of $\cos \theta_1$ and $\cos \theta_2$:

$$\frac{1}{\sigma} \frac{d\sigma}{d \cos(\theta_1) d \cos(\theta_2)} = \frac{1}{4} \left(1 + A \kappa_1 \kappa_2 \cos(\theta_1) \cos(\theta_2) \right) . \quad (2.4)$$

The two analyzer factors, κ_1 and κ_2 , denote the spin information content of the top quark decay particles, see Table 2.4, and the angles θ_1 and θ_2 are defined as sketched in Figure 2.9. The spin analyzing strength $\kappa_{1/2}$ depends on the type of W decay particle due to the different helicity properties in the W decay. The spin correlation strength of the used top pair event samples the dileptonic final states are extracted using the maximal analyzing strength of $\kappa_{l\pm} = \pm 1$. The angles θ_1 and θ_2 are calculated in different rest frames and are denote as θ_{l+} and θ_{l-} since leptons are chosen. The momenta of the decay particles are boosted to the rest frames of the original decaying top quarks. The angle $\theta_{l\pm}$ is defined between these boosted lepton momenta p_{l+} or p_{l-} and the according top-quark momentum boosted into the top quark pair rest frame, denoted by p_t and $p_{\bar{t}}$. The Standard Model expectation distribution is shown in Figure 2.10. By exchanging the used leptons by quarks the slope is reduced and the position of minima and maxima are exchanged, see Table 2.4 and Equation 2.4. An experimental challenge of this observable is the necessity of an event-wise fully reconstructed top quark pair system. This requires a sufficient accuracy of the used top quark pair selection and kinematic reconstruction. This observable is used to extract the spin correlation strength of the used top quark pair samples, listed in Table 4.1. Within the later data analysis a more experimental accessible variable $\Delta\phi$ [33] is considered to measure the spin correlation strength in data. The variable $\Delta\phi$ is defined as azimuthal difference between the two leptons in dileptonic top pair decays:

$$\Delta\phi = \left| \left| \phi_{l+} - \phi_{l-} - \pi \right| - \pi \right| . \quad (2.5)$$

According to this definition, $\Delta\phi$ is always positive and smaller than π . This variable is sensitive to the $t\bar{t}$ spin correlation as shown in Figure 2.11 and nearly independent of the used mass scale $\mu = m_t/2, m_t, 2m_t$, see [33, Fig. 18]. Therefore, by extraction of the $\Delta\phi$ distribution a measurement of $t\bar{t}$ spin correlation in dileptonic top pair events is feasible

Figure 2.9: Sketch of boosted momenta definition and the calculation of θ_{l+} and θ_{l-} [30].Figure 2.10: Double differential θ_{l+} and θ_{l-} distribution according to the Standard Model expectation obtained by MC@NLO 3.4.1 [31, 32].

and a full kinematic reconstruction of the decaying top quark pair event is omitted. It is a compromise between further systematic uncertainties and spin correlation sensitivity. This variable also has the benefit to have a high sensitivity and experimental accessibility to anomalous top chromo moments, see [34]. The constraints of dimensionless chromo

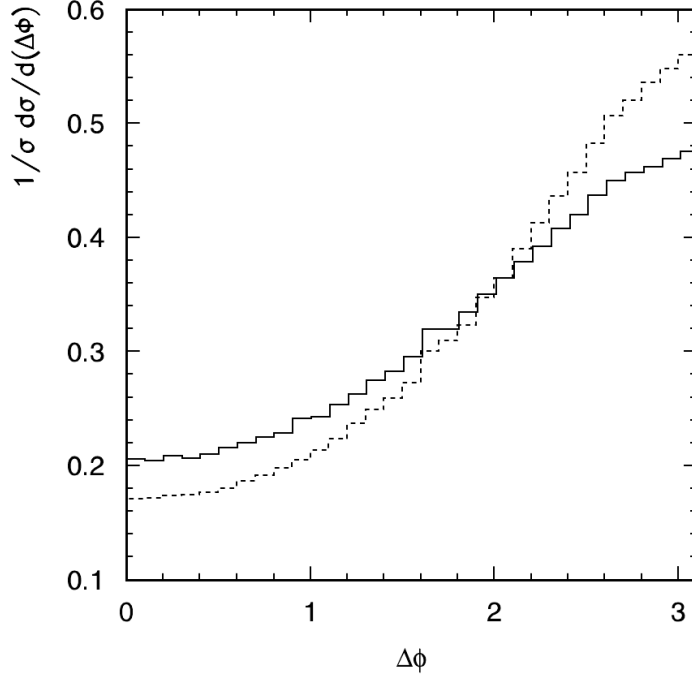


Figure 2.11: Distribution of $\Delta\phi$ assuming Standard Model $t\bar{t}$ spin correlations, solid line, and a model without spin correlation, dashed line, [33, Fig. 19].

magnetic and electric moments, $\hat{\mu}_t$ and \hat{d}_t , are complex numbers with experimental constraints of the magnitude to be smaller than $|\hat{\mu}_t| < 0.03$ and $|\hat{d}_t| < 0.1$ via the total top quark cross section. The real part of top chromo magnetic moment $\hat{\mu}_t$ is experimental accessible by the presented $\Delta\phi$ distribution, see Fig. 11 in [34].

The investigation of spin correlation in top quark pair events is also sensitive to the SUSY search for light stop quarks. In a so-called “stealth regime”, see [35], the stops have a slightly higher mass than the top quarks and a spin of zero. Therefore they are produced without spin correlation. Hence, an additional stop production washes out the angular distributions, in particular $\Delta\phi$, compared to the Standard Model expectation. Furthermore, since spin correlations are robust to systematic uncertainties related to NLO corrections they are a very promising and stable observable to search for stops. This distinguishes them from other stop searches. Additionally, possible massive particles decaying into a top pair could be well hidden by the dominating top quark pair production in proton-proton collisions. A detailed study of angular distributions presented in Equation 2.4 and 2.5 could also reveal small contributions of heavy resonances decaying into top quark pairs. Moreover, a sensitivity estimation to another possible Higgs like boson is presented in [36].

Chapter 3

The CMS Detector and the Large Hadron Collider

Within this chapter an overview of the today's world largest particle accelerator the LHC [37, 38] is presented followed by a summary of the CMS experiment [39].

3.1 The Large Hadron Collider

The LHC is the successor of the Large Electron Positron (LEP) Collider [40, 41] and is hosted in the same tunnel. Its beams provide four experiments, ATLAS [42], CMS, ALICE [43] and LHCb [44], with proton-proton, proton-lead or lead-lead collisions. There are two smaller experiments, LHC forward (LHCf) [45] and Total Elastic and Diffractive Cross Section Measurement (TOTEM) [46] respectively hosted in the ATLAS and CMS cavern. The main tunnel has a circumference of 26.7 km in a depth of roughly 100 m [37] and is located at the border of Switzerland and France, close to Geneva. The LHC is designed to provide two counter-rotating proton beams with a center of mass energy, \sqrt{s} , up to 14 TeV. During 2011 the energy was fixed to 3.5 TeV per beam, which was increased to 4 TeV during 2012. In 2015 the beam energy will be 6.5 TeV close to its design value of 7 TeV. The LHC delivered during 2011 an integrated luminosity of 6.13 fb^{-1} and the CMS experiment recorded 5.55 fb^{-1} , see Figure 3.1. Compared to the last proton-antiproton collider Tevatron [48], which delivered an integrated luminosity of approximately 12 fb^{-1} [49] at an $\sqrt{s} = 1.96 \text{ TeV}$ LHC delivered half of Tevatron's data but with a 3.5 times higher center of mass energy. Due to the energy dependence of cross sections, see Figure 2.7, the interesting process of top quark pair production has a 20 times higher cross section at LHC. Therefore, the LHC produced 850,000 top-quark-pair events in 2011 compared to 86,000 at Tevatron during 10 years.

The second operation mode of the LHC are lead-nuclei collisions with an energy of 0.18-1.58 TeV per nucleon. More details of this operation mode are given in Chapter 21 of [37].

The production of high-energetic proton beams with high luminosity is achieved by a complex pre-acceleration chain consisting of the Linear Accelerator 2 (Linac2), the Pro-

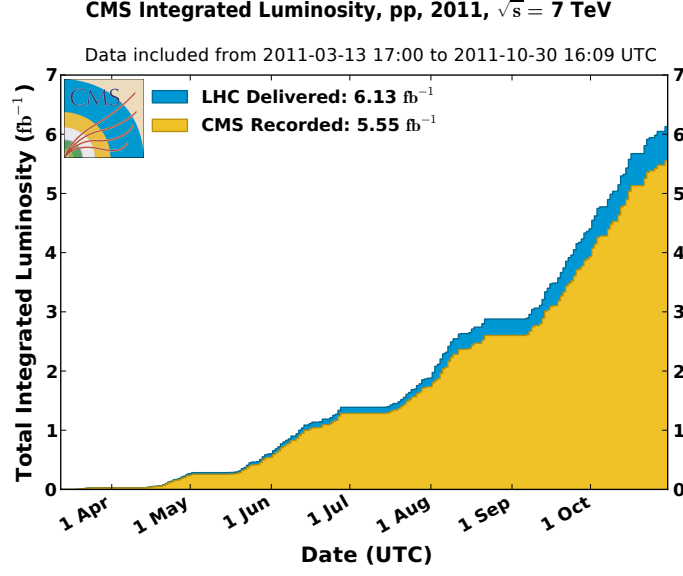


Figure 3.1: Amount of data delivered by LHC to the CMS experiment. In comparison the recorded data by the CMS experiment [47].

ton Synchrotron Booster (PSB), the Proton Synchrotron (PS) and the Super Proton Synchrotron (SPS). The produced 450 GeV protons finally enter the LHC ring and are accelerated to 3.5 GeV, see Figure 3.2. The most important LHC parameters are summarized in Table 3.1. More detailed technical information concerning LHC is available in [37, 52, 53]. During 2011, the instantaneous luminosity rose to 4.07 Hz/nb , which is half of the design value of $\mathcal{L} = 10^{34} \text{ cm}^{-2}\text{s}^{-1}$ and imposes strong time requirements on electronics, trigger and data acquisition systems of the detectors. The instantaneous luminosity \mathcal{L} can be calculated by:

$$\mathcal{L} = \frac{N_b^2 n_b f_{\text{rev}}}{A_T^{\text{eff}}}, \quad (3.1)$$

and depends on number of protons per bunch, N_b , the revolution frequency, f_{rev} , number of bunches n_b , their Lorentz factor γ_r and effective transverse beam area, A_T^{eff} , more details are given in [54]. This effective transverse beam area is defined as $A_T^{\text{eff}} = 4\pi\sigma_x\sigma_y$, where σ_x and σ_y denote the width of the approximately Gaussian transverse beam profile. Due to this high luminosity multiple inelastic proton-proton interactions occur during a single bunch crossing, see Figure 3.3, which is called pile-up (PU). These multiple proton-proton interactions challenge the detector resolution and reconstruction algorithms and are a disadvantage of the desired high luminosity. The remnants of the previous collision are called "out-of-time pile-up" and add more complexity to the simulation methods. Therefore, a precise detector and good resolution is important to distinguish between an interesting hard interaction and other parallel reactions.

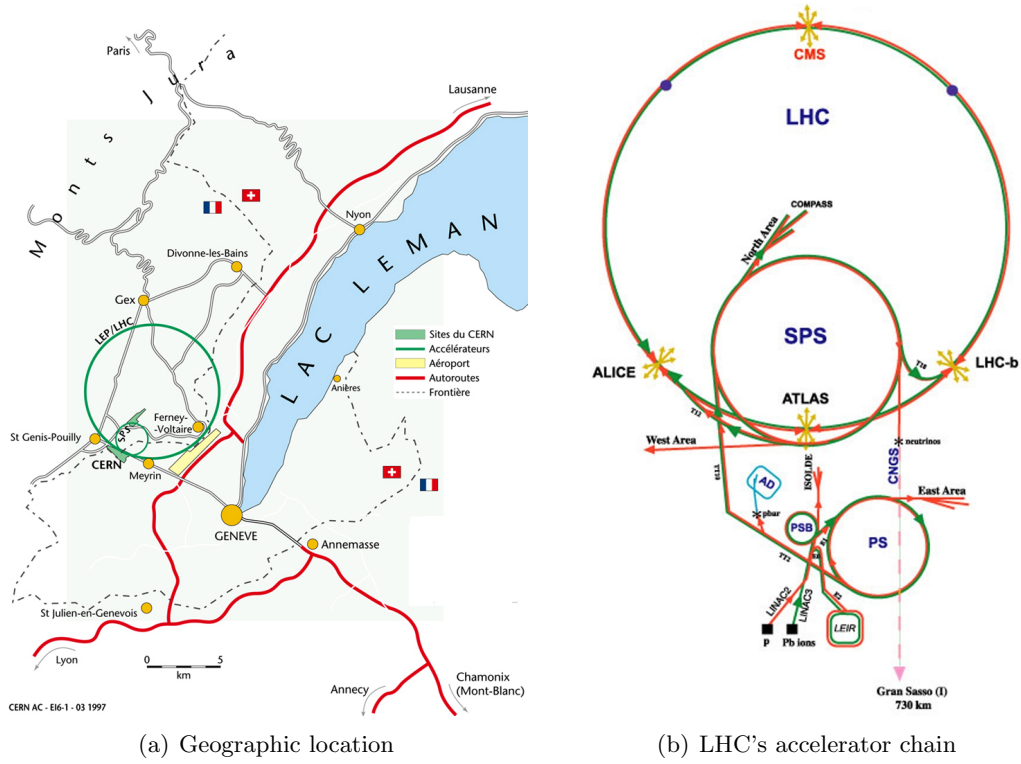


Figure 3.2: CERN and its accelerators. Left: Geographic location at the Franco-Swiss border near Geneva, based on [50]. Right: LHC's accelerator chain with all its pre-accelerators, several projects and experiments [51].

Table 3.1: Important LHC parameters for proton-proton collisions in 2011, see [37].

Parameter	value
proton energy	3500 GeV
number of collision points	4
ring circumference	26.7 km
main dipoles	1232
dipole field	8.3 T
number of bunches	2808
protons per bunch	$1.15 \cdot 10^{11}$
size at interaction point	64 μm
bunch spacing	50 ns

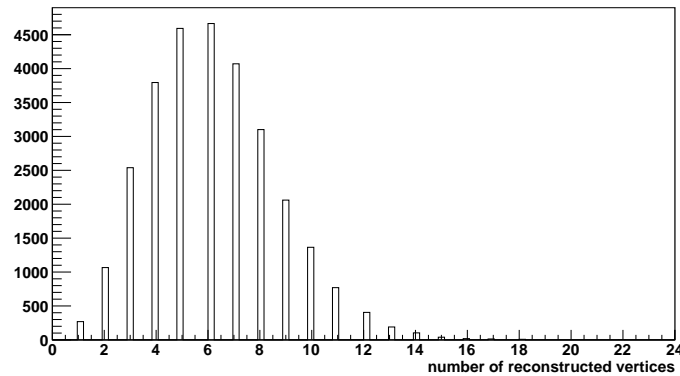


Figure 3.3: Exemplary number of reconstructed vertices per collision in data, also called “pile-up”. The events are selected by muon triggers requiring at least one single muon.

3.2 The CMS Detector

The CMS experiment is one of the four main experiments of the LHC and located at Point 5 of the LHC tunnel, close to Cessy and Gex, see Figure 3.2. CMS is an acronym for Compact Muon Solenoid [39, 55] which dimensions are a weight of 14,000 t, a length of 30 m and a height of 15 m. CMS is a multipurpose detector and consists of several layers of components which are specialized for different tasks. An overview of the whole detector is given in Figure 3.4. The CMS detector consists of different parts which are

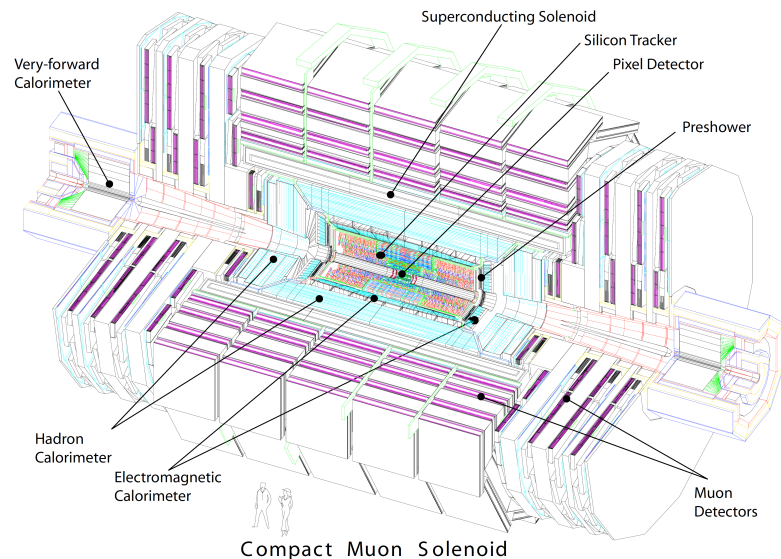


Figure 3.4: Sketch of the CMS detector [39].

arranged in shells of each other. The following subsections will describe the coordinate system and the different sub systems starting from the innermost the tracking system, following with the calorimeters, the solenoid, the muon system and closing with the trigger system.

3.2.1 The CMS Coordinate Conventions

The origin of the coordinate system used in the CMS detector is the interaction point of the detector. The z -axis is points along the beam heading to the Jura mountains, the y -axis is the vertical direction upwards and the x -axis is pointing in horizontal direction towards the center of the LHC ring. The azimuth, ϕ , is measured from the x -axis in the x - y plane. The polar angle θ is measured from the z -axis and often converted to the pseudo rapidity η given by

$$\eta = -\ln \left[\tan \left(\frac{\theta}{2} \right) \right] = \frac{1}{2} \ln \left(\frac{|\mathbf{p}| + p_L}{|\mathbf{p}| - p_L} \right) . \quad (3.2)$$

Transverse components of an object are calculated using only its x and y components.

3.2.2 The CMS Tracking System

The innermost component of CMS is its tracking system [56], which is divided in two main components: the silicon pixel detector which is as close as possible to the interaction point and is enclosed by the silicon strip detector. Its main purpose is track reconstruction of the decay products emerging out of a proton-proton collision and hence vertex reconstruction. The fine granularity, several detector layers and a high magnetic field are essential to disentangle the multiple tracks created possible several proton-proton interactions, see Figure 3.3.

The Pixel Detector System

The Silicon Pixel Detector is divided in two parts: the barrel pixel (BPIX) detector with three layers and the forward pixel (FPix) detector, which consists of two end-caps with two disks each, see Figure 3.5. The layers of the BPIX are at radii 4.4 cm, 7.3 cm and 10.2 cm and have a length of 53 cm. The pixels have a size of $100 \times 150 \mu\text{m}^2$ and a resulting occupancy of 10^{-4} per bunch crossing [39, Subsec. 1.5.5] or a rate of 1 MHz/mm^2 [55, Subsec. 3.1.1]. The FPix disks are placed at $|z| = 34.5 \text{ cm}$ and $|z| = 46.5 \text{ cm}$ with an inner radius of 6 cm and an outer radius of 15 cm. The two pixel systems have 66 million channels, an active detector surface of 1 m^2 and a resolution of $10 \mu\text{m}$ for the r - ϕ measurement and $20 \mu\text{m}$ in z direction [39].

The Silicon Strip Detector

The second silicon tracking system, the silicon strip detector, which consists of four parts: the Tracker Inner Barrel (TIB), the Tracker Outer Barrel (TOB), the Tracker

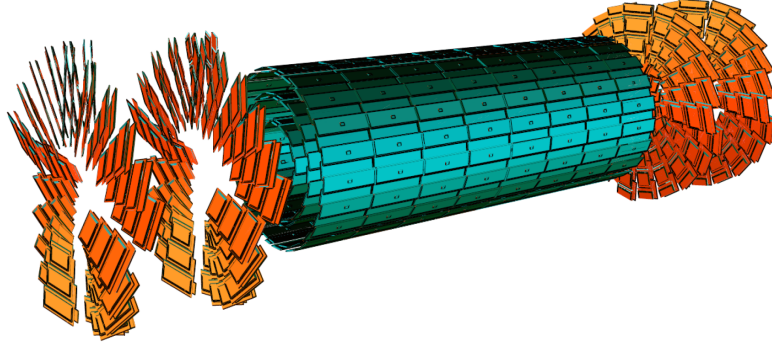


Figure 3.5: The cylindrical pixel detector system [39].

Inner Discs (TID) and the Tracker End-cap (TEC), see Figure 3.6. They combine 10 layers with a length of 1.3 m and 2.2 m and radii starting at 20 cm till 1.1 m and 12 discs with starting at $|z| = 75$ cm and ending at $|z| = 2.8$ m. The active detector area is 200 m^2 , spreads up to $|\eta| = 2.5$ in forward direction and has complete coverage in azimuth. In total more than 15,000 modules are contained with 9.6 million channels. There are more than 20 different module geometries and a part of the modules have two layers to improve the resolution achieving $23\text{--}53\text{ }\mu\text{m}$ in the $r\text{--}\phi$ plane and $230\text{--}530\text{ }\mu\text{m}$ in z direction. Both parts of the silicon tracker are operated at a temperature of -20°C to avoid damages, caused by the high radiation dose of 70 kGy at a radius of 22 cm within ten years [56]. More details and studies on radiation hardness are given in [57]. The

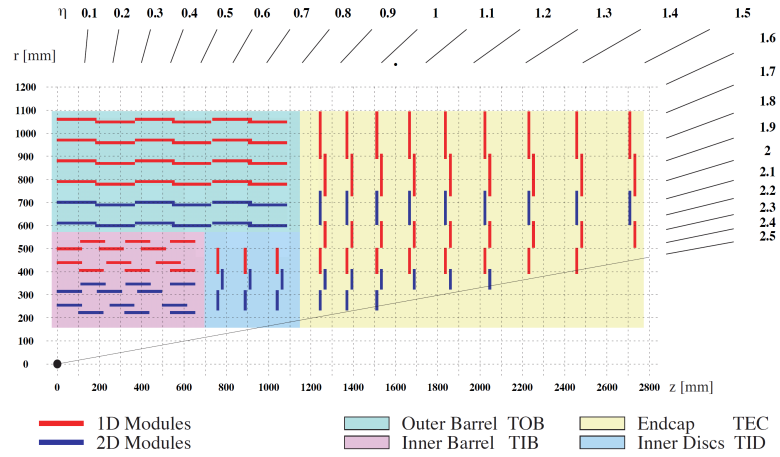


Figure 3.6: Sketch of the silicon strips detector system [39, 58].

total overall track reconstruction efficiency is depending on the particle and its energy. Hadrons with an energy $E > 100\text{ GeV}$ have an reconstruction efficiency of 95%, which is decreasing to 85% for hadrons with an energy $E = 1\text{ GeV}$. The total momentum

resolution of the tracking system is depending on the pseudo rapidity η and given as:

$$\frac{\delta p_T}{p_T} \simeq 0.005 + 0.15 \cdot p_T/\text{GeV} \quad (|\eta| < 1.6) \quad (3.3)$$

and decreases with higher pseudo rapidity. For example, at pseudo rapidity $\eta = 2.5$ the resolution is given by:

$$\frac{\delta p_T}{p_T} \simeq 0.005 + 0.6 \cdot p_T/\text{GeV} \quad (|\eta| = 2.5) \quad . \quad (3.4)$$

These high resolutions are achieved by the fine granularity of CMS tracking systems and a high magnetic field, see Section 3.2.4, providing trajectory bending for even high energy particles. The reconstruction efficiency $\epsilon_{\text{rec. PV}} > 99.75\%$ and resolution $\sigma_x < 30 \mu\text{m}$ and $\sigma_z < 50 \mu\text{m}$ of the primary vertices is excellent [59]. A track only based reconstruction of the K_S^0 mass shows an outstanding resolution: $m_{K_S^0} = 497.68 \pm 0.06 \text{ MeV}$ [60] compared with the world average of $497.61 \pm 0.02 \text{ MeV}$ [16]. The tracking and momentum resolution of muons is higher compared to electrons due to the combination of the inner tracking systems and the muon system. Further details and descriptions are given in Section 3.2.5.

3.2.3 The Calorimeters

The next detector components are the calorimeters [61, 62, 63]. These consist of an electromagnetic and hadronic calorimeter specialized to the according interaction of the particles with the detector material. These detector components are measuring the energy of the emerging particles by their energy loss or stopping them. In order to estimate the energy transferred to weakly interacting particles, e.g. neutrinos, a nearly full coverage and total energy absorption is desirable. The total energy deposition of the particles is achieved by a large material budget with a high density. The different radiation and interaction lengths of electromagnetic and hadronic interactions motivate two types of calorimeters. One dedicated to measure, i.e. stop, charged light particles and another to absorb particles which are massive and lose the majority of their energy via hadronic interaction. These two calorimeters are shown in Figure 3.7 and discussed in following paragraphs.

The Electromagnetic Calorimeter

The electromagnetic calorimeter (ECAL) is designed to measure electrons and photons with highest possible precision and has a radius of $1.29 \text{ m} < r < 1.75 \text{ m}$ and a length of 6 m . A overall sketch of its different components is given in Figure 3.8. A high energy loss of the traversing particles is achieved by scintillating lead tungsten, PbWO_4 , crystals with a density $\rho_{\text{PbWO}_4} = 8.3 \text{ g/cm}^3$. Lead tungsten has a short radiation length of $X_0 = 0.89 \text{ cm}$, a small Molière radius of $R_M = 2.19 \text{ cm}$, a short light decay time of less than 15 ns , see [61, Table 1.1], and a sufficient radiation hardness. The electromagnetic calorimeter is made of three parts: the Barrel ECAL up to $|\eta| < 1.479$, two ECAL end-caps $1.479 < |\eta| < 3.0$, and two ECAL preshowers $1.653 < |\eta| < 2.6$ in order to identify

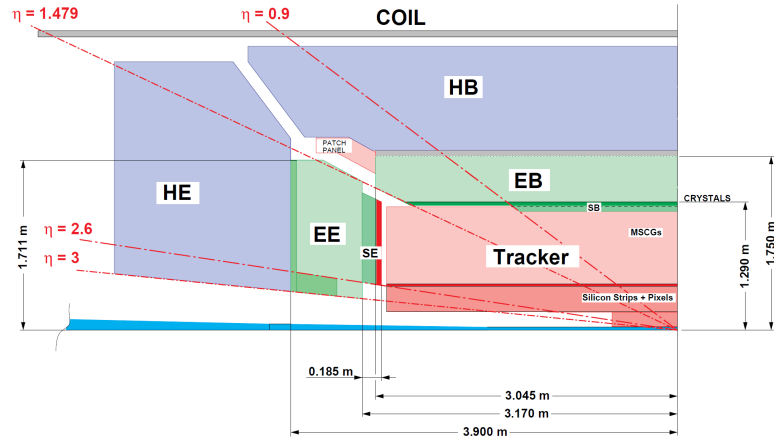


Figure 3.7: Sketch of the electromagnetic and hadronic detector system [51, 61].

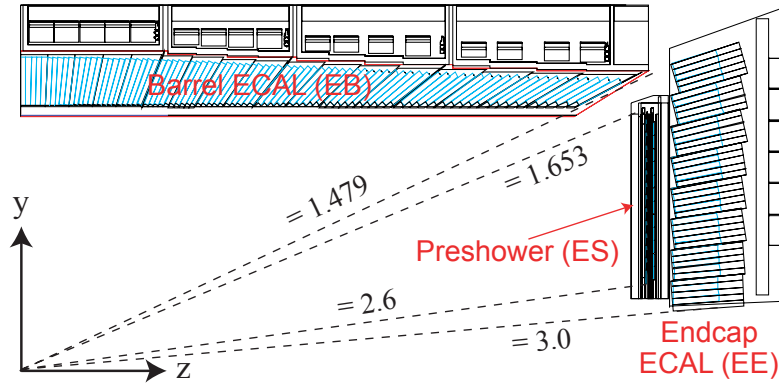


Figure 3.8: Sketch of the electromagnetic calorimeter [39, 64].

neutral pions and separate them from photons. The barrel part consists of 61,200 lead tungsten crystals with a front face of $22 \times 22 \text{ mm}^2$ corresponding to their Molière radius, a length of 23 cm, and a granularity of $\Delta\eta \times \Delta\phi = 0.0175 \times 0.0175$. The end-cap crystals have an increased front face of $28.6 \times 28.6 \text{ mm}^2$ and length of 22 cm. The preshower detectors are built of two planes of silicon strip detectors behind two X_0 and three X_0 of lead absorbers adding up to a total thickness of 20 cm. Thus 95 % of the incoming photons shower before the second plane of the preshower detector, which improves the spatial resolution at this forward region. The total radiation length at $\eta = 0$ is $25.8 X_0$ and the total energy resolution is

$$\frac{\sigma}{E} = \frac{2.8\%}{\sqrt{E}} \oplus \frac{0.12}{E} \oplus 0.30\%, \quad (3.5)$$

where E is given in GeV and obtained from electron test beams having momenta between 20 and 250 GeV [55]. Performance tests like the mass resolution for $Z \rightarrow e^+e^-$ decays show a resolution of 1.6% and 2.6 % of the barrel part and the endcaps, respectively [65].

The Hadronic Calorimeter

The hadronic calorimeter (HCAL) encloses the electromagnetic calorimeter and is the outermost component within the solenoid. With a radius of $1.81 \text{ m} < r < 2.86 \text{ m}$ and a pseudo-rapidity range of $|\eta| < 5.0$ a large coverage is achieved to increase the resolution of missing transverse energy, see Section 5.4. It is divided into four parts: the barrel hadron (HB) calorimeter, the two end-cap hadron (HE) calorimeters, the hadron outer (HO) calorimeter, and the hadron forward (HF) calorimeter, see Figure 3.7. The central part, HB, is a sampling calorimeter made of 36 wheels with 17 layers of brass read out by scintillators between them. The HB has a pseudo-rapidity range of $|\eta| < 1.4$, in total 2304 towers with a granularity of $\Delta\eta \times \Delta\phi = 0.087 \times 0.087$, and a total sampling length of 7.2 hadronic interaction length including the electromagnetic calorimeter. The transverse segmentation of the 18 HE modules is similar to the ECAL granularity and a range of up to $|\eta| = 3$ is covered.

The HE and HB are located within the solenoid, whereas the HO and HF systems are located outside. In the central part of the HO system is located at an inner radius of 3.8 m and covers an $|\eta|$ range up to 0.3. It is built of two scintillators separated by an iron plate of a thickness of 20 cm. The outer parts of the HO system extend to a range of $|\eta| < 1.26$ and are built of a single scintillator layer which has an inner radius of 4.02 m. The HO system improves the shower containment of the central part to a minimum of 11 radiation lengths and is designed as a tail catcher. Due to its position in front of the first muon stations, it is capable of detecting punch throughs, i.e. particle showers that are not stopped by the calorimeters and leaking through the solenoid into the muon system.

The HF system is located at a distance of 11.2 m from the interaction point in the very forward region of CMS. It covers the high radiation region of $3.0 < |\eta| < 5.0$ and is using a Cerenkov light based detection of quartz fibers running parallel to the beam

line. The main tasks are improving the estimation and measuring the instantaneous luminosity [55].

By combination of the electromagnetic and hadronic calorimeters an energy resolution of

$$\frac{\Delta E}{E} = \frac{0.7}{\sqrt{E/\text{GeV}}} \oplus \frac{1}{E/\text{GeV}} \oplus 8\% \quad (3.6)$$

was measured using test beams of pions [66]. During the CRAFT [67] run in 2008 a muon energy loss of 2.85 GeV with a statistical error of 0.02 GeV in the HB system was measured for a muon momentum of 135-170 GeV [68]. This result is in good agreement with the test beam results and simulation [68].

3.2.4 The Solenoid

The high magnetic field of $B = 3.8\text{ T}$ is provided by a superconducting solenoid cooled by liquid helium. The solenoid encloses the calorimeters and has an inner bore of 5.9 m, an outer radius of 6.3 m and a length of 12.9 m. The magnetic field is generated by a current of 19.1 kA and stores an energy of 2.6 GJ [55]. The return yoke is built of three iron layers used as support structure and housing of the muon system, the most outer detector component, described in the next Subsection 3.2.5. The magnetic field penetrates the complete CMS detector and bends the trajectories of charged particles. The different trajectory curvatures permit the determination of particle momenta up to $\mathcal{O}(\text{TeV})$. This high magnetic field causes also some displacement of the CMS subdetectors, called misalignment, which is corrected by hardware alignment systems and taking into account during the particle trajectory reconstruction.

3.2.5 The Muon System

The muon system is one of CMS key features and name giving components. This outermost detector system is integrated into the return yoke and benefits from the inherent magnetic field. The main usage is the identification and momentum measurement over a wide kinematic range and providing fast trigger information. Three types of gaseous detectors are used within the muon system, see Figure 3.9. Drift tube (DT) chambers cover an area up to $|\eta| < 1.2$ with a low magnetic field and muon rate. The DTs are located in four layers at radii from 4.0 till 7.0 m from the beam line. They are mostly built of three super layers of four staggered drift tube layers and capable of measuring the $r - \phi$ and z coordinate of a crossing muon. In total 250 DTs are used in the barrel part providing a spatial resolution per chamber of $80 - 120\text{ }\mu\text{m}$ [69] or a single hit resolution of $260\text{ }\mu\text{m}$ [70]. The reconstruction efficiency for hits and track segments originating from muons traversing the muon chambers is in the range $95 - 98\%$ [69] and the reconstruction efficiency of high-quality local track segments in each station is about 99% [70] in all stations. The two end-caps are covering the pseudo rapidity region of up to $0.9 < |\eta| < 2.4$ which has a higher muon rate and magnetic field. Therefore, they are equipped with 468 Cathode strip chambers (CSC) providing a fast response time, fine

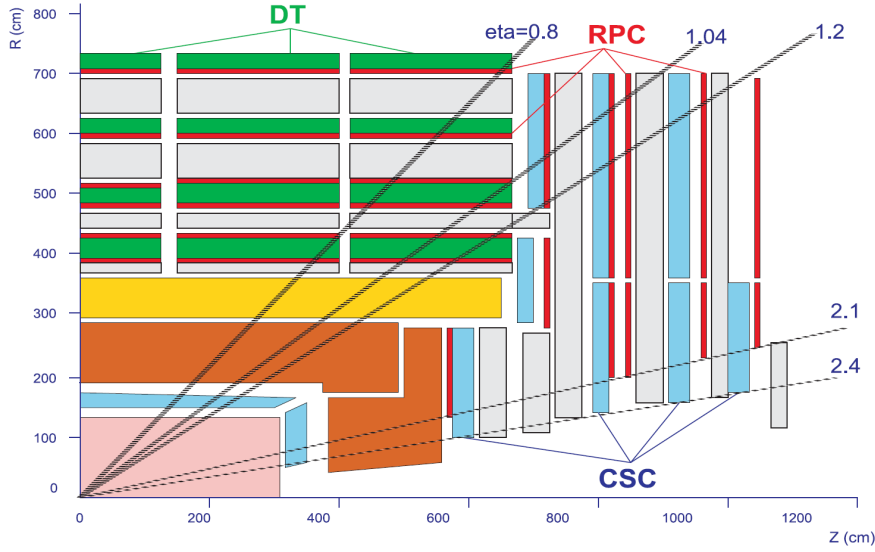


Figure 3.9: Sketch of the CMS muon system [39, 51].

segmentation and sufficient radiation hardness. These are mounted into four disks perpendicular to the beam axis. The spatial resolution is typically between $40 - 150 \mu\text{m}$ [69]. Trigger information is obtained by all parts of the muon system. Especially the resistive plate chambers (RPC) extending to $|\eta| < 2.1$ with a spatial resolution of $0.8 - 1.2 \text{ cm}$ [69] have a very fast response time of less than 3 ns . They offer additional independent and segmented information and can unambiguously identify the correct bunch crossing.

3.2.6 The Trigger System

The trigger system of CMS consists of two levels, the Level 1 (L1) trigger and the High Level Trigger (HLT). The purpose of these systems is to reduce the enormous data produced by the read-out channels of all subdetectors. Considering the LHC event rate of 40 MHz and the average event size of 1 MB , the trigger system needs to process a data rate of roughly 40 TB/s . The L1 system is based on programmable custom-made electronics and uses coarsely segmented data from the calorimeters and the muon system. It reconstructs first object candidates for muons, electrons, jets, and photons, called L1-objects and processes a set of selections called L1 paths. An event passes this L1 trigger if one of these paths are successfully processed. The total event rate is reduced to roughly 20 kHz and passed to the HLT system. The maximum latency between a bunch crossing and the final L1 decision is $3.2 \mu\text{s}$, within the high resolution data is held in pipe-lined memories of the front-end electronics [71, 72]. The HLT system analyzes the complete data, is software based and runs more complex algorithms. These algorithms are similar to later offline analysis to reconstruct the object candidates more precisely. The HLT consists of roughly $13,000$ commercial CPUs and reduces the L1 rate to 1 kHz , which is written to storage. The average processing time in 2012 was 200 ms per event. The

complete trigger system was commissioned during CRAFT [73, 74].

3.2.7 Luminosity Measurement

A very important input variable for a lot of physics analyses is the integrated luminosity of an experiment. The CMS experiment measures the instantaneous luminosity by the HF calorimeter and estimates it by pixel system during the offline data analysis. During a run period the beam settings change, e.g. the bunch number and number of protons per bunch, therefore the instantaneous luminosity and corresponding event rates rise. The increasing event rates induced higher trigger thresholds in order to keep the total event rate written to disk constant. The alternating triggers used for this analysis are discussed in Section 6.3.1. The integrated luminosity of each luminosity section varies from 0.01 nb^{-1} to 92 pb^{-1} and is estimated by the HF system [75, 39] during runtime. The data is segmented in luminosity sections corresponding to roughly 23 s of data taking. Trigger thresholds are adjustable at the base of these luminosity sections. A more precise luminosity estimation is obtained by counting vertices with the pixel detector [76]. It is used as an independent measurement of the “online” luminosity estimation. Both methods are in reasonable agreement. Therefore, this analysis relies on the pixel based luminosity calculation, which is recommended by the CMS collaboration.

Chapter 4

Collision Data and Event Simulation

In this chapter a brief summary of the established CMS event simulation procedures, a more detailed description of the used collision data and the analysis-specific event-simulation of top quarks is given.

4.1 Collision Data

The data recorded data by CMS in 2011, $\mathcal{L}_{\text{CMS int.}} = 5.55 \text{ fb}^{-1}$, is checked for detector failures and miscalibrations and a full operational detector. The estimation of the recorded integrated luminosity is described in Section 3.2.7. The Physics Validation Team (PVT) provides a list of good and validated luminosity sections in the JavaScript Object Notation (JSON) format. This file is the so-called “golden JSON file” of a run period. The used JSON file and primary datasets are listed in Table A.1 and Table A.2. The total collected data in 2011 intersected with the according JSON files provides an total integrated luminosity $\mathcal{L}_{\text{int.}} = 5.0 \text{ fb}^{-1}$ which is used for this analysis.

4.2 Event Simulation

The official event simulation procedure established within the CMS collaboration is divided in several steps. In general the detector response to a physical process is simulated by several Monte Carlo (MC) generators [77], within different steps. The following subsection summarize the main parts starting with the matrix element simulation followed by the hadronization and fragmentation of the final state particles and closing with the CMS detector response and pile-up simulation.

4.2.1 Matrix Element Generators

Matrix element (ME) generators simulate the initial proton-proton collision and the resulting particles according to the desired interaction processes and Feynman graphs.

The level of detail is given by the used matrix element generator. This analysis uses MC@NLO 3.4.1 [31, 32] and POWHEG BOX 1.4 [78, 79, 80, 81] which are next-to-leading order (NLO) generators. The official samples used for background description are generated also using PYTHIA 6.4.24 [82] and MadGraph 4 [83, 84]. More details are given in Section 4.3.1. The simulated events are produced in the standardized Les Houches Event (LHE) format [85] and passed to a hadronizer. Hadronizers are event generators, which simulate the hadronization and fragmentation of the final states of a given interaction. During these steps τ lepton decays are modeled by TAUOLA 2.7.121.5 [86, 87]. Additionally initial state radiation (ISR) and final state radiation (FSR) is added to the events. By using NLO generators an mandatory matching between the Hadronizer and ME generator is needed due to double counting of radiations. According to official CMS naming conventions, these steps are summarized in single step called generation (GEN). The output of the hadronizer are colorless and nearly stable particles, which reach the CMS detector. Weakly decaying particles like muons, pion and kaons are exceptions. Due to the high collision energy these particles with a usual lifetime of $\tau \simeq 10^{-8}$ s are relativistic and have a mean decay length in the order of the first detector layers and sometimes the distance calorimeters. The decay and interaction with the detector materials are simulated by the GEANT4 simulation toolkit [88, 89].

4.2.2 Detector Simulation

The detector simulations mimics the response of all sensitive components to an simulated event. The well established simulation toolkit GEANT4 is used to simulate the interaction between emerging particles and their decay particles with the detector materials and components. The obtained energy hits and depositions of the different detector components. This output is processed by the frontend electronics simulation and digitalization simulation. This step is called correspondingly DIGI. Finally the obtained detector response is reconstructed by the official RECO and has the same technical format as recorded data, see Chapter 5.

4.2.3 Pile-up Simulation

Multiple proton-proton interactions per bunch crossing dilute the detector response of a desired hard interaction by additional energy depositions and tracks. Therefore, a random number of events taken from a simulated MinBias dataset, and their detector response is added to the hard interaction. Afterwards the reconstruction is applied to the resulting combined detector response. There are different pile-up scenarios simulated according to the average number of collision vertices. This analysis assumes the pile-up scenario number six with an average number of collision vertices like Figure 4.1. Since the recorded number of vertices per event, is not perfectly mimicked by the assumed pile-up scenario, this analysis applies an event-wise reweighting to take this effect into account.

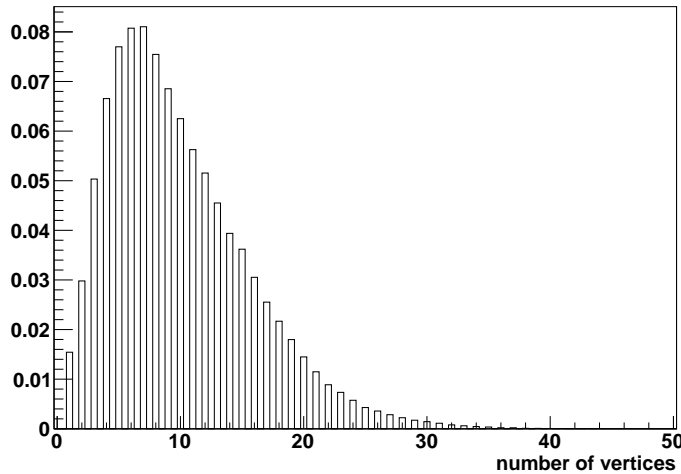


Figure 4.1: Number of vertices assumed in pile-up scenario number 6.

4.3 Top Quark Event Simulation

This section describes the simulation of the non Standard Model scenarios generated for systematics related to top quark uncertainties. These non Standard Model samples are needed for the template fit to estimate uncertainties related to top-quark modeling.

4.3.1 Matrix Element Generators

The non-Standard Model sample of top quark pair events with no spin correlation, i.e. $A = 0$, was privately generated and officially approved by the CMS collaboration. Since a template fit is used to extract the spin correlation strength each top quark related systematic uncertainty also has to be simulated with this non Standard Model scenario. The preferred ME generator is MC@NLO 3.4.1. which is approved by the CMS collaboration and used for official samples. In order to estimate the uncertainty related to the used ME generator an additional sample collection using POWHEG BOX 1.4 is created. The intrinsic spin correlation strength using Standard Model input values is similar for both generators and the obtained values are given in Table 4.1. The spin correlations strength is estimated by using the double differential distribution, see Equation 2.4, and selecting dileptonic decays. The obtained spin correlation strength is in reasonable agreement with the Standard Model expectation of $A_{\text{SM}} = 0.31 \pm 0.01$. Both, ME generators and the theory calculations apply approximations during their calculations. Therefore, a deviation of 6.5% of the presented results is feasible.

Table 4.1: Spin correlation strength of the used top quark pair samples. The shown correlation strength is obtained by fitting the distribution of equation 2.4 obtained from top quark pair events generated with MC@NLO 3.4.1 and POWHEG BOX 1.4. Uncertainties are neglected due to their limitation by the generated statistics.

sample	A
MC@NLO	0.33
POWHEG BOX	0.29

Table 4.2: Systematic samples related to top quark uncertainties. Systematic samples dedicated to the renormalization and factorization scales are generated with $\mu_{\text{ren.}} = \mu_{\text{fac.}}$.

systematic	variables
top mass	$m_t = 169.5, 172.5, 175.5 \text{ GeV}$
ren./fac. scale	$\mu_{\text{ren./fac.}} = \frac{1}{2}m_t, m_t, 2m_t$

4.3.2 Non Standard Model Spin Correlation Production

The non Standard Model scenarios are produced by disabling the decay of the top quarks within the initial ME generator. Since the output of the ME generator is transferred via the LHE format to the hadronizer PYTHIA 6.4 or HERWIG 6.5.20 [90], all spin information is lost. Therefore, the spin of the two top quarks is not correlated after execution of the hadronizer. This procedure is applied for all samples generated by MC@NLO 3.4.1 and POWHEG BOX 1.4 and describes the systematic top quark uncertainties.

4.3.3 Systematic Top Samples

Several systematics related to top quarks also have to be simulated using the no spin correlation scenario. The systematic uncertainties are divided in two groups. One group is modeling different top quark masses of $m_t = 169.5, 172.5, 175.5 \text{ GeV}$ and the second group is related to uncertainties of modeling top quark production. The top quark production modeling is dependent on the chosen renormalization and factorization scale. The renormalization scale is set to $\mu_{\text{ren.}} = 1/2 m_t, m_t, 2 m_t$ by which the interaction strength of the strong coupling in the matrix element calculation is varied. By convention the factorization scale using $\mu_{\text{fac.}} = 1/2 m_t, m_t, 2 m_t$ is set to the same values and defines which processes are calculated by the ME generator and which are left out for the hadronizer. The different samples related to top quark uncertainties are listed in Table 4.2. In total each systematic sample contains 10 million events, which is roughly half of the size of official top quark pair samples. Due to the large number of additional samples the production is using FastSim [91], which is a reasonable approximation of the detailed detector simulation. The following section presents the sample validation.

4.3.4 Validation of private samples

The obtained samples are compared to the official production of top quark pair events using the same Matrix Element generator and hadronizer. The complete detector simulation and event reconstruction is repeated. In order to validate the private production the number of reconstructed muons, electrons and jets and their kinematic distributions of p_T , η , ϕ and are investigated. These distributions show a reasonable agreement in particle kinematics and numbers. A similar result is obtained by a second comparison with events passing the analysis. Additionally, more sophisticated variables like MET and the CSV jet discriminator are examined. These variables are very sensitive to differences in the event kinematics because they have a large variety of input variables and are nearly depending of the whole event kinematics. In both distributions no significant deviations are observed.

Chapter 5

Event Reconstruction

This chapter outlines the event reconstruction techniques and methods applied on recorded data and simulated events. This step is called RECO and consists of a set of algorithms building particle candidates. The standard reconstructions for jets, muons, electrons, and missing transverse energy are outlined and their performance is presented.

In general, the reconstruction is based on the signal of different subdetectors of CMS. Each specialized subdetector provides information to identify a group of particles by their specific signature. The full reconstruction of recorded data events, also called “of-line reco”, applies more complex and sophisticated algorithms. It also combines several detector components in contrast to the simplified reconstruction performed by the HLT and L1 trigger system. Figure 5.1 shows different particle types and their footprint in several components of the CMS detector. The following sections describe the details for muons, electrons, jets, and missing transverse energy, respectively. Finally, high level algorithms like b -tagging and particle flow event-reconstruction are summarized.

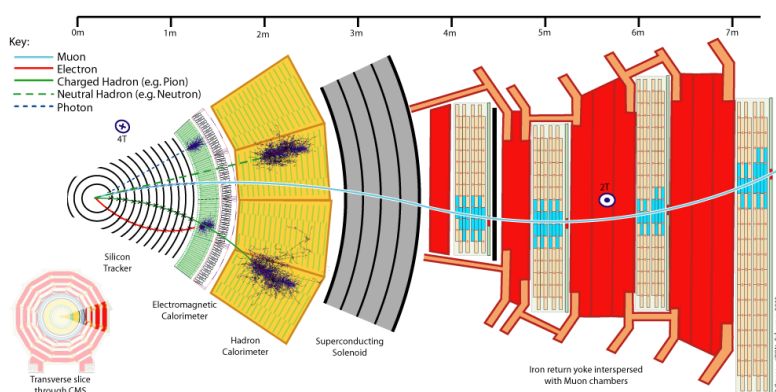


Figure 5.1: Slice of the CMS detector with exemplary particle tracks.

5.1 Muons

Generally, muons generated by top quark decays travel through the entire detector, because their energy loss is nearly minimal from a few GeV up to one TeV, see [16, Fig. 27.1]. The minimal energy of a muon reaching the muon system is 3–4 GeV [92]. Muons with less energy are not reaching the muon system due to energy loss by ionization or are curled up by the magnetic field. Therefore, high energy muons create matching tracks within the inner and outer tracking system. The standard muon reconstruction procedure defines two categories of muon reconstruction approaches: the “Global Muon Reconstruction” and the “Tracker Muon Reconstruction”. The Global Muon Reconstruction begins with the muon system and searches for track candidates with a sufficient number of hits and track quality, like χ^2/NDF , see [92]. These muon tracks are called “stand-alone” muons [93] and have a good resolution for muons with a momentum $p_T < 200$ GeV [92]. Their tracks are built by applying the Kalman-filter technique [94] on the set of recorded hits in the outer tracking system and a beam spot constraint starting from L1 trigger muons, see [72]. The tracks are fitted from both directions, inner most muon system layer to the outer most and vice versa. Afterwards, the standalone tracks are interpolated to the inner tracking systems and a matching track within the inner tracking system is found by comparing the two tracks on a common surface. A “global track” is fitted by combining the hits of both tracks and using the Kalman-filter technique. The finally resulting muon is called “Global Muon”. A similar procedure is used in the second approach. Its results are “Tracker Muons” which are built from tracks in the inner tracking system, interpolated to the muon system and looking for a matching track muon system track. Radiation and energy loss in the surrounding material, multiple scattering and non-uniform magnetic field are considered by using GEANT4 for the iterative track propagation [39, Sec. 9.9.1]. These inner tracks have to pass several criteria in combination with the stand-alone track. Combining these two approaches and applying additional track criteria the “Tight Muon ID” is defined [92]. The global track is required to have at least a reasonable quality $\chi^2/\text{ndf} < 10$, at least one assigned muon chamber hit, the tracker track has at least ten assigned hits in the tracking system and the corresponding impact parameter has to be $|d_{xy}| < 2$ mm with respect to the primary vertex. These so-called “Tight Muons” are used as starting point of the particle flow reconstruction, see Section 5.5. The transverse momentum resolution varies from 1 % to 6 % depending on pseudorapidity for muons with p_T below 100 GeV [92].

5.2 Electrons

Electrons are stopped in the electromagnetic calorimeter creating a footprint and leave a track in the inner tracking system. Due to their small mass a lot of Bremsstrahlung is emitted by traveling through matter, which dilutes their track and broadens the energy deposition. Due to the bending of the magnetic field, electrons have a characteristic footprint in the calorimeter with a narrow width in η and a spread in ϕ direction. In order to correct for these effects a Gaussian Sum Filter (GSF) is applied to fit the

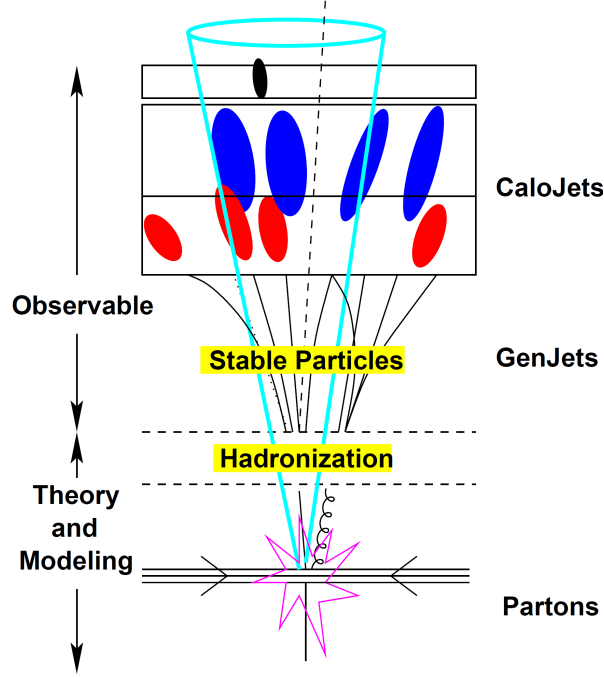


Figure 5.2: The concept of jets. A particle created by hard scattering evolves into a group of color neutral particles which are detected [51].

according track, [95]. The GSF assumes a sum of Gaussian functions and instead of one single Gaussian function like the Kalman filter [94]. More technical details are given in [96, 97]. In total, electrons, selected by a tag-and-probe method based on $Z \rightarrow e^+e^-$ events, showed a reconstruction efficiency of over 96.8 % [96].

5.3 Jets

Jets classify a group of tracks pointing in the same direction and their corresponding energy deposits in the calorimeters. The concept of jets is inspired by the fragmentation and hadronization of partons generated by a hard scattering. These partons are not detectable since they are not color neutral and transform instantaneously into a color neutral state, see Figure 5.2. Therefore, jets are estimators for energy and momentum of the initial parton from hard scattering which is diluted by color reconnection, hadronization and fragmentation. They are built by jet algorithms which search for tracks or calorimeter entries pointing in similar direction and cluster them. There are various jet algorithms available using sequential recombination or cones to cluster their entities. The CMS collaboration is using the particle flow algorithm (PFLOW) [98, 99] for the event reconstruction. Jets are built by using the particle flow output as constituents of a jet and applying the anti- k_T algorithm, see Section 5.3.1. This widely used

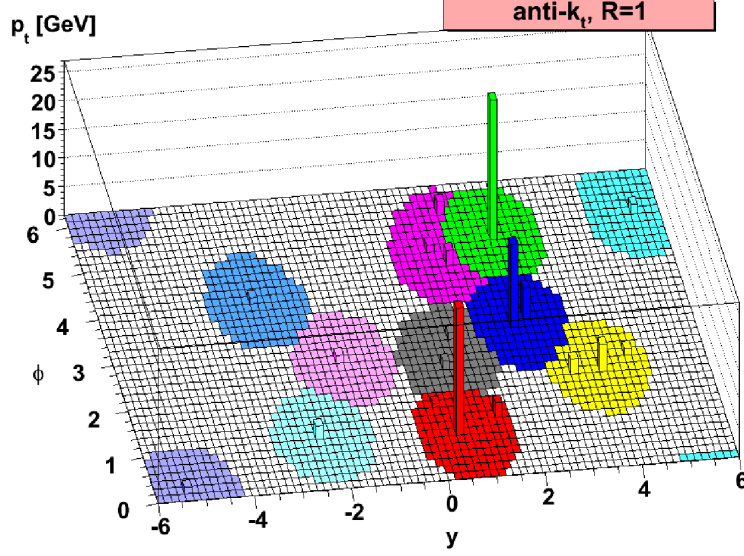


Figure 5.3: A sample parton level event analyzed by the anti- k_T algorithm [100] with additional low energy entries.

jet algorithm is described in the following subsection.

5.3.1 The Anti- k_T Algorithm

The anti- k_T algorithm is a sequential cone jet algorithm, which is collinear and infrared safe. It is based on recombination and the distance of its entities. It is parametrized by the power of the energy scale and is adjusted by the cone size R . The resulting cones are almost symmetric, see Figure 5.3, and common sizes are $R = 0.4$ and $R = 0.6$. The distance measure is defined as

$$d_{ij} = \min\left(\frac{1}{k_i^2}, \frac{1}{k_j^2}\right) \frac{\Delta_{ij}}{R^2}, \quad (5.1)$$

$$d_{iB} = \frac{1}{p_i^2}, \quad (5.2)$$

where $\Delta_{ij} = (y_i - y_j)^2 + (\phi_i - \phi_j)^2$ and k_i , y_i and ϕ_i are respectively the transverse momentum, rapidity, and azimuth of particle i . More details are given in [100]. The later discussed Particle Flow algorithm is applying the anti- k_T algorithm for jet calculation and assignment.

5.3.2 Jet Energy Corrections

The measured jet energy is diluted by inefficiencies and additional processes like electroweak interactions. Therefore, an energy correction of the reconstructed jets is mandatory. These energy corrections are factorized in different categories, see Figure 5.4, and

the mandatory corrections depend on the measured jet energy, η , and p_T . The CMS col-

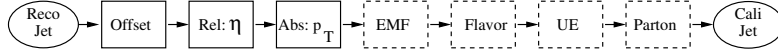


Figure 5.4: Official jet correction procedure. The first three levels are recommended by the CMS collaboration [101].

laboration also provides corrections for the electromagnetic fraction, flavor, and so-called parton level of a jet, which are not used in this analysis. Details concerning these additional and not mandatory corrections are presented in [101]. The standard procedures and correction steps are summarized in the following section. Additional details and technical descriptions are given in [102]. The standard set of applied energy corrections are the levels L1, L2 and L3 for data and simulated events.

The offset correction, “L1 Pile Up”, is the first step which estimates and subtracts the energy not associated with the high- p_T scattering. These are the contributions by electronic noise and pile-up events.

The next correction level, “L2 Relative”, flattens the jet response in η . The correction factors are obtained from Monte Carlo events, by assigning a Monte Carlo truth particle matching in the η - ϕ plane. The obtained calibration factors reduce the bulk of inequality in η .

The last recommended correction level is an absolute correction in p_T , called “L3 Absolute”. This correction flattens the p_T response and its correction factors are obtained using data driven techniques, i.e. the Z/γ +jet balance technique [102, sec. 5].

For data an additional correction called “L23 Residuals” is applied in order to correct small discrepancies due to insufficient detector simulation, see the description of the L2 correction. These correction factors are also derived from data using the dijet method. The method uses dijet events and restricts one jet to point to the central region of the detector $|\eta| < 1.3$ and calculates a balance parameter for the second jet with an arbitrary η value. The estimated residual corrections are of the order of a few percent [102, Fig. 11]. The jet response is not flat, because of the inhomogeneous material budget in η and therefore corresponding inefficiencies in η . Furthermore, it is also highly depending on the applied jet algorithm, see [102, Fig. 6/7]. Finally, all corrections are sequentially applied and the resulting energy and p_T values are used for selection and kinematic event reconstruction.

5.3.3 b -Tagging

Jets generated by b quarks, which fragment to B mesons and baryons, are distinguishable from jets created by light flavors, i.e. u , d , s , and c quarks. B mesons decay predominantly to D mesons and additional particles. These weak decays have a lifetime of 10^{-12} s and lead to a secondary decay vertex for high energy B mesons. This analysis uses the “Combined Secondary Vertex” algorithm, which is based on the secondary-vertex significance. The combination of the significance and the properties of the resulting jet, e.g. number of tracks and interaction parameter [103, 104, 105] provides a well discriminating

observable.

5.4 Missing transverse energy

Missing transverse energy (MET), denoted by \cancel{E}_T , is a variable referring to the transverse energy of non-interacting particles and energy loss by dead material. It is calculated with the assumption that the event is balanced in p_T :

$$\cancel{E}_T = - \sum_i p_T^i \quad . \quad (5.3)$$

Due to non-vanishing transverse momentum contributions by PDFs every event has a small p_T imbalance. Therefore, the sum of the emerging neutrinos in an event is still strongly correlated with the observed MET, but they are not equal. Additional inefficiencies and mismeasurements dilute this correlation. During the run in 2010 the performance of the MET was measured and showed a good agreement for $Z \rightarrow l^+l^-$ and photon events [106] between data and Monte Carlo.

5.5 Particle Flow

The preceding sections focused on a single candidate reconstruction. The modular structure of the software framework simplifies the use of a large variety of reconstruction hypotheses. The recommended event reconstruction procedure relies on the particle flow algorithm. This algorithm uses the advantage of combining all detector components [98, 99, 107, 108] and aims at reconstruction of all stable particles contained in an event. It starts with building calorimeter clusters and reconstructing tracks in the inner tracking system. These tracks are associated with calorimeter clusters by extrapolation of the track to the calorimeters. Subsequently, muons in the outer tracking system are reconstructed and a pre-electron identification is executed using the GSF algorithm. The remaining and not assigned clusters are reconstructed as photons for ECAL clusters and neutral hadrons for HCAL clusters. The obtained set of muons, electrons, photons and hadrons is used to build jets, and MET. Furthermore, τ leptons are identified and the isolation of all reconstructed particles is calculated. Jets are constructed by the anti- k_t -algorithm, see Subsection 5.3.1.

The particle flow algorithm has a similar muon reconstruction efficiency and a lower fake rate [108] compared to standard muon reconstruction. An measurement of the J/Ψ mass $m_{J/\Psi}$ using particle flow electrons showed a result of $m_{J/\Psi} = 3.07 \pm 0.01$ GeV, which is very close to the world average of 3.10 GeV. Additionally, the association efficiency of 97 % [108] between particle flow electrons and GSF electrons is very good. The reconstructed jets reconstructed by the Particle Flow algorithm have a significant better energy response, see [98, Fig. 6], than jets reconstructed using only calorimeter information. The same results are obtained comparing the particle flow MET with the calorimeter based MET calculation [98, Fig. 18].

Chapter 6

Selection

This chapter describes the applied selection and its influence on the $t\bar{t}$ spin correlations. At the beginning the main background processes of this analysis are briefly described and the applied object selection is outlined. The event selection follows and its influence on $t\bar{t}$ spin correlations is investigated. The event and object selection are inspired by the expected signature of dileptonic top pair events containing only electrons and muons and jets, see Figure 2.8. The entire selection consists of three subselections according to the three dileptonic signal channels. All channels share the same object selection but differ in their event selection. Finally, the selection is validated by comparing several distributions obtained from data with their Monte Carlo expectation. At the end of this chapter, different correction procedures related to pile-up simulation, trigger efficiency and b -tag modeling are described.

6.1 Background Processes

In general, background processes are hard proton-proton interactions, which are different from $t\bar{t}$ production and decay processes. Within this analysis all processes except the top-quark-pair events decaying dileptonically are considered as background processes. This section presents an overview of the most important background processes of the analysis. These can be divided in two groups: Firstly, processes, which have a signal like signature, and secondly, processes with a high production cross section compared to top quark pair events. Dataset name, used ME generator, cross section, the total number of events and the corresponding integrated luminosity are given in Table A.3.

6.1.1 QCD Processes

A very important background process due to its high cross section are QCD events. The cross section is of the order of $\sigma_{\text{QCD}} = O(\text{mb})$ and is very high compared to top quark pair production. An exemplary Feynman graph is given in Figure 6.1. With additional radiation of gluons or jet splitting a sufficient number of reconstructed jets is generated and the obtained signature is very similar to a top quark pair event. Due to the high

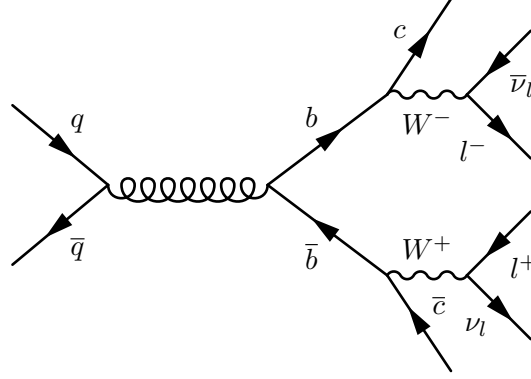


Figure 6.1: A $b\bar{b}$ event decaying dileptonically.

cross section an inclusive simulation of QCD events is technical not affordable, therefore some minimal kinematic and particle requirements are implied. Events of the QCD sample used for this analysis have to contain a particle carrying a minimal transverse momentum of 20 GeV and a muon with at least $p_T > 15$ GeV, see Table A.3. This background is strongly reduced by requiring high energetic and isolated leptons.

6.1.2 W Boson Processes

These background processes are modeled using an official sample containing W bosons, which decay leptonically, i.e. into e or μ , see Table A.3. This background process also dominates by its high cross section in the order of $\sigma_{W+\text{jets}} = O(10\text{nb})$, see Figure 2.3. The initial high energetic and isolated lepton mimicks a dileptonic top quark pair signature with additional jets and a second lepton, see Figure 6.2. This background process is reduced by requiring several high energetic jets and a second isolated lepton.

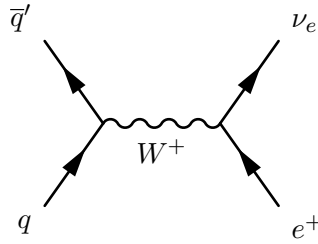


Figure 6.2: An example of a W boson production.

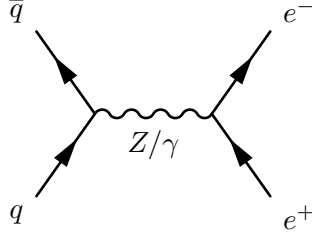


Figure 6.3: Exemplary Drell-Yan production.

6.1.3 Drell-Yan Processes

Drell-Yan (DY) processes create a virtual photon or Z boson which then decays into a pair of oppositely-charged leptons. Due to a production cross section of $\sigma_{\text{DY}} = O(10\text{nb})$ a minimal lepton pair mass is required in order to minimize the technical effort. The official used samples and their technical details are listed in Table A.3 and an exemplary Feynman graph is shown in Figure 6.3. In general, requiring additional jets reduces this background significantly, except in the phase space of resonant Z boson production. Events with a lepton pair mass in the range of $m_{\ell\ell} \in (76, 106) \text{ GeV}$ are discarded because of the dominating Z boson production.

6.1.4 Diboson Processes

Diboson production are processes containing two of the weak exchange bosons W^\pm or Z . These processes are modeled using three official samples listed in Table A.3. A general Feynman graph of the production is shown in Figure 6.4. The production cross sections are : $\sigma_{WZ} = 18.2 \text{ pb}$, $\sigma_{WW} = 47 \text{ pb}$, and $\sigma_{ZZ} = 7.67 \text{ pb}$. These processes are likely to contain two high energetic isolated leptons. Therefore only jets are missing at leading order (LO) Feynman graphs if leptonic W boson decays are assumed.

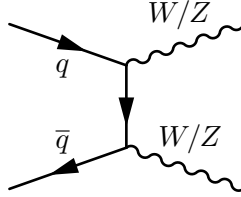


Figure 6.4: Exemplary diboson production.

6.1.5 Single Top Processes

The single top-quark production and decay is very similar to top-quark pair events. They contain one top quark and at least one high energetic quark or W boson, see

Figure 6.5. There are three production channels for single top quark events. The s-

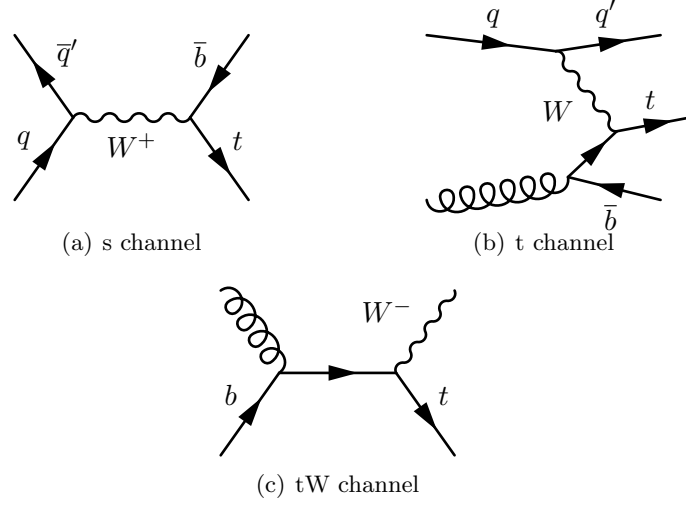


Figure 6.5: The three production channels of single top events.

channel production has the lowest total cross section of $\sigma_{t,\text{s-ch.}} = 4.1 \text{ pb}$. Due to the parton density functions of the proton, the production of a top quark is roughly twice as likely than antitop quark production, see Table A.3. The tW -channel production has a production cross section of $\sigma_{t,tW\text{-ch.}} = 15.7 \text{ pb}$ and has an equal production probability of top and antitop quarks. The dominant production mode of single top quark events is the t -channel with a cross section of $\sigma_{t,t\text{-ch.}} = 63 \text{ pb}$. Due to the initial u quark in the t -channel top quark production Feynman graph the cross sections producing a top and antitop quark differ by roughly a factor of two, see Table A.3.

6.2 Object Selection

This section defines properties for muons, electrons and jets used within this analysis. The official reconstruction provides candidates for each particle group which are candidates for the objects used in the event selection. All object candidates start from the final output of the particle flow reconstruction, see Section 5.5. This section starts with muons having a bright signature, followed by electrons and jets and closes with the definition of missing transverse energy. In general, all leptons are required to have a minimal distance to the primary vertex of less than 1 cm in z direction.

6.2.1 Selection of muons

The muon selection starts with particle flow muon candidates. They are required to have a minimal transverse momentum of $p_T > 20 \text{ GeV}$ and maximal absolute η of $|\eta| < 2.4$. Its track has to pass the tracker and global muon requirements, and should fulfill

the PromptTight criterion. Furthermore, its track has to fulfill the following quality requirements:

- The $\chi^2/ndof$ of the global track has to be lower than 10
- The number of valid hits has to be greater than 10
- The impact parameter with respect to the beamspot has to be less than 0.02 cm.

Finally the muon candidate is required to be isolated, which is defined by a relative isolation of the sum of the charged hadron, neutral hadron and photon isolation divided by the candidate momentum. The isolation is computed by the Particle Flow algorithm, see Section 5.5. The algorithm subtracts charged contributions by pile-up and calculates the isolation by using a ΔR cone of 0.3. The above defined isolation divided by the transverse momentum has to be less than 0.2.

6.2.2 Selection of electrons

Electron candidates are built from particle flow electrons. They are required to have a minimal transverse momentum of $p_T > 20 \text{ GeV}$ and a maximal absolute η of $|\eta| < 2.5$. Their track, reconstructed by the GSF algorithm, should have an impact parameter w.r.t. to the beam spot of less than 0.04 cm. In order to reject electrons originating from photon conversions and selecting electrons from the hard interaction, the number of missing hits in the tracking system should be at most one. No minimal number of hits is required, because the number of possible hits is at least 13 and depends on the direction of flight, see Figure 3.4 and for details Figure 3.5 and Figure 3.6. Additional discrimination against electrons from conversion is achieved by the partner track method on the electron track. This method calculates the distance, d , of all combinations of the electron candidate tracks and all its opposite sign tracks in the r - ϕ -plane, according to:

$$d = \left| |\vec{r}_{\text{trk el.}} - \vec{r}_{\text{trk}}| - r_{\text{trk el.}} - r_{\text{trk}} \right|. \quad (6.1)$$

Subsequently the distance in the r - z -plane, $\Delta \cot \theta$, is calculated using

$$\Delta \cot \theta = \left| \frac{1}{\tan \theta_{\text{trk el.}}} - \frac{1}{\tan \theta_{\text{trk}}} \right|. \quad (6.2)$$

In both equations $\vec{r}_{\text{trk el.}}$ and $r_{\text{trk el.}}$ denote the radial vector and the radius of the electron track. The radial vector and radius of an opposite electron sign track are denoted respectively, as \vec{r}_{trk} and r_{trk} . The angle θ is defined according the CMS coordinate system, see Section 3.2.1. If a combination exists with $d < 0.02 \text{ cm}$ and $\Delta \cot \theta < 0.02$, it is rejected, because it is considered to originate from a photon conversion. More technical details concerning the photon-electron rejection are given in [109, 110]. Furthermore, a minimal distance of $\Delta R > 0.1$ is required between electron and any muon passing the global or tracker identity. Finally its relative isolation should be less than 0.17. The relative isolation is defined similar to the muon relative isolation, see Section 6.2.1.

6.2.3 Selection of jets

The jets are reconstructed using particle candidate jets built using the anti- k_T algorithm, with an $R = 0.5$. These jet candidates are energy corrected until correction level three as described in Section 5.3.2. The kinematic requirements of a transverse momentum $p_T > 30 \text{ GeV}$ and $|\eta| < 2.5$ are applied. In order to suppress jets reconstructed from electronic noise the fractions of energy contributions from the calorimeters is restricted. Similar to the loose jet identity the energy contribution from charged hadronic energy has to be greater than 0 % and the contribution from charged electromagnetic, neutral electromagnetic and neutral hadronic energy has to be less than 99 %. At the end, jets are discarded, which are within a ΔR cone of 0.4 of selected leptons. The following subsection discusses the modeling of b -tagging in Monte Carlo compared to data.

b -Jet identification

The $t\bar{t}$ signal contains two b quarks within the hard process therefore the number of b jets in the total event is enriched and is a promising selection criterion. This analysis uses the Combined Secondary Vertex (CSV) b -tagging algorithm, described in Section 5.3.3, to improve rejection of background process events by requiring a minimal b -tag discriminator value of 0.244. This value is called the loose working point (CSVL), because it has a high efficiency for jets originating from b quarks and an acceptance of 10 % for light flavored jets. This b -tag algorithm has very similar performance in data and Monte Carlo events with an efficiency scale factor close to 1, see [105]. Small differences from one are taken into account by varying the scale factor within its errors of $sf_{b\text{-tag}} = 1.01 \pm 0.03$. This uncertainty is obtained by the method described in [111] and is compatible to the scale factors presented in [105]. These scale factors are applied to Monte Carlo events by event weights. This analysis defines b -jets as a jet with a discriminant value higher than CSVL working point.

6.2.4 Selection in Transverse Missing Energy

The missing transverse energy is calculated using particle flow objects, see Section 5.4 and Section 5.5. This analysis applies no corrections to the MET calculation and therefore uses the so-called “raw” MET.

6.3 Event selection

At the beginning of this section the required number of particle candidates are outlined and at the end, techniques of data-driven background estimations and scale factors are described. In general, an event is required to fire a dileptonic trigger, more details are given in the next Subsection 6.3.1, and to have a good reconstructed vertex. If the primary vertex is contained within a cylinder with a length of 24 cm and a radius of 2 cm it is considered as a good reconstructed vertex. This selection is based on the signature of top quark pair events decaying to e/μ final states, which are characterized by the

presence of two highest- p_T isolated leptons originating from W boson decays associated with a large missing transverse energy and two additional b -jets. A similar top quark pair selection is presented in [112].

6.3.1 Trigger selection

The event selection is using dileptonic, electron and muon, triggers which correspond to the signal decay channel. The general trigger techniques used by the CMS collaboration are described in Section 3.2.6. The used trigger paths require two muons or electrons or one electron and one muon. The kinematic requirements of the triggers rose during the run period in 2011 due to the increasing instantaneous luminosity. Therefore, the trigger paths used in this analysis change for different run periods. The minimal trigger thresholds requires 8 GeV of transverse momenta and a minimal isolation for electrons. More technical details: trigger names, kinematic and isolation values and run ranges of the trigger used for data taking of this analysis are listed in Table A.5. The triggers used to study the trigger selection in Monte Carlo are listed in Table A.6.

6.3.2 Lepton pair selection

Events having more than two selected leptons are classified into the three signal channels by a transverse momenta sum assignment. The assignment is done maximizing the sum of the transverse momenta of all lepton pairs with opposite charge. In addition an invariant lepton pair mass of $m_{ll} > 20$ GeV is required to suppress low invariant Drell-Yan processes. A fiducial trigger requirement is applied to channels containing signal muons, requiring that at least one of the selected signal muons fulfills the condition $|\eta| < 2.1$. The mass of the chosen lepton pair has to be outside of Z mass resonance of $m_{ll} \notin [76, 106]$ GeV if the leptons have the same flavor.

6.3.3 Jet and MET selection

The event selection continues with non leptonic features of the signal signature. All three signal channels contain two b quarks which transform in two jets and also two neutrino originating from the W boson decay. Therefore, events are required to contain two jets with the properties described in Section 6.2.3. Additionally, one of these jets has to be considered as b -jet as outlined in Section 6.2.3. Finally the event is required to have a “raw” missing transverse energy, see Section 6.2.4, of $\cancel{E}_T > 40$ GeV if it is categorized as $\mu\mu$ or ee event. This last step reduces the amount of Z boson production events.

6.4 Applied Monte Carlo Corrections

This section describes applied methods to correct insufficient Monte Carlo modeling of data. Firstly, the applied pile-up reweighting technique is outlined followed by data-driven background estimations. At the end trigger and lepton identification efficiencies are investigated.

6.4.1 Pile-up Reweighting procedure

The Pile-up is heavily dependent on the proton beam parameters, e.g. number of protons per bunch and the beam size at the collision point. Therefore, the pile-up increased during the run period of 2011 and no a priori pile-up expectation for the total run period could be provided for simulation. This analysis uses the number of reconstructed vertices to estimate the quality of pile-up modeling and investigates it at several stages of the selection, see Figure 6.6. The insufficient pile-up modeling is corrected by applying event weights and reweighting Monte Carlo events according to the pile-up measured in data. A detailed description of the reweighting applied on simulated background processes is given in [113] and is called “3D pile-up reweighting”. This procedure is requiring that in-time and out-of-time pile-up is simulated in Monte Carlo events. The according pile-up simulation scenario which is used during the Monte Carlo simulated is called “PU_S6” and only available in FullSim. Since private samples are using FastSim, which is not simulating out-of-time pile-up, the 3D pile-up reweighting is not available. Therefore, the “2D pile-up reweighting” is used for the samples related to systematic uncertainties of top quark modeling. Therefore the pile-up reweighting technique considers only in-time pile-up. The small observed difference in the number of reconstructed vertices shown in

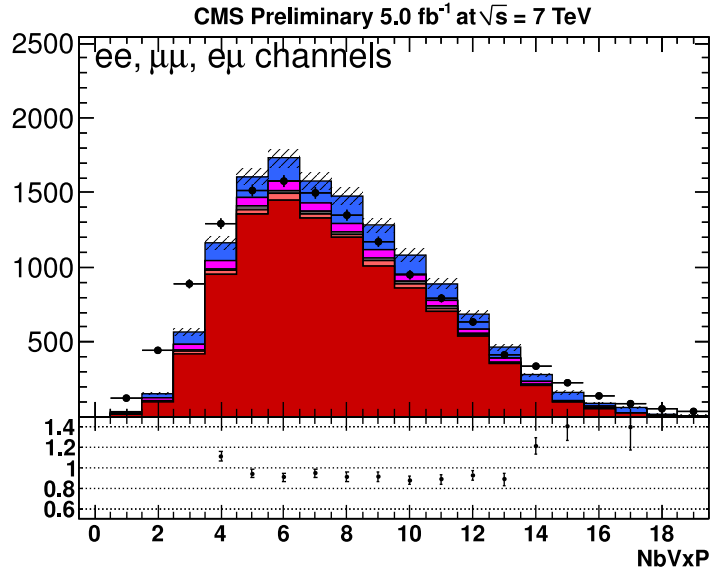


Figure 6.6: Number of reconstructed vertices in data of $\mathcal{L}_{\text{int.}} = 5.0 \text{ fb}^{-1}$ and Monte Carlo simulation after the dileptonic selection. All three signal channels are summed.

Figure 6.6 is corrected by the described pile-up reweighting techniques.

6.4.2 Lepton trigger and identification efficiency

The trigger efficiency for dileptonic events that pass the analysis selection criteria is determined using a “tag-and-probe” method as described in [114, 115]. The efficiencies for events selected by the analysis selection and passing the trigger of the according channel is 100 %, 95 % and 90 % for the ee , $e\mu$, and $\mu\mu$ channel respectively. These efficiencies are slightly depending on p_T and η . Due to the different set of triggers used in data and Monte Carlo, see Table A.5 and Table A.6, the obtained trigger efficiencies are different. The trigger efficiencies in data are estimated by a sample selected with MET triggers, which are weakly correlated to dileptonic triggers. The following scale factors between Monte Carlo and data are obtained for the three channels: $sf_{\text{trig}}^{\mu\mu} = 0.977 \pm 0.015$, $sf_{\text{trig}}^{ee} = 0.962 \pm 0.016$, and $sf_{\text{trig}}^{e\mu} = 1.008 \pm 0.009$ respectively. This method is outlined in [22]. The corresponding event weights are applied to Monte Carlo event yields for each channel separately. The lepton selection efficiencies for reconstruction, identification, and isolation are consistent between data and simulation. The obtained results are additionally confirmed by [22, 115]. For each signal channel the efficiencies for lepton reconstruction, identification and isolation are estimated using Z boson events and a “tag-and-probe” method, as described in [22]. The efficiencies are determined as a function of the lepton p_T and η and from this the corresponding data to Monte Carlo scale factors $sf_{\text{rec, iso, id}}$ are obtained. In total, this procedure estimates the following scale factors for the three signal channels: $sf_{\text{rec, iso, id}}^{\mu\mu} = 0.997 \pm 0.005$, $sf_{\text{rec, iso, id}}^{ee} = 0.995 \pm 0.003$ and $sf_{\text{rec, iso, id}}^{e\mu} = 0.994 \pm 0.005$. These scale factors are applied to Monte Carlo events selected by the corresponding sub-selection.

6.5 Data-driven Background Estimation

Except for the diboson and single top processes, the event yields of background processes, see Section 6.1, are estimated by data-driven techniques. The dominant Drell-Yan background is estimated by the $R_{\text{out/in}}$ method and a template fit of the invariant mass of the lepton pair. Processes related to the presence of a fake lepton or a lepton with a fake isolation, called “non-prompt lepton”, are estimated using the tight-loose method. This category contains the semileptonic and full hadronic $t\bar{t}$ decays, W +jets and QCD processes. A summary of these techniques is given in this section and more technical details of the data-driven estimation techniques are given in [22].

6.5.1 Drell-Yan background estimation

The data-driven Drell-Yan background estimation is using two different techniques for the different channels. First the $R_{\text{out/in}}$ method used for the same lepton flavor, ee and $\mu\mu$, channels is described followed by the template fit method which is applied to the opposite flavor channel. Both techniques are outlined and validated in [116].

The $R_{\text{out/in}}$ Drell-Yan estimation method is based on the idea of comparing the number of two regions in the invariant-lepton-pair-mass spectrum. One region is defined at the Z resonance and called “inside region”. The region of the remaining mass spectrum is

called respectively “outside region”. The inside region is defined as the Z -veto region used in the lepton pair selection, see Section 6.3.2. The event-number yield of the outside region is estimated from the yield of the inside region by measuring the ratio of the event yield of the two regions from Monte Carlo events. The event yield in the outside region is measured from data by:

$$N_{\text{out}}^{l^+l^-,\text{obs}} = R_{\text{out/in}}^{l^+l^-} (N_{\text{in}}^{l^+l^-} - 0.5N_{\text{in}}^{e\mu} k_{ll}) , \quad (6.3)$$

where $ll = \mu\mu$ or ee and $R_{\text{out/in}}$ is the ratio of the number of the event yields of the outside/inside region defined by:

$$R_{\text{out/in}} = \frac{N_{\text{DY MC}}^{\text{out}}}{N_{\text{DY MC}}^{\text{in}}} . \quad (6.4)$$

The correction factor k is applied to take into account the differences between electron and muon reconstruction and is calculated using events in the Z peak region passing the standard dilepton and jet selections, without any MET cut, and is expressed by:

$$\begin{aligned} k_{ee} &= \sqrt{\frac{N_{\text{in}}^{e^+e^-}}{N_{\text{in}}^{\mu^+\mu^-}}} , \\ k_{\mu\mu} &= \sqrt{\frac{N_{\text{in}}^{\mu^+\mu^-}}{N_{\text{in}}^{e^+e^-}}} . \end{aligned} \quad (6.5)$$

The contamination from non Drell-Yan background events in the inside region is subtracted from the $e\mu$ channel and then scaled according to the event yields in ee and $\mu\mu$ channels. The dependence of $R_{\text{out/in}}$ as a function of the number of vertices and the jet multiplicity is studied. The purity of the Drell-Yan events is estimated by the fraction $N_{\text{DY}}/N_{\text{all MC}}$ using Monte Carlo events. Out of these control regions, $R_{\text{out/in}}$ is obtained for Monte Carlo and data separately and a correction factor $sf_{R_{\text{out/in}}} = R_{\text{out/in}}^{\text{data}}/R_{\text{out/in}}^{\text{MC}}$ is estimated. The following scaling factors are obtained for same lepton flavor channels separately: $sf_{R_{\text{out/in}}^{ee}} = 1.050 \pm 0.001$ and $sf_{R_{\text{out/in}}^{\mu\mu}} = 1.076 \pm 0.001$. The Drell-Yan event yields for the different selection steps are summarized in Table 6.1. The given errors are considering statistics only and the errors of correction factors f are taken into account.

The “template fit method” is applied to the $e\mu$ channel, whose Drell-Yan contribution is predominantly originating from the process $Z/\gamma^* \rightarrow \tau^+ \tau^- \rightarrow e^+ \nu_e \bar{\nu}_\tau \mu^- \bar{\nu}_\mu \nu_\tau$. The cross section of this process is significantly lower than the inclusive Drell-Yan cross section. Therefore the overall background contamination is small. In addition, because of the presence of neutrinos created by the τ decays, the dileptonic invariant mass is not compatible with the known Z boson mass and the peak is shifted to a lower mass range. In order to estimate the overall Drell-Yan contamination in the $e\mu$ channel a binned “template” likelihood fit of the dileptonic invariant mass distribution is applied. The fit is executed using the RooFit [117] package. The templates used within the fit are extracted from Monte Carlo for signal and background process. The fit is performed after the jet multiplicity selection and before the missing transverse energy requirement, see Section 6.3. The results of the fits are presented in Figure 6.7 and the corresponding data/MC scale factors are shown in Table 6.2.

Table 6.1: The Drell-Yan event estimates and obtained scale factors.

channel	$R_{\text{out/in}}$	DY MC	DY pred	sf
ee , NJets ≥ 2	0.136 ± 0.009	4610 ± 68	5257 ± 336	1.140 ± 0.073
ee , $\cancel{E}_T \geq 40$	0.162 ± 0.015	199 ± 14	329 ± 67	1.654 ± 0.339
ee , NBjets ≥ 1	0.163 ± 0.020	85.3 ± 9.2	149 ± 32	1.745 ± 0.374
ee , NBjets ≥ 2	0.190 ± 0.043	19.5 ± 4.4	40 ± 12	2.027 ± 0.601
$\mu\mu$, NJets ≥ 2	0.142 ± 0.009	6030 ± 78	7056 ± 427	1.170 ± 0.071
$\mu\mu$, $\cancel{E}_T \geq 40$	0.217 ± 0.017	334 ± 18	512 ± 109	1.532 ± 0.325
$\mu\mu$, NBjets ≥ 1	0.206 ± 0.020	134 ± 12	202 ± 46	1.510 ± 0.341
$\mu\mu$, NBjets ≥ 2	0.212 ± 0.039	26.5 ± 5.1	32 ± 12	1.210 ± 0.441

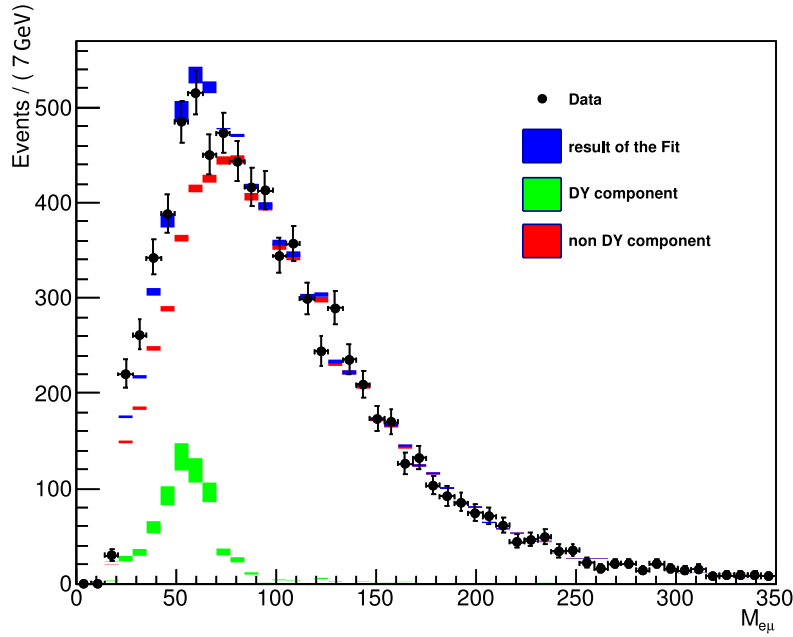


Figure 6.7: Results obtained from the Drell-Yan template fit of the dilepton invariant mass in the $e\mu$ channel, after jet multiplicity selection. Data is shown as black dots, the blue area corresponds to the fit result, the green area and the red area correspond to the Drell-Yan component and contributions from other processes estimated by the fit. The width of the area denotes the statistical uncertainty.

Table 6.2: Data to Monte Carlo scale factors obtained by the template fit method.

	expected	predicted	data/MC ratio
after jet selection	371 ± 31	656 ± 70	1.77 ± 0.24

6.5.2 Fake lepton estimate

The fake lepton background contribution is estimated using the “tight-loose method” which is presented in [118, 119, 120] and sometimes called “matrix method”. This method measures the background from misidentified leptons or from true leptons that pass the isolation requirement, but correspond to semi-leptonic decays of b or c hadrons contained within jets. True isolated leptons are called “prompt” leptons. Therefore these leptons, which fake a good isolation, are called “non-prompt” leptons in the following. Three categories of backgrounds are defined: $t\bar{t}$ signal-like, W +jets-like and multi-jet processes, containing two, one, and no prompt leptons, respectively. The $t\bar{t}$ signal-like sample contains $t\bar{t}$ signal events, but also Drell-Yan, single top-quark and di-boson events. The W +jets-like category consists of W +jets events and semileptonically decaying $t\bar{t}$ events. The multi-jet category is mainly built of multi-jet events from direct QCD production and of full-hadronic $t\bar{t}$ decays. The number of selected events for each category can be estimated by defining three sets of selections for dileptonic pairs with different lepton isolation requirements. The lepton isolation is relaxed from $I_{\mu, \text{rel}} < 0.20$ and $I_{e, \text{rel}} < 0.17$ for muons and electrons, respectively, of the $t\bar{t}$ signal-like category to $I_{\text{rel}} < 0.8$ for both flavor of leptons, called “loose” leptons. The three categories define different dileptonic samples containing so-called loose, medium, and tight events. They are built of events containing, respectively, two loose, at least one tight, and two tight isolated leptons. The tight sample contains the events used for the later spin correlation measurement. A system of equations is constructed by introducing probabilities for a loose or medium event to be also categorized as medium or tight event. The solution of this system of equations estimates the number of $t\bar{t}$ signal-like, W +jets-like and multi-jet events. The prompt lepton efficiencies are estimated using Z events in data, similarly to the method presented in Section 6.5.1. The corresponding systematic uncertainties are taken conservatively as 50% of the difference between the efficiency measurements in data and the predictions of the Monte Carlo simulation. In order to obtain a sample of a statistically reasonable size the estimated number of W -like events and multi-jet events is estimated before any b -tagging requirement is applied. These event numbers are called N_W and $N_{\text{multi-jet}}$, respectively. The results for N_W and $N_{\text{multi-jet}}$ are presented in Table 6.3. The uncertainties account for the statistical uncertainty and for the systematic uncertainties of the efficiencies for prompt and non-prompt loose leptons to pass the tight isolation requirement. The effect of the b -tag selection is introduced by applying the b -tag efficiencies and mistag rates, as predicted by the Monte Carlo simulation, to the results shown in Table 6.3 obtained without any b -tagging requirement. The final event numbers N_W and $N_{\text{multi-jet}}$ are presented in Table 6.4 and denote the estimated

Table 6.3: Estimated number of W -like, N_W and multi-jet, $N_{\text{multi-jet}}$ events before any b -jet requirement.

	ee	$\mu\mu$	$e\mu$
N_W	20.5 ± 12.0	35.6 ± 7.1	154.7 ± 33.7
$N_{\text{multi-jet}}$	1.5 ± 1.1	1.5 ± 0.9	40.2 ± 18.8

event numbers after requiring at least one b -jet in the events.

Table 6.4: Estimated number of W -like, N_W and multi-jet $N_{\text{multi-jet}}$ events containing at least one b -jet.

	ee	$\mu\mu$	$e\mu$
N_W	4.7 ± 12.7	23.4 ± 13.4	102.8 ± 35.4
$N_{\text{multi-jet}}$	1.3 ± 1.1	0.8 ± 0.4	14.3 ± 7.4

6.6 Distortion of Spin Correlation Effects by the Selection

In order to estimate the influence of the selection on a $t\bar{t}$ spin correlation measurement, the dilution of the $\Delta\phi$ distribution, see Equation 2.5 and Figure 2.11, of the two leptons is investigated. The resulting $\Delta\phi$ distributions after application of the event selection are separately shown for the three signal channels Figure 6.8. The comparison to the Standard Model estimation without any requirements, see Figure 2.11, shows a distortion of the $\Delta\phi$ distribution. But a clear separation between the Standard Model expectation and the assumption of no spin correlations in dileptonic top quark pair decays is preserved. Therefore, the above outlined selection is suitable for a spin correlation measurement. In order to validate that the separation between a scenario with and without spin correlations is only observed in the $\Delta\phi$ distribution, the invariant lepton pair mass is investigated. The same set of selected events are studied and the results for the three channels are shown in Figure 6.9. No significant difference m_{ll} is observed and confirms the application of the event selection.

6.7 Comparison of Data and Monte Carlo Simulation

The selection, Monte Carlo modeling, and data-driven background estimations are validated by comparing event yields and event kinematics for data and Monte Carlo estimation. Each variable is investigated for each channel separately and for the sum of all three channels. The invariant lepton pair mass of events selected after the jet

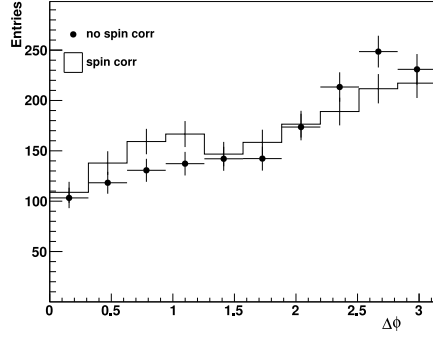
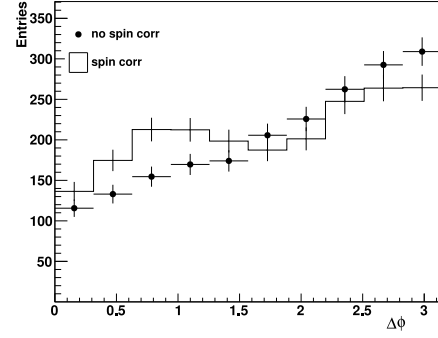
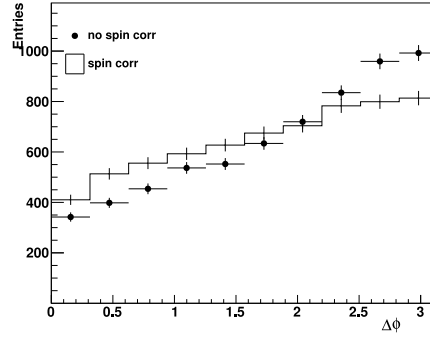
(a) ee channel(b) $\mu\mu$ channel(c) $e\mu$ channel

Figure 6.8: The $\Delta\phi$ distribution of the signal channels after requiring at least one b -jet, comparing $t\bar{t}$ events produced with and without top quark pair spin correlation.

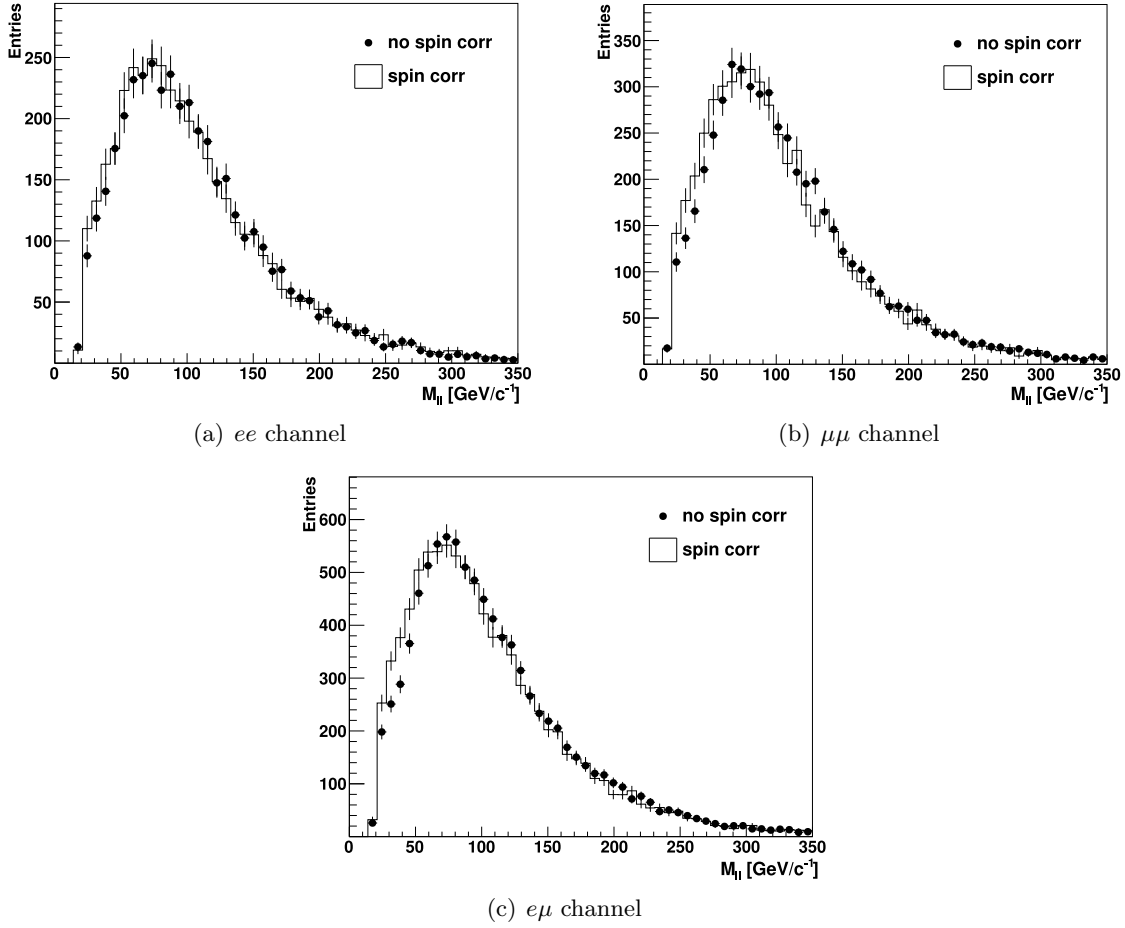


Figure 6.9: Dilepton invariant mass, m_{ll} , distribution of the three signal channels after the lepton event selection, comparing $t\bar{t}$ events produced with and without top quark pair spin correlation.

multiplicity requirement shows a good agreement of data and Monte Carlo modeling, see Figure 6.10. The “gap” in the same lepton flavor channels is related to the z mass veto region of the event selection for these channels. The displayed Monte Carlo versus data ratio shows a good agreement. The next kinematic variable, the momentum of the first leading lepton and second lepton is shown divided in lepton flavors in Figure 6.11. Events entering these plots are selected after the MET requirement and the scale factor for trigger efficiencies and lepton selection efficiencies and data driven background estimations are used. The displayed Monte Carlo to data ratio shows good agreement. Overall the lepton kinematics modeling in Monte Carlo reasonably resembles the measurement within data.

The next set of validation variables are related to jet modeling. Similar to the lepton variables the momenta are compared channel-wise and the estimated jet multiplicity of the selected events is investigated. The momenta are shown for the leading, see Figure 6.12, and second leading jet, see Figure 6.13, separately. The shown events are selected after the MET requirement and the scale factor correction for trigger, lepton and MET efficiencies are applied. The above described data-driven background estimations are also applied. No significant deviations between data and Monte Carlo are found for the jet multiplicity or the momenta of the leading and second leading jet.

Finally the MET expectation from Monte Carlo and data is compared. Due to its construction this variable is very sensitive to any significant difference of event kinematics, because it is built from all objects reconstructed with the event, see Section 5.4. In Figure 6.15, the missing transverse energy distribution is shown after the jet multiplicity requirement. A small deviation between data and Monte Carlo is present at small MET values lower than 40 GeV. This MET region is negligible for the presented analysis, because a MET requirement of 40 GeV is required, see Section 6.3.3. The data modeling of Monte Carlo is reasonable for the rest of the MET distribution and no significant differences are observed.

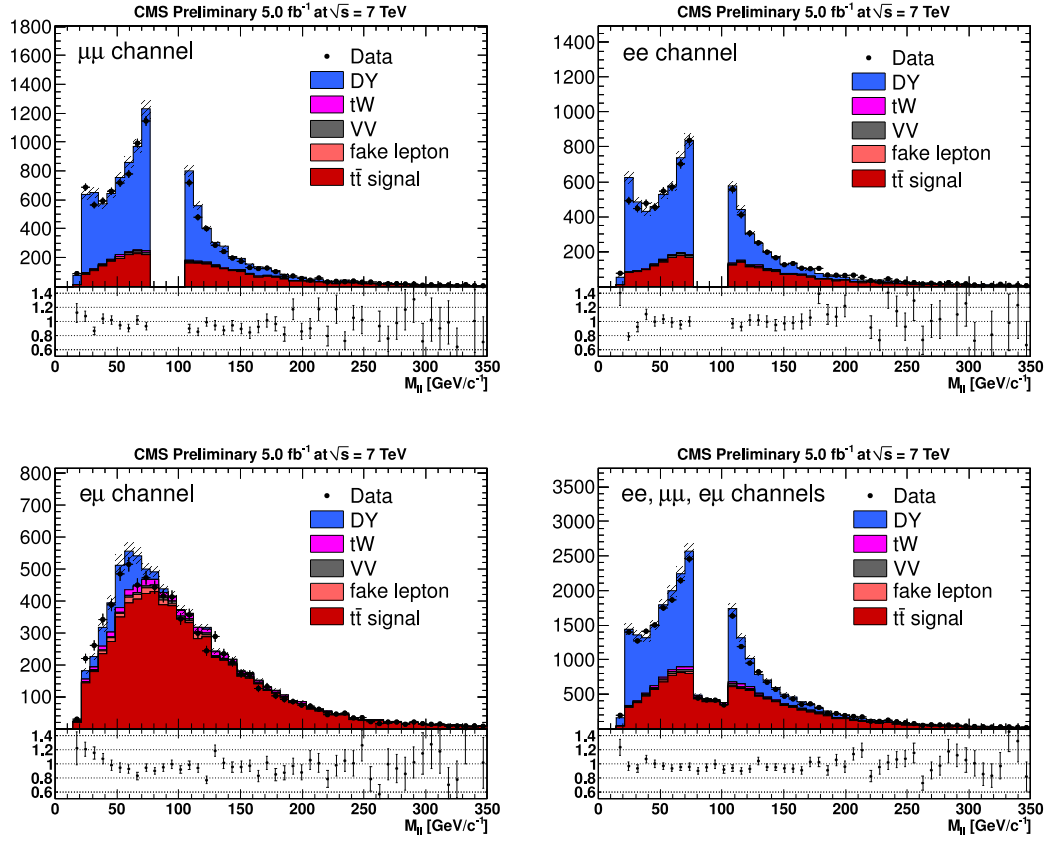


Figure 6.10: Distribution of the dilepton invariant mass in the three lepton-lepton channels, and for the overall combination after the jet multiplicity cut. Scale factors for trigger, lepton selection, and data driven background estimations are applied. The hatched area corresponds to the scale factor uncertainties with an uncertainty of 4.5 % on luminosity.

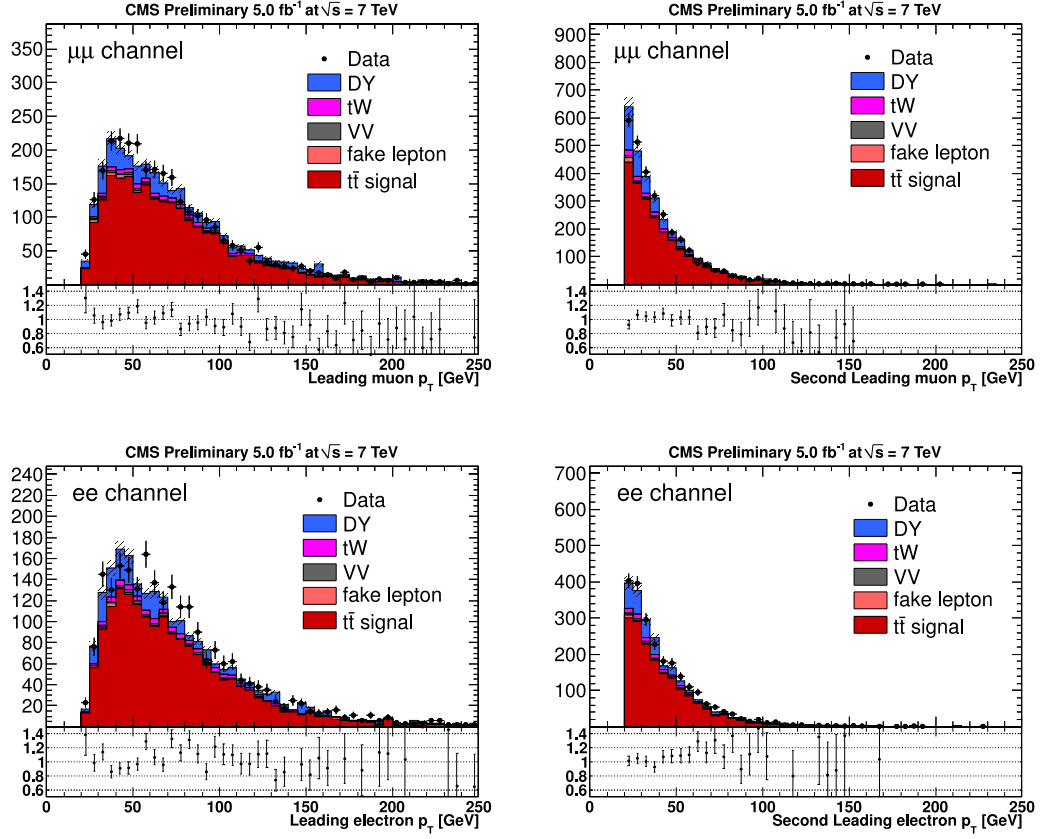


Figure 6.11: Distributions of the muon (upper plots) and electron (lower plots) p_T after applying in the MET requirement. Scale factors for trigger, lepton selection, and data-driven background estimations are used. The hatched area corresponds to the scale factor uncertainties with an uncertainty of 4.5% on luminosity.

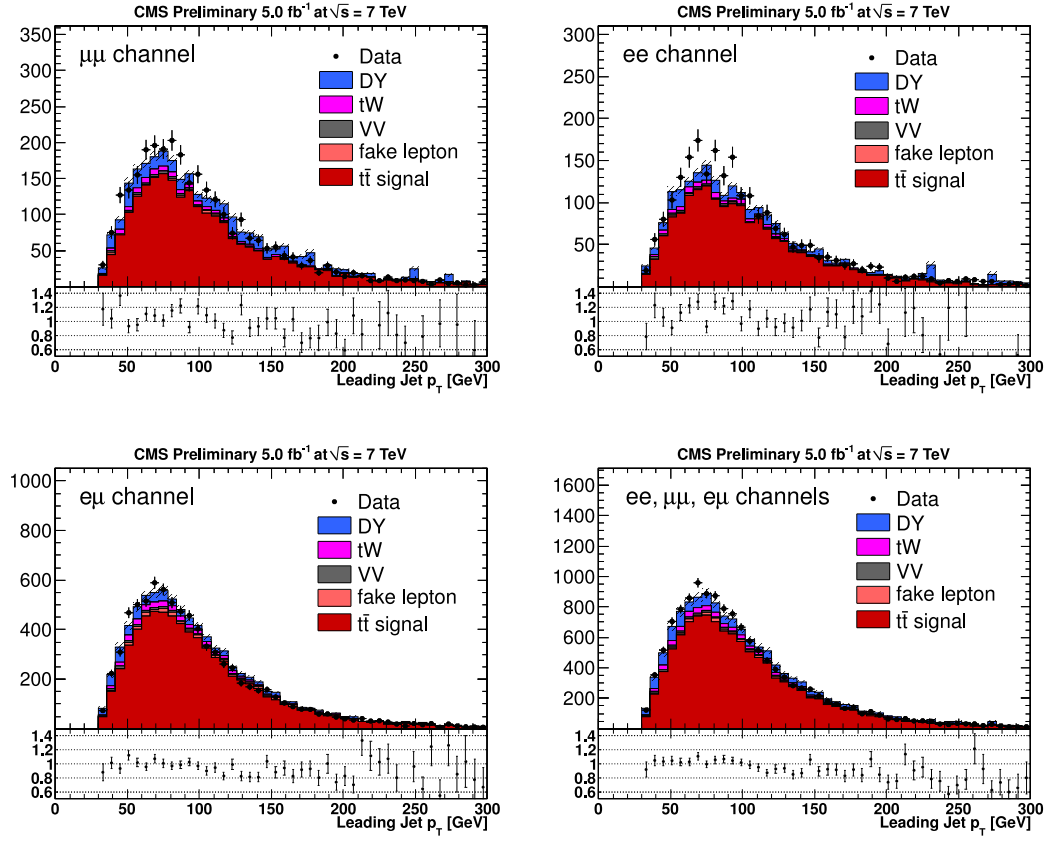


Figure 6.12: Transverse jet momenta of the leading jet in the three dilepton channels, and for the overall combination after applying the MET requirement. Scale factors for trigger, lepton selection, MET, and data-driven background estimations are used. The hatched area corresponds to the scale factor uncertainties with an uncertainty of 4.5 % on luminosity.

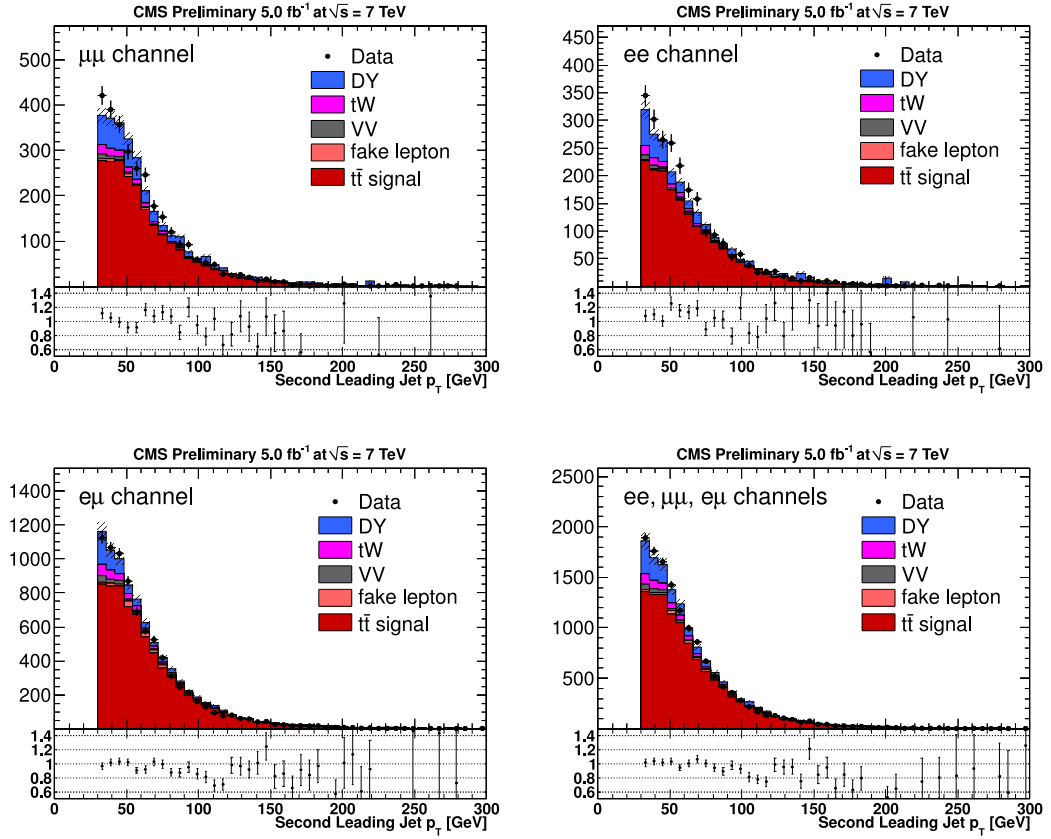


Figure 6.13: Transverse jet momenta of the second leading jet in the three dilepton channels, and for the overall combination after applying the MET requirement. Scale factors for trigger, lepton selection, MET, and data driven-background estimations are used. The hatched area corresponds to the scale factor uncertainties of 4.5 % on luminosity.

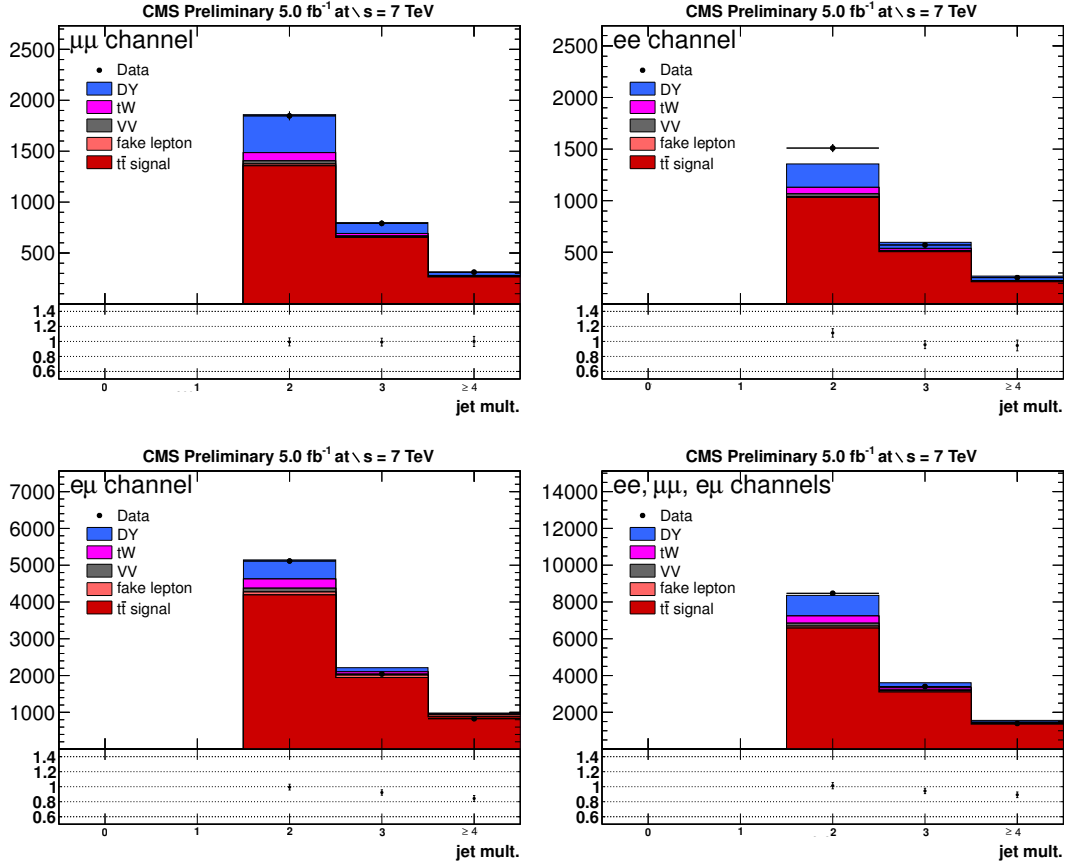


Figure 6.14: Jet multiplicity distributions in the three dilepton channels, and for the overall combination after applying MET requirement. Scale factors for trigger, lepton selection, MET, and data-driven background estimations are used. The hatched area corresponds to the scale factor uncertainties of 4.5% on the luminosity.

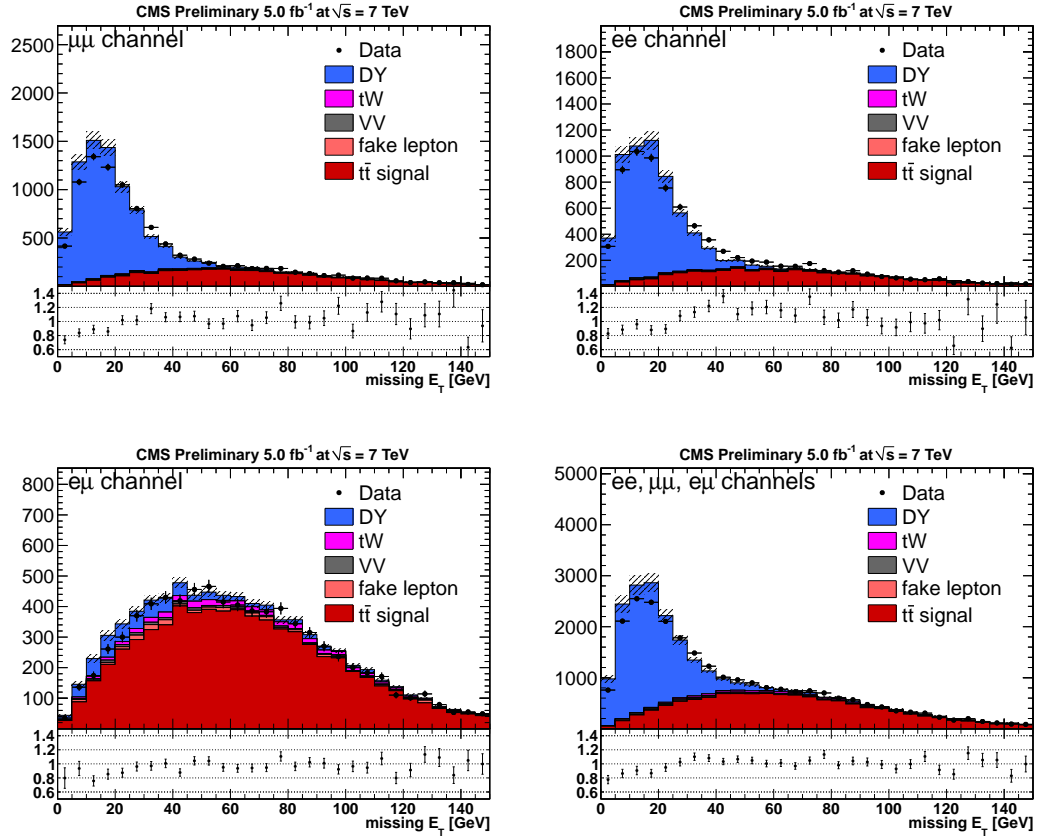


Figure 6.15: MET distributions in the three dilepton channels, and for the overall combination after the jet multiplicity cut. Scale factors for trigger, lepton selection, and data-driven background estimations are used. The hatched area corresponds to the scale factor uncertainties of 4.5 % on the luminosity.

Chapter 7

Spin Correlation Extraction

This chapter outlines the procedure to interpret the top quark spin correlations from the selected data. A template fit of the $\Delta\phi$ distributions of the three signal channel is made and validated. At the end a closure test result is presented and discussed.

7.1 Applied Template Fit

The first part of the following section describes the applied fit function and method. At the end a comparison of selected data events and the two used templates are shown. The second part summarizes the technical implementation in RooFit [117].

7.1.1 Fit Function and Templates

The applied fit is preformed in three dileptonic channels individually, which are denoted by $ll = \mu\mu, e\mu, ee$. In each channel, a template fit of three templates is performed, see Equation 7.1.

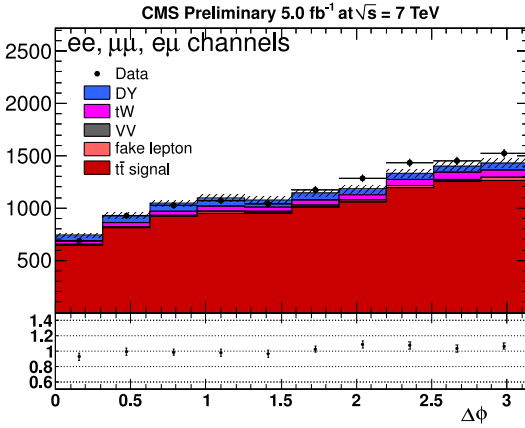
$$\frac{d\sigma^{ll}}{d\Delta\phi} = N_{\text{sig}}^{ll} \cdot \left(f^{\text{SM}} \cdot P_{t\bar{t} \text{ corr}}^{ll}(\Delta\phi) + (1 - f^{\text{SM}}) \cdot P_{t\bar{t} \text{ no-corr}}^{ll}(\Delta\phi) \right) + N_{\text{bkg}}^{ll} \cdot P_{\text{bkg}}^{ll}(\Delta\phi) . \quad (7.1)$$

Each template corresponds to a different contribution to the $\Delta\phi$ distribution. The first template, denoted by $P_{\text{bkg}}^{ll}(\Delta\phi)$, represents the $\Delta\phi$ distribution of the background processes. The second $P_{t\bar{t} \text{ corr}}^{ll}(\Delta\phi)$ and third $P_{t\bar{t} \text{ no-corr}}^{ll}(\Delta\phi)$ template models the $\Delta\phi$ distribution of top quark pair events with a Standard Model like spin correlation and the assumption of no spin correlation. These three types are abbreviated by: bkg, $t\bar{t}$ corr and $t\bar{t}$ no-corr. The two templates describing $t\bar{t}$ events are weighted by the factor f^{SM} and $(1 - f^{\text{SM}})$ which ensures that the sum of the two templates is equal to unity. Furthermore, this factor later displays the fraction of Standard Model expectation contained in the data. The template fits of all three channels are executed simultaneously and share the same Standard Model expectation factor f^{SM} . The fit variables are the number of signal events in each channel $N_{\text{sig}}^{ll} = N_{\text{sig}}^{\mu\mu}, N_{\text{sig}}^{e\mu}, N_{\text{sig}}^{ee}$ and the fraction of

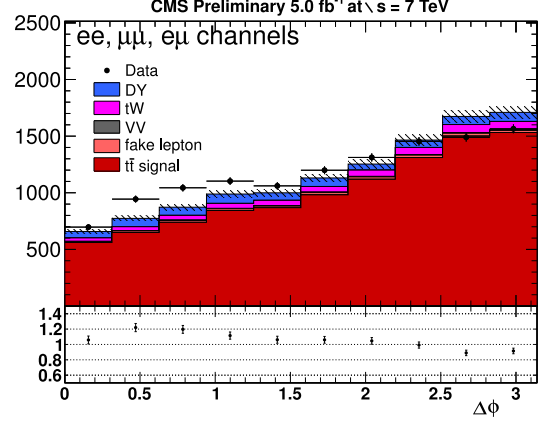
Standard Model expectation f^{SM} . The templates $P_{t\bar{t}\text{corr}}^{\text{ll}}$ and $P_{t\bar{t}\text{no-corr}}^{\text{ll}}$ are normalized to unity since their normalization is a fit parameter.

$$P_k^{\text{ll}}(\Delta\phi) = \frac{1}{\sigma_{\text{type}}^{\text{ll}}} \frac{d\sigma_{\text{type}}^{\text{ll}}}{d\Delta\phi}, \quad \text{type} = \text{bkg}, t\bar{t}\text{corr}, t\bar{t}\text{no-corr}$$

The number of background events in each channel, $P_{\text{bkg}}^{\text{ll}}(\Delta\phi)$, is estimated from Monte Carlo and data-driven methods and has a fixed value. The $\Delta\phi$ distributions of background expectation and Standard Model expectation obtained from MC@NLO is shown in Figure 7.1(a). The equivalent distribution is shown in Figure 7.1(b), comparing the measured $\Delta\phi$ distribution with the scenario assuming no top quark pair spin correlation. Both scenarios show significant differences between the Monte Carlo expectation of $\Delta\phi$ and the according measurement in data. The assumed event yields for selected signal events are calculated using the considered integrated luminosity, selection efficiencies, data Monte Carlo corrections factors and the measured cross section for top quark pair production, see Section 2.2 and 6.4. The similar $\Delta\phi$ distribution derived from Monte Carlo simulation and considering only selected $t\bar{t}$ events is shown in Figure 6.8. Additional events from background processes and the distortion due to the detector acceptance and resolution do not dilute the different shapes of the $\Delta\phi$ distribution for top quark pair events with and without spin correlations.



(a) MC@NLO with top quark spin correlation.



(b) MC@NLO without top quark spin correlation.

Figure 7.1: The $\Delta\phi$ distributions, comparing data and Monte Carlo predictions, after selection, for $t\bar{t}$ MC@NLO events with and without top quark pair spin correlation.

7.1.2 Technical Implementation

The templates, which are described and shown above, and the corresponding model, see Equation 7.1, are implemented in a “RooWorkspace” object of ROOTFIT which is available within the ROOT [121] analysis framework. The fit uses a binned likelihood algorithm [122] to estimate the best values for the fit parameters: $N_{\text{sig}}^{\mu\mu}$, $N_{\text{sig}}^{e\mu}$, N_{sig}^{ee} and f^{SM} which are assigned as “RooRealVar” objects. The nine templates are transferred into “RooDataHist” objects and declared as “HistPdf” depending on the “RooRealVar” f^{SM} . The two templates describing the $\Delta\phi$ distribution of the Standard Model prediction and the null hypothesis are summed according to Equation 7.1 by the “SUM” assignment. By a second “SUM” statement the third template, the constant background $\Delta\phi$ distribution is added and the assumed model for each channel of Equation 7.1 is complete. The three channels are combined by the “SIMUL” statement to an simultaneous model called *model* of all three channels with the global fit parameter f^{SM} . The probability density function of the model is extracted by calling the “pdf” function of the object *model*. From this probability density the negative log-likelihood is calculated and minimized by using Minuit [123]. The minimization uses the Minuit routines MIGRAT and HESSE in succession to calculate the minimum. The MIGRAT subroutine is based on “Fletcher’s” switching variation and of the “Davidon-Fletcher-Powell” algorithm. More details are given in [123]. The HESSE subroutine is executed to derive the errors of the obtained fit parameters.

In order to be independent of the technical implementation and the used set of minimization algorithms the template fit was also executed in a complementary environment of the SciPy framework [124]. The obtained ROOT histograms were transferred in NumPy arrays. The simultaneous fit of the three channels with nine templates is implemented via a section-wise defined user function. The minimization is executed by the least square routine of SciPy’s optimize package. This method is a wrapper of the “lmdif” and “lmdr” algorithms of MINPACK [125]. More technical details and examples for implementing template fits in SciPy and its optimization routines is given in the corresponding citations and online manuals.

7.2 Template Fit Validation

The applied template fit is validated using pseudo data with different spin correlation strengths. The pseudo data is generated using different Standard Model contribution factors, denoted by $f_{\text{gen}}^{\text{SM}}$ in the range of $[-1, 2]$. The following values of Standard Model contribution are used: $f_{\text{gen}}^{\text{SM}} = -1 + k \cdot \frac{1}{3}$, $k = 0, \dots, 9$. The two $\Delta\phi$ distributions of the selected Monte Carlo top quark pair events are shown in Figure 7.1 with and without top-quark spin-correlation scenario. In both figures all signal channels are summed with the initial factor $f_{\text{gen}}^{\text{SM}}$ set to zero or one, respectively. According to the resulting $\Delta\phi$ distribution, 10,000 pseudo experiments are generated by a bin-wise fluctuation of the bin number of each $\Delta\phi$ bin. For each pseudo experiment the factor f^{SM} is estimated by

the template fit. For each assumed $f_{\text{gen}}^{\text{SM}}$ the obtained f^{SM} are saved in a histogram and their distribution is approximated by a Gaussian function. In order to check the linearity of the applied template fit, the mean value of this Gaussian function is plotted against the assumed $f_{\text{gen}}^{\text{SM}}$, see Figure 7.2(a). The displayed errors are the obtained standard deviations of the fitted Gaussian distribution. In Figure 7.2(b) the bias of the linearity between f^{SM} and $f_{\text{gen}}^{\text{SM}}$ is shown and no significant bias is observed. Furthermore, the

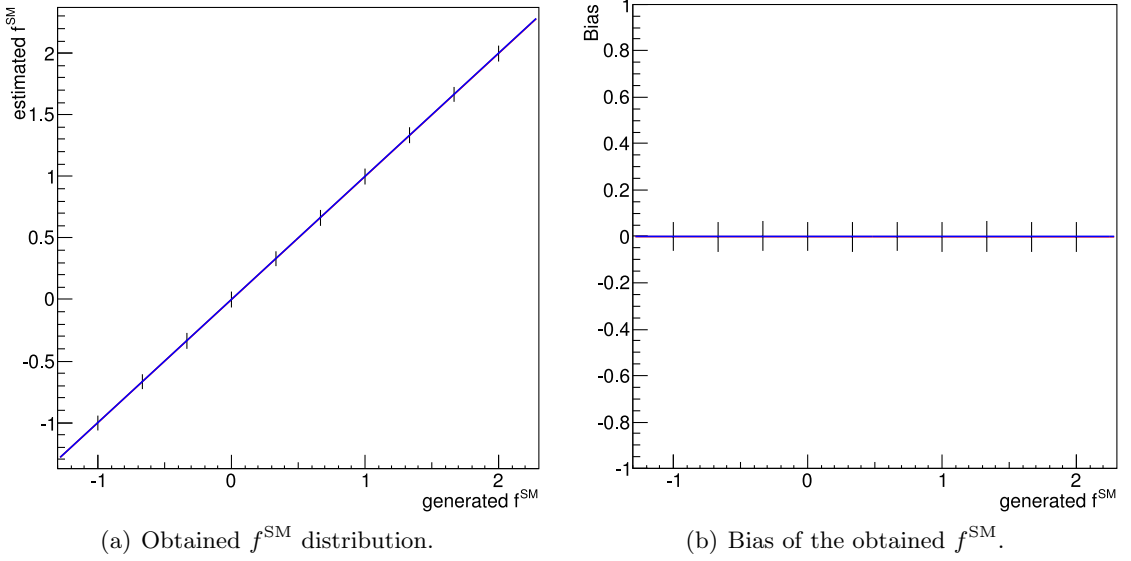


Figure 7.2: Example of the f^{SM} distribution of the estimated f^{SM} and bias as function of the generated f^{SM} .

width of the pull distributions, i.e. $(f^{\text{SM}} - f_{\text{gen}}^{\text{SM}})/\sigma_{f^{\text{SM}}}$, is presented in Figure 7.3 on the left side. The uncertainty estimation by the template fit is validated by investigating the obtained pull-distribution depending on the generated $f_{\text{gen}}^{\text{SM}}$, see Figure 7.3(b). The fit underestimates the uncertainty, since an average pull width smaller than one is obtained. As an example the pull distribution for $f_{\text{gen}}^{\text{SM}} = 1$ is shown in Figure 7.3(a) which has an estimated width of 0.92 ± 0.01 which is significantly deviating from one. This effect is considered to be a technically irrelevant feature of ROOFIT and is corrected by applying an inclusive scaling factor f_{err} to the estimated error. The factor $f_{\text{err}} = 0.932$ is obtained from the results in Figure 7.3 by approximating the obtained pull width by a constant function. By this conservative calibration all statistical uncertainties are recalculated. The estimated uncertainties, tested with pseudo experiments after calibration with f_{err} are shown in Figure 7.4. After rescaling the obtained pull widths are in agreement with a unitary expectation and the mean of the obtained pull distributions is well centered at zero.

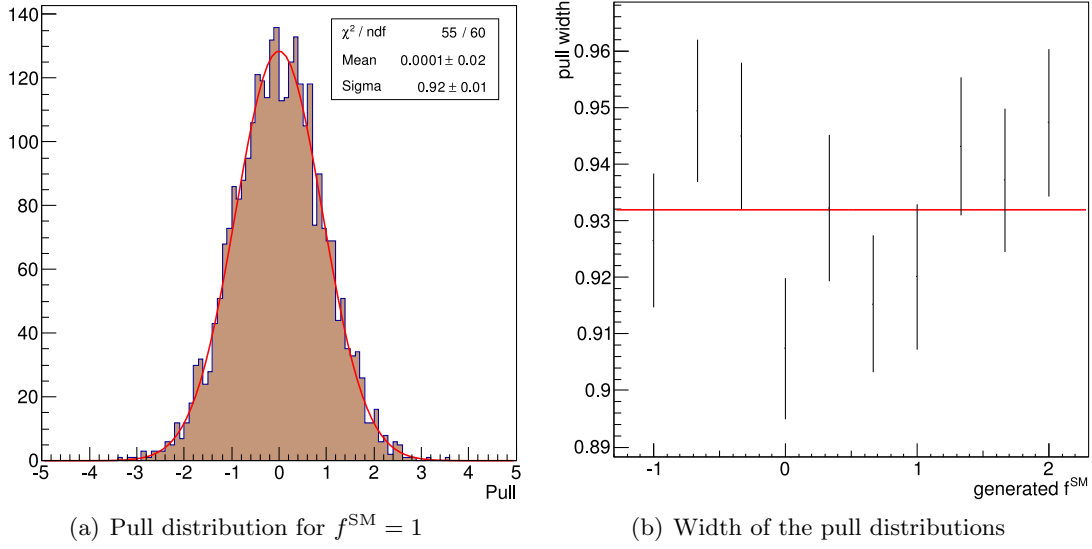


Figure 7.3: Obtained pull distribution for $f^{\text{SM}} = 1$ with statistical uncertainties and width of the pull distributions as a function of f^{SM} with statistical uncertainties.

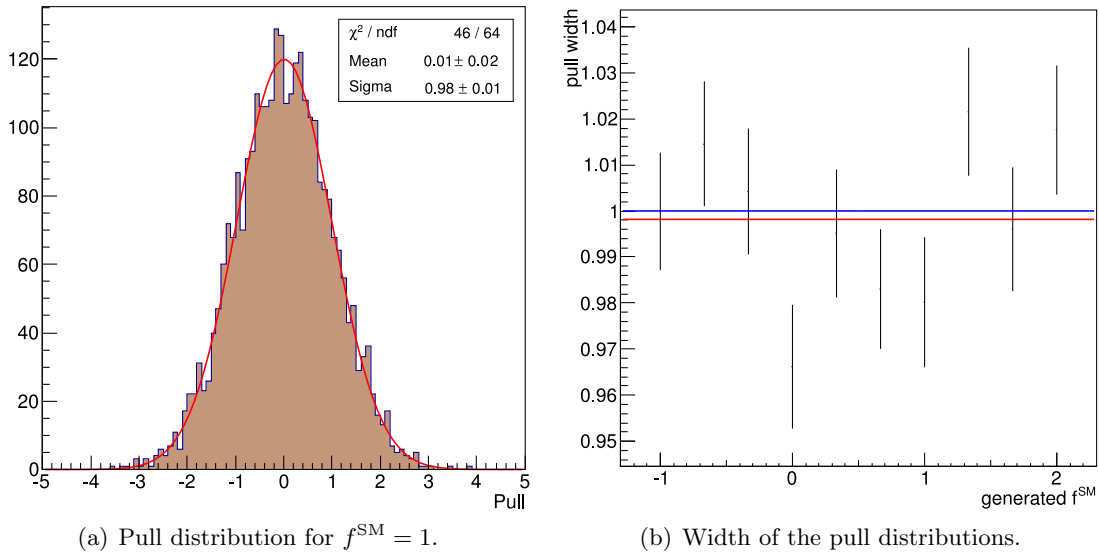


Figure 7.4: Obtained pull distribution for $f^{\text{SM}} = 1$ with rescaled statistical uncertainties and width of the pull distributions as a function of f^{SM} with rescaled statistical uncertainties.

Table 7.1: Fit results estimated by the described template fit. All uncertainties are considering only statistics.

channel	$\mu\mu$	$e\mu$	ee	all
N_{sig}	2132 ± 50	6351 ± 85	1718 ± 44	—
f^{SM}	—	—	—	0.74 ± 0.08

7.3 Template Fit Result

The result of the template fit is given in Table 7.1. The total number of background events, dominated by the Drell-Yan processes, is $N_{\text{bkg}}^{\mu\mu} = 349 \pm 175$, $N_{\text{bkg}}^{e\mu} = 744 \pm 371$ and $N_{\text{bkg}}^{ee} = 241 \pm 121$ for the $\mu\mu$, $e\mu$ and ee channels, respectively. The result of the template fit on data is presented in Figure 7.5 and was also published in [126, 127]. The

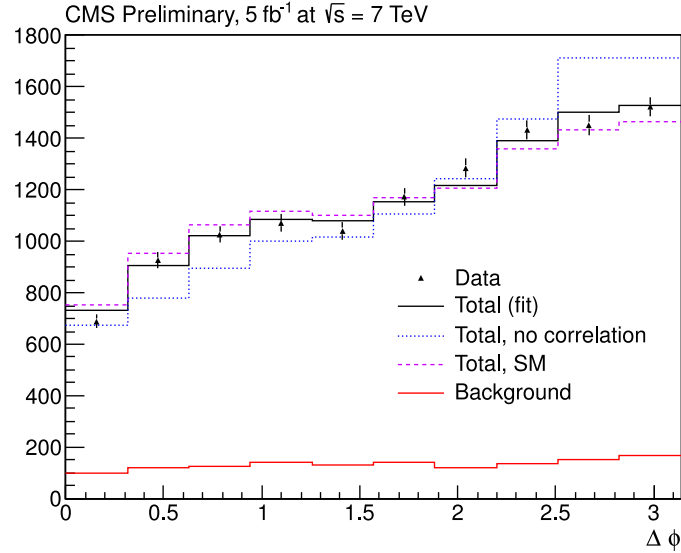


Figure 7.5: Result of the fit, solid line, performed on data, triangles, after the combination of the three channels. The data expectation is also compared to the $\Delta\phi$ distributions of $t\bar{t}$ events with and without spin correlation. Both scenarios include the $\Delta\phi$ distribution of the expected background component. The according log likelihood function is shown in Figure 7.6.

three separately and simultaneously fitted channels are combined and the two different hypotheses for top quark pair events with and without spin correlations are shown. Both scenarios show a significant difference from data but the combination with the fitted ratio of $f^{\text{SM}} = 0.74$ is in good agreement with the measured $\Delta\phi$ distribution. For illustration, the $t\bar{t}$ event yields are the number of signal events estimated by the applied template fit, see Table 7.1. The sum of the estimated $t\bar{t}$ event yields, $N_{\text{sig}}^{\text{all}} = 10201 \pm 108$, is

compatible with the Standard Model expectation of the Standard Model top quark cross section respecting the selection efficiency of the analysis. The according log likelihood function depending on f^{SM} is shown in Figure 7.6. The log likelihood function has the

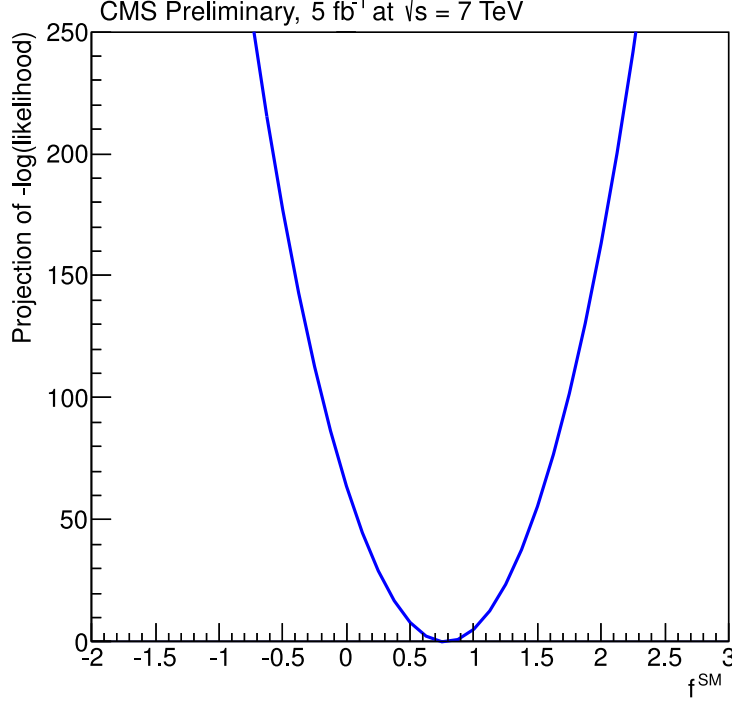


Figure 7.6: Negative Log Likelihood function depending on f^{SM} , the ratio of Standard Model and no top quark pair spin correlation expectation. The minimum is estimated to be at $f^{\text{SM}} = 0.74$ and the remaining fit parameters are listed in Table 7.1.

expected shape with one single minimum at the best fit value of $f^{\text{SM}} = 0.74$. The log likelihood functions depending on N_{sig} for the three channels have a similar behavior with the best fit value listed in Table 7.1 as single minimum.

Chapter 8

Systematic Uncertainties

This chapter discusses the systematic uncertainties related to the experimental setup, simulations and methods used. The systematic uncertainties are categorized into two groups of detector related systematics and physics related modeling. The first group influences the applied selection by uncertainties related to lepton and jet properties. This group is considering the applied lepton scale factors for isolation and selection identification, the lepton energy scale, the jet energy scale jet energy scale (JES) and jet energy resolution (JER). Finally, the normalization of background processes is discussed.

Lepton scale factors: The lepton scale factors for isolation and selection identification are compatible with one within their uncertainties, because the measured efficiency in data and Monte Carlo events is compatible. Therefore, the systematic uncertainty related to these scale factors is estimated by setting these scale factors to $sf = 1$ and applying the total spin correlation extraction. The difference of the obtained f^{SM} for two sets of scale factors is assumed as the systematic uncertainty related to the lepton selection scale factors. In total, a systematic uncertainty of $\Delta f^{\text{SM}} = 0.01$ is observed.

Lepton energy scale: The lepton energy scale uncertainty is 0.3 % for electrons and negligible for muons. This is estimated from comparisons of data and Monte Carlo events by selecting Z boson events. In order to estimate the related uncertainty on f^{SM} , the energy of all electrons before selection is varied by 0.3 % and the whole analysis is repeated. An uncertainty of $\Delta f^{\text{SM}} = 0.01$ is estimated by this procedure.

Jet energy scale and resolution: The uncertainties related to the jet energy scale (JES) and the jet energy resolution (JER) are estimated in combination. The uncertainty related to the energy scale is estimated by varying the jets within their uncertainties of 5 %, see [102] and propagating the deviations to the estimated MET. A new set of templates with changed jet energies and MET is generated and the spin correlation extraction is repeated. The uncertainty related to jet energy resolution is estimated in a similar way. The transverse jet energy is varied by 5 to

10 %, depending on the η of the jet [102]. Since both uncertainties are correlated to each other a new set of templates is generated with jets changed according to both uncertainties and the template fit is repeated. The systematic uncertainty to JES and JER is estimated to be $\Delta f^{\text{SM}} = 0.02$

Background event yields: The uncertainties of background event yields or their normalization is considered by varying the event yields of Drell-Yan, fake lepton, diboson and single top-quark backgrounds by 100 %. The template fit is repeated with these new background templates and an uncertainty of $\Delta f^{\text{SM}} = 0.07$ is estimated.

Pile-up: For the estimated number of proton-proton interactions per bunch crossing in data an uncertainty of $\pm 5\%$ is assumed. This uncertainty is recommended by [128] and is considering the luminosity uncertainty of 2.2 % [76] during run period 2011 and the uncertainty of the inelastic proton cross section $\sigma_{\text{inel}} = 60.2 \pm 0.2$ (stat.) ± 1.1 (syst.) ± 2.4 (lum.) mb [129] at $\sqrt{s} = 7$ TeV. The observed number of proton-proton interactions of the selected data is shifted by the recommended $\pm 5\%$ and the pile-up event weights for Monte Carlo are recalculated. The whole analysis is repeated with these changed event weights and the larger deviation in f^{SM} considered as related systematic uncertainty. The uncertainty of $\Delta f^{\text{SM}} = 0.02$ is obtained.

b -tagging scale factor: The b -tagging scale factor is varied within its uncertainty and an uncertainty of $\Delta f^{\text{SM}} = 0.01$ is obtained as the largest deviation from the central value of f^{SM} .

The second group of systematic uncertainties related to physics modeling is always estimated by generating a new scenario and repeating the analysis. Afterwards, the new set of fit templates is used to extract the spin correlation strength from data.

Top quark mass: The systematic uncertainty related to the top-quark mass is considered by a set of top-quark pair samples with different simulated m_t values. These are generated using MC@NLO 3.1.4 and the top-quark masses of $m_t = 167.5, 170.0, 172.5, 175.0$ and 177.5 GeV. The sample with a top-quark mass of $m_t = 172.5$ GeV is considered as reference. For each mass point the template fit is performed and the dependency of f^{SM} as a function of the generated top-quark mass is determined. The measured deviation of f^{SM} for a change of $m_t = 172.5$ GeV for ± 2 GeV is considered as the related systematic uncertainty. A systematic uncertainty of $\Delta f^{\text{SM}} = 0.02$ is obtained.

PDF: The uncertainties of modeling the parton density functions of the colliding protons are considered according to the PDF4LHC prescription [130]. In general, different sets of PDFs are used with different central values and uncertainty bands. As an example of an uncertainty, the top-quark pair cross section uncertainty is estimated to be of the order of 5 % due to PDF uncertainties, see [131]. The deviation obtained by this procedure is $\Delta f^{\text{SM}} = 0.07$.

FastSim: Since the template fit uses two scenarios of top-quark processes, every systematic sample concerning top-quark modeling has to be generated according to these two scenarios. These samples are produced privately and use FastSim due to CPU constraints. The official production uses FullSim. Therefore, an uncertainty describing the two simulation strategies has to be taken into account. The measurement is repeated using privately generated MC@NLO FastSim samples compared to an official MC@NLO FullSim sample. The obtained difference of $\Delta f^{\text{SM}} = 0.06$ is taken as related uncertainty.

Renormalization and factorization scales: The uncertainties related to the used renormalization and factorization scales are estimated in combination. These scales are set in the simulation of the hard interaction. The default values for top pair generation is the top-quark mass: $f_{\text{ren}} = f_{\text{fac}} = m_t$. In total two sets of samples are generated by doubled and halved default values: $f_{\text{ren}} = f_{\text{fac}} = m_t/2$ and $f_{\text{ren}} = f_{\text{fac}} = 2 \cdot m_t$. The largest deviation in f^{SM} is denoted as systematic uncertainty. A systematic uncertainty of $\Delta f^{\text{SM}} = 0.15$ is estimated.

Top p_T : The modeling of the p_T distribution of top quarks show a slight but significant difference compared to data, see [112]. This deviation is corrected by reweighting the simulated top-quark events according to the measured p_T distribution before selection. After repeating the whole analysis an systematic error of $\Delta f^{\text{SM}} = 0.06$ is obtained.

Modeling of τ decay: The τ decay of the top-quark pair samples is modeled by the used hadronizer HERWIG. This hadronizer uses an outdated version of TAUOLA, which insufficiently models the polarization of the decaying tau leptons. A more detailed description of this issue is given in Section 8.1 and a systematic error of $\Delta f^{\text{SM}} = 0.03$ is estimated.

The dominant uncertainty is related to the modeling of $t\bar{t}$ processes. The recommended variation of the renormalization and factorization scale is the most dominant uncertainty with 20 %. The second dominating uncertainties are related to the integrated luminosity, the PDF uncertainties and the background events yields.

8.1 Tau Polarization Modeling

This section is dedicated to the systematic uncertainty of incorrectly modeled τ decays in MC@NLO samples. A short summary of the Standard Model expectation for τ polarizations and the corresponding observable in Monte-Carlo samples is given.

The Standard Model predicts left-handed τ leptons from W boson decays with a helicity $h_\tau = -1$ and a polarization of $P_\tau = -1$. This prediction is confirmed by the ATLAS experiment with a measurement of $P_\tau = -1.06 \pm 0.04$ (stat.) $^{+0.05}_{-0.07}$ (sys.) [132]. The τ helicity, h_τ , is accessible by the τ lepton decay products. The decay channel $\tau^- \rightarrow \pi^- \nu_\tau$ is most sensitive to the τ helicity states. Since this analysis investigates dileptonic $t\bar{t}$ decays, this section estimates the τ polarization with its leptonic decay channels.

Table 8.1: Uncertainties on the fraction of events with spin correlation Δf^{SM} , as predicted by the fit.

uncertainty Δf^{SM}	absolute	relative
statistic uncertainty	0.08	11 %
MC stat uncertainty	0.07	9 %
experimental		
lepton selection	0.01	1 %
lepton energy scale	0.01	1 %
JES/JER	0.02	3 %
all backgrounds	0.07	9 %
pile-up	0.02	3 %
b -tagging	0.01	1 %
$t\bar{t}$ modeling		
FastSim vs FullSim	0.06	8 %
Fact. and renorm. scales	0.15	20 %
τ pol	0.03	4 %
top mass	0.02	3 %
top p_{T}	0.06	8 %
PDF	0.07	9 %

The two body decay $W^- \rightarrow \tau^- \bar{\nu}_\tau$ produces τ leptons with an energy of half the W -mass in the W boson rest frame, $E_\tau = m_W/2$ if the τ mass is put to zero. The following three body decay $\tau^- \rightarrow l^- \bar{\nu}_l \nu_\tau$ produces leptons, $l = e, \mu$, with a continuous energy spectrum, E_{lep} . An observable testing the τ helicities is the ratio, x , of the lepton energy in the W boson rest frame, E_{lep} , divided by the τ energy in the same frame, E_τ :

$$x = \frac{E_{\text{lep}}}{E_\tau} = \frac{E_{\text{lep}}}{m_W/2} . \quad (8.1)$$

The Standard Model prediction of this energy ratio is:

$$\frac{d\Gamma}{dx} \sim \frac{5}{3} - 3x^2 + \frac{4}{3}x^3 - h_\tau \left(-\frac{1}{3} + 3x^2 - \frac{8}{3}x^3 \right) . \quad (8.2)$$

A more detailed discussion is given in [133, 134, 135]. A measurement of $\frac{d\Gamma}{dx}$ using generator level particles simulated by the MC@NLO generator and interfaced to the HERWIG hadronizer is used to extract the tau polarization. The results are shown in Figure 8.1 and reveal that that tau polarizations are neglected. The result of fitting the expected Standard Model distribution yields a tau helicity in agreement with zero, $h_\tau = (-7.4 \pm 9.0) \cdot 10^{-3}$. The first bin of the $\frac{d\Gamma}{dx}$ distribution is not considered during the fit, since it clearly shows mismodeling. A second $t\bar{t}$ sample is tested which is produced

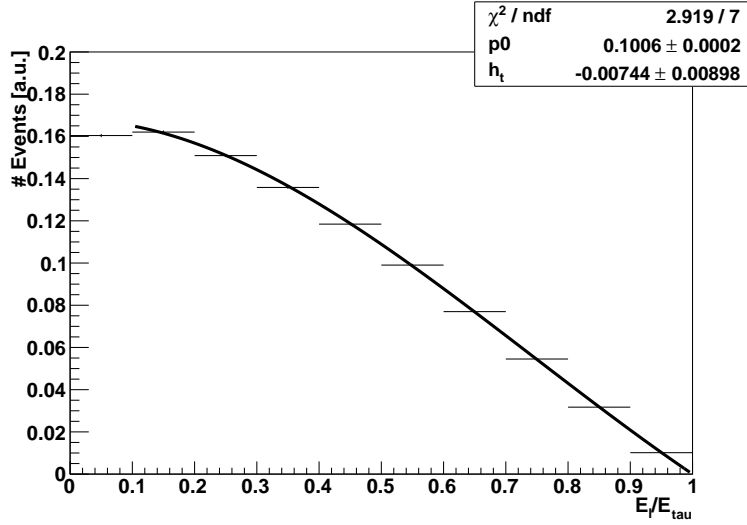


Figure 8.1: The ratio of the lepton energy and the τ energy in the rest frame of the W boson, using events generated by MC@NLO and interfaced to HERWIG. The tau polarization is extracted by fitting the function shown in Equation 8.2. The result of $h_\tau = (-7.4 \pm 9.0) \cdot 10^{-3}$ is in agreement with no polarization.

by POWHEG BOX interfaced to PYTHIA. This sample shows the expected distribution for the energy ratio, see Figure 8.2. The POWHEG BOX sample is close to the Standard

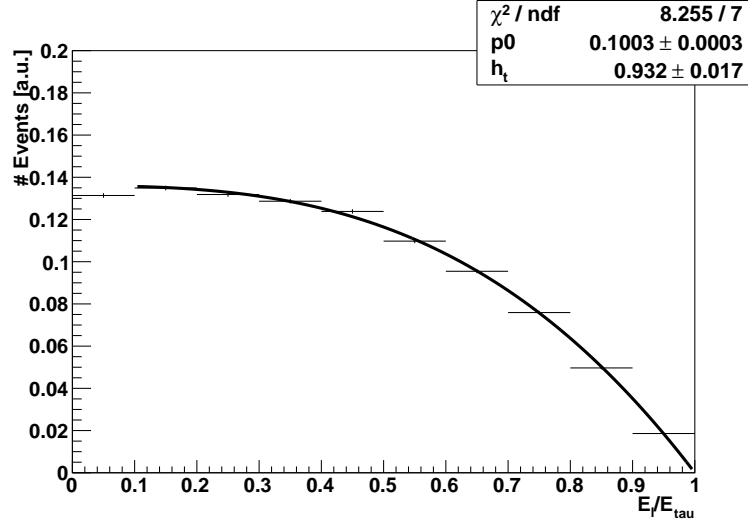


Figure 8.2: The ratio of the lepton energy and the τ energy in the rest frame of the W boson using events generated by POWHEG BOX and interfaced to PYTHIA. The tau polarization is extracted by fitting the function shown in Equation 8.2. The result of $h_\tau = -0.932 \pm 0.017$ is in reasonable agreement with the Standard Model expectation.

Model expectation of $h_\tau = -1$. The missing tau polarization in the MC@NLO sample is corrected by reweighting the events by Equation 8.2. The event weights are derived by comparison of the normalized expectation of the energy ratio, shown in Equation 8.2, and the obtained distribution presented in Figure 8.1. These event weights are used to obtain a reweighted $\Delta\phi$ distribution of selected dileptonic events with a correct τ polarization. The influence of reweighting on the $\Delta\phi$ distribution is shown for the three signal channels in Figure 8.3, 8.4 and 8.5. The reweighting yields only a small deviation of the $\Delta\phi$ distributions. A similar result is obtained using MC@NLO samples without spin correlations. The estimation of the systematic error due to incorrect modeling of tau polarization in the official MC@NLO samples is estimated by pseudo experiments. The reweighted $\Delta\phi$ distributions are used to generate pseudo experiments by varying the obtained templates within their bin-wise errors. These new templates are used to extract the Standard Model fraction f^{SM} . This procedure is repeated 10,000 times and the difference between the mean of the obtained f^{SM} distribution and the measured f_{SM} is considered as systematic uncertainty related to the mismodeled tau polarization. In total a systematic error of $\Delta f^{\text{SM}} = 0.034$ is obtained.

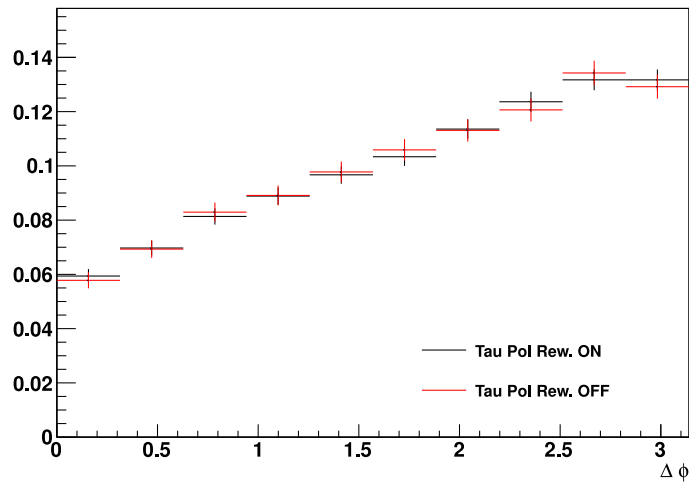


Figure 8.3: Selected $e\mu$ -channel events with spin correlations without τ polarization reweighting shown in red, with applied reweighting in black.

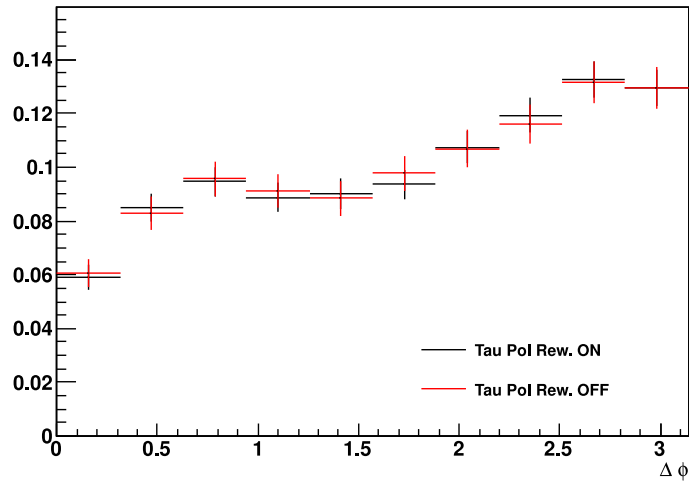


Figure 8.4: Selected $\mu\mu$ -channel events with spin correlations without τ polarization reweighting shown in red, with applied reweighting in black.

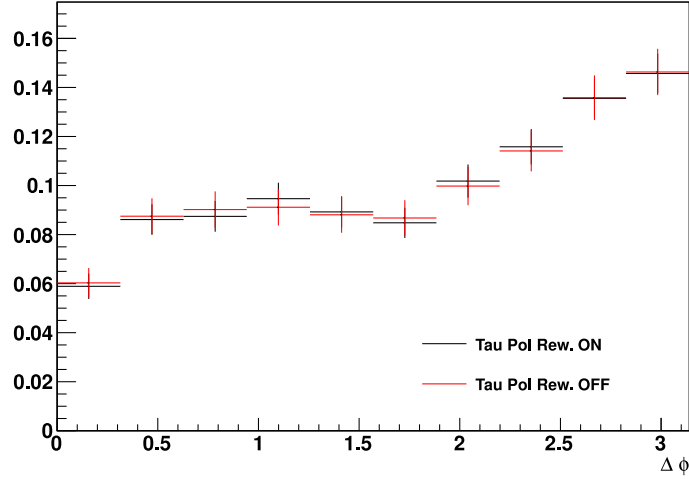


Figure 8.5: Selected ee -channel events with spin correlations without τ polarization reweighting shown in red, with applied reweighting in black.

8.2 Result of Systematic Uncertainties

The combined uncertainty related to sytematics, which are assumed to be uncorrelated, are obtained by a Gaussian sum of all systematic uncertainties listed in Table 8.1. Including all the systematic uncertainties the measurement of f^{SM} has following statistic and systematic uncertainties:

$$f^{\text{SM}} = 0.74 \pm 0.08 (\text{stat.}) \pm 0.21 (\text{sys.}) . \quad (8.3)$$

Since the used templates are assuming different helicity and spin correlation scenarios, the ratio of the two templates is linked to the top-quark spin correlation strength: The top-quark pair spin correlation n the helicity basis is related to the obtained ratio by following equation:

$$A_{\text{hel.}}^{\text{meas.}} = f^{\text{SM}} \cdot A_{\text{hel.}}^{\text{MC}} . \quad (8.4)$$

The intrinsic spin correlation of the sample simulated by MC@NLO is estimated using the double-differential angular distribution, see Equation 2.4, and is obtained to be $A_{\text{hel.}}^{\text{MC}} = 0.33$. This spin correlation strength is estimated in the helicity basis. Therefore, the measured spin correlation strength is also given in the helicity basis and all uncertainties are propagated according to this relation. The uncertainty of $A_{\text{hel.}}^{\text{MC}}$ is negligible related to the uncertainties of f^{SM} , because of the high statistics of the Monte Carlo samples. In total, a measured spin correlation strength of:

$$A_{\text{hel.}}^{\text{meas.}} = 0.24 \pm 0.03 (\text{stat.}) \pm 0.07 (\text{sys.}) \quad (8.5)$$

is obtained. Compared to the Standard Model expectation of $A_{\text{hel.}}^{\text{SM}} = 0.31 \pm 0.01$ [33], this value is in agreement within the given uncertainties. The uncertainty of the Standard Model expectation is estimated to be 0.01 due to approximations applied in the

theoretical calculation. The obtained result is also in agreement with the measurement $A_{\text{hel}}^{\text{ATLAS}} = 0.4 \pm 0.04 \text{ (stat.) } {}^{+0.08}_{-0.07} \text{ (sys.)}$ [26] by the ATLAS collaboration. Both measurements are in agreement with the Standard Model but are indicating different trends for A_{hel} , which has to be investigated in future analyses.

Chapter 9

Conclusion

The present analysis focuses on the measurement of the $t\bar{t}$ spin correlation strength in top quark pairs. This strategy offers a strong test of the Standard Model, since most BSM models are expected to lead to significantly different $t\bar{t}$ spin characteristics. In the scope of the outlined analysis a first measurement of the $t\bar{t}$ spin correlation in proton-proton collisions at $\sqrt{s} = 7$ TeV measured by the CMS collaboration has been performed and published [126, 127].

Beforehand, the matrix element generators MC@NLO and POWHEG BOX are validated and a reasonable agreement with the Standard Model expectation of top quark spin correlation strength is obtained. The simulated spin correlation strength of both Monte Carlo generators are $A_{\text{hel}}^{\text{MC@NLO}} = 0.33$ and $A_{\text{hel}}^{\text{POWHEG}} = 0.29$, while the Standard Model predicts an asymmetry of $A_{\text{hel}}^{\text{SM}} = 0.31$. The deviation is covered by approximations applied during the calculations.

Furthermore, a dedicated simulation strategy is developed in order to model top quark pair events with uncorrelated spins. This method is applied to generate the scenarios modeling systematic uncertainties. These scenarios are also acknowledged by the CMS collaboration and used in further publications. The uncorrelated scenario is assumed as null hypothesis to test the Standard Model expectation.

The analysis focuses on dileptonically decaying $t\bar{t}$ events with electrons and muons in their final states. A dedicated dileptonic top quark pair selection is implemented and optimized. The event yields are validated by comparison of data with Monte Carlo simulation. Additionally, the consistency of the selection is confirmed in terms of a cut-wise performance validation with similar independent CMS analyses by guaranteeing a synchronized cut-flow.

The event yields for background processes are obtained by both Monte Carlo simulations and data-driven methods. The matrix element method is implemented to estimate the

background contribution of QCD and W boson production from data. The Drell-Yan contamination is obtained from data with a Z boson mass ratio method. In order to correct for a non perfect modeling of trigger and lepton isolation efficiencies in Monte Carlo a set of alternative MET triggers is utilized to measure the according scale factors. The obtained results are in agreement with a reference selection established within the CMS collaboration.

The top pair spin correlation strength is measured by the difference of the azimuthal angle of the two reconstructed leptons, $\Delta\phi$. This avoids an additional bias and uncertainties due to the boosting into the top quark rest frames, which is required in alternative approaches. The $\Delta\phi$ distribution of selected events in data is analyzed by a template fit. The events are evaluated individually in the $\mu\mu$, $e\mu$ and ee channel. For each channel the $t\bar{t}$ signal is modeled with respect to the Standard Model and an uncorrelated scenario. The remaining background contributions are taken into account by an additional template. This set of three templates for each channel is combined into a global fit of the event yield per channel. The fraction of Standard Model scenario contribution f^{SM} is obtained as global quantification of the consistency with the Standard Model expectation. The obtained fraction resembles the measured spin correlation strength in top quark pair events. The final result is a spin correlation strength of $A_{\text{hel}}^{\text{meas.}} = 0.24 \pm 0.03 \text{ (stat.)} \pm 0.07 \text{ (sys.)}$ measured in the helicity basis.

The dominant systematic uncertainties related to the implemented selection and top quark simulation are studied. The following effects are investigated: lepton selection and energy resolution, jet energy and resolution, pile-up and b -tagging modeling and background normalization. Considering top quark simulation, additional effects are investigated: the renormalization and factorization scale, impact of incorrect tau polarization modeling, the assumed top quark mass, the used set of PDFs and the influence of using FastSim instead of the detailed detector simulation (FullSim), which requires more computing time. The estimation of uncertainties related to the top quark mass, the factorization scale and renormalization scale is done with private simulations of complementary signal samples with a full detector simulation. These private samples are validated against the official production sample and the deviations of using FastSim instead of FullSim are taken as the corresponding uncertainty. The influence of incorrect tau polarization modeling is investigated by event reweighting according to the Standard Model expectation. The most dominant systematic uncertainty turns out to be the choice of renormalization and factorization scales with an uncertainty of 20 %. PDF uncertainties and background normalizations are estimated to 9 %.

In total, the full dataset of 2011, corresponding to an integrated luminosity of 5.0 fb^{-1} , is investigated and a spin correlation strength of $A_{\text{hel}}^{\text{meas.}} = 0.24 \pm 0.03 \text{ (stat.)} \pm 0.07 \text{ (sys.)}$ is obtained. This is the first published measurement of top quark spin correlations at $\sqrt{s} = 7 \text{ TeV}$ by the CMS collaboration. The result is in agreement with the Standard Model expectation and with the measurement by the ATLAS collaboration. Neverthe-

less, while the CMS result indicates a measurement smaller than the Standard Model expectation, the ATLAS result shows a slight overestimation. This effect will be investigated in further studies and it remains fascinating how the slight tension will evolve.

Chapter 10

Outlook

The predominant systematic uncertainty is related to the used renormalization and factorization scales within MC@NLO. These uncertainties are not avoidable without a replacement of the core matrix element generator MC@NLO. Therefore, improvements concerning these uncertainties require an alternative official next-to leading order matrix element generator. Since no official sample with a modeling of no Standard Model top quark pair spin correlations are available for an energy of $\sqrt{s} = 7$ TeV a private production is required and an official validation is needed. Possible alternative matrix element generators are POWHEG and WHIZARD, whereas the later is not a standard generator used for official samples. By repeating the presented analysis with these generators a possible smaller systematic uncertainty considering renormalization and factorization could be estimated.

An analysis using $\sqrt{s} = 8$ TeV dataset with higher statistics will not significantly improve the result, because it is systematically dominated. Furthermore, the spin correlation strength changes within the uncertainties, because of the only slightly alternating ratio of gluon-gluon fusion and quark-antiquark annihilation production. The statistics of the 2011 dataset could also be extended by considering dileptonic top quark pair events with tau leptons in their final states. Due to decay combinatorics, the number of signal events would increase by a quarter of the total event yield. The second important systematic uncertainties are related to PDF and background estimations. The PDF uncertainties are only reducible with more precise measurements of the proton PDFs and a reprocessing of all investigated samples.

The uncertainty of background estimation could be reduced by a more detailed study of the background contributions. Furthermore, data-driven background estimations, especially, the background template shape of single top and Drell-Yan processes would avoid the very conservative scaling of 100 % of the background event yields.

An additional application of unfolding would simplify the comparison of the obtained $\Delta\phi$ distribution with theory predictions. Furthermore, this unfolded distribution could yield on a possible anomalous chromomagnetic dipole moment of the top quark, see [34]. By implementing a full kinematic reconstruction of the top quark pair system additional spin correlation observables would be accessible. The double differential distribution of

$\cos \theta_{1,2}$, see Equation 2.4, is able to measure the asymmetry A_{hel} directly. Therefore, no additional no-spin correlation samples would be necessary and this measurement would be more robust by avoiding the corresponding simulation uncertainties. With the complete kinematic reconstruction, a cut on the invariant mass of the top quark the difference between the Standard Model spin correlation and a scenario of uncorrelated spins could be enhanced.

With the start of the $\sqrt{s} = 13 \text{ TeV}$ era the higher energy range provides more potential for beyond Standard Model scenarios which could manifest in spin correlation observables. The new era of LHC physics will remain intriguing for spin correlation investigations.

Appendix A

Samples and Datasets

Table A.1: Investigated primary datasets. The datasets are divided according to different trigger streams.

dataset description	dataset name
Run2011A Muon 05Aug ReReco	DoubleMu/Run2011A-05Aug2011-v1
Run2011A Muon May10 ReReco	DoubleMu/Run2011A-May10ReReco-v1
Run2011A Muon Prompt Reco v4	DoubleMu/Run2011A-PromptReco-v4
Run2011A Muon Prompt Reco v6	DoubleMu/Run2011A-PromptReco-v6
Run2011B Muon Prompt Reco v1	DoubleMu/Run2011B-PromptReco-v1
Run2011A Electron 05Aug ReReco	DoubleElectron/Run2011A-05Aug2011-v1
Run2011A Electron May10 ReReco	DoubleElectron/Run2011A-May10ReReco-v1
Run2011A Electron Prompt Reco v4	DoubleElectron/Run2011A-PromptReco-v4
Run2011A Electron Prompt Reco v6	DoubleElectron/Run2011A-PromptReco-v6
Run2011B Electron Prompt Reco v1	DoubleElectron/Run2011B-PromptReco-v1
Run2011A Muon-Electron 05Aug ReReco	MuEG/Run2011A-05Aug2011-v1
Run2011A Muon-Electron May10 ReReco	MuEG/Run2011A-May10ReReco-v1
Run2011A Muon-Electron Prompt Reco v4	MuEG/Run2011A-PromptReco-v4
Run2011A Muon-Electron Prompt Reco v6	MuEG/Run2011A-PromptReco-v6
Run2011B Muon-Electron Prompt Reco v1	MuEG/Run2011B-PromptReco-v1
Run2011A MET 05Aug ReReco	MET/Run2011A-05Aug2011-v1
Run2011A METBTag May10 ReReco	METBTag/Run2011A-May10ReReco-v1
Run2011A MET Prompt Reco v4	MET/Run2011A-PromptReco-v4
Run2011A MET Prompt Reco v6	MET/Run2011A-PromptReco-v6

Table A.2: Summary of JSON files applied to the recorded data. The corresponding luminosities per JSON file are also shown. The JSON files are obtained from [136] and the luminosity is calculated using the official prescription.

datasets	JSON file	luminosity
2011A May10	Cert_160404-163869-7TeV_May10ReReco_Collisions11_JSON_v3.txt	216.20 pb ⁻¹
2011A 05Aug	Cert_170249-172619-7TeV_ReReco5Aug_Collisions11_JSON_v3.txt	368.04 pb ⁻¹
2011A PromptReco v4	Cert_160404-173692-7TeV_PromptReco_Collisions11_JSON.txt	929.75 pb ⁻¹
2011A PromptReco v6	Cert_160404-173692-7TeV_PromptReco_Collisions11_JSON.txt	658.89 pb ⁻¹
2011A PromptReco v6	Cert_160404-173692-7TeV_PromptReco_Collisions11_JSON.txt	658.89 pb ⁻¹
2011B PromptReco v1	Cert_160404-180252-7TeV_PromptReco_Collisions11_JSON.txt	2.714 fb ⁻¹

Table A.3: Official samples used for background process description. Technical information taken from [137]. Cross sections are calculated by FEWZ [138] and MCFM [139].

dataset name	ME generator	number of events	σ [pb]	\mathcal{L}_{int} [fb $^{-1}$]
/DYJetsToLL_M-10To50_TuneZ2_7TeV-madgraph/Fall11-PU_S6_START42_V14B-v1/AODSIM	MadGraph 4	31,480,628	12,783,000	2.463
/DYJetsToLL_TuneZ2_M-50_7TeV-madgraph-tauola/Fall11-PU_S6_START42_V14B-v1/AODSIM	MadGraph 4	36,209,629	3,048,000	11.880
/Tbar_TuneZ2_s-channel_7TeV-powheg-tauola/Fall11-PU_S6_START42_V14B-v1/AODSIM	POWHEG BOX 1.4	137,980	1.490	92.604
/Tbar_TuneZ2_t-channel_7TeV-powheg-tauola/Fall11-PU_S6_START42_V14B-v1/AODSIM	POWHEG BOX 1.4	1,944,826	22,000	88.401
/Tbar_TuneZ2_tW-channel-DR_7TeV-powheg-tauola/Fall11-PU_S6_START42_V14B-v1/AODSIM	POWHEG BOX 1.4	323,401	7.870	41.093
/Tbar_TuneZ2_tW-channel-DS_7TeV-powheg-tauola/Fall11-PU_S6_START42_V14B-v1/AODSIM	POWHEG BOX 1.4	785,246	7.870	99.777
/T_TuneZ2_s-channel_7TeV-powheg-tauola/Fall11-PU_S6_START42_V14B-v1/AODSIM	POWHEG BOX 1.4	259,971	2.720	95.578
/T_TuneZ2_t-channel_7TeV-powheg-tauola/Fall11-PU_S6_START42_V14B-v1/AODSIM	POWHEG BOX 1.4	3,900,171	42,600	91.553
/T_TuneZ2_tW-channel-DR_7TeV-powheg-tauola/Fall11-PU_S6_START42_V14B-v1/AODSIM	POWHEG BOX 1.4	814,390	7.870	103.480
/T_TuneZ2_tW-channel-DS_7TeV-powheg-tauola/Fall11-PU_S6_START42_V14B-v1/AODSIM	POWHEG BOX 1.4	795,379	7.870	101.065
/QCD_Pt-20_MuEnrichedPt-15_TuneZ2_7TeV-pythia6/Fall11-PU_S6_START42_V14B-v1/AODSIM	PYTHIA 6.4.24	25,080,241	84,679,000	0.296
/WJetsToLNu_TuneZ2_7TeV-madgraph-tauola/Fall11-PU_S6_START42_V14B-v1/AODSIM	MadGraph 4	81,345,381	31,314,000	2.598
/WW_TuneZ2_7TeV_pythia6_tauola/Fall11-PU_S6_START42_V14B-v1/AODSIM	PYTHIA 6.4.24	4,225,916	47,000	89.837
/WZ_TuneZ2_7TeV_pythia6_tauola/Fall11-PU_S6_START42_V14B-v1/AODSIM	PYTHIA 6.4.24	4,265,243	18,200	234.354
/ZZ_TuneZ2_7TeV_pythia6_tauola/Fall11-PU_S6_START42_V14B-v1/AODSIM	PYTHIA 6.4.24	4,191,045	7.670	546.420

Table A.4: Official samples used for top quark pair modeling. The signal process is extracted by a Monte Carlo truth filter selecting only events which decay dileptonically. Technical information taken from [137].

dataset name	ME generator	number of events	σ [pb]	\mathcal{L}_{int} [fb ⁻¹]
/TT_noCorr_7TeV-mcatnlo/Fall11-PU_S6.START42_V14B-v1/AODSIM	MC@NLO 3.4.1	12,034,490	161.9	74.3
/TT_TuneZ2_7TeV-mcatnlo/Fall11-PU_S6.START42_V14B-v1/AODSIM	MC@NLO 3.4.1	21,745,199	161.9	134.3

Table A.5: Triggers used for data selecting.

trigger name	trigger run range R
di-electron triggers	
HLT_Ele17_CaloIdL_CaloIsoVL_Ele8_CaloIdL_CaloIsoVL_v*	$R \leq 170901$
HLT_Ele17_CaloIdT_CaloIsoVL_TkIdVL_TkIsoVL_Ele8_CaloIdT_CaloIsoVL_TkIdVL_TkIsoVL_v*	$R \geq 170902$
di-muon triggers	
HLT_DoubleMu7_v*	$R \leq 165208$
HLT_Mu13_Mu8_v*	$165209 \leq R \leq 178419$
HLT_Mu17_Mu8_v* OR HLT_Mu17_TkMu8_v*	$R \leq 178420$
electron-muon triggers	
HLT_Mu8_Ele17_CaloIdL_v*	$R \leq 167913$
HLT_Mu8_Ele17_CaloIdT_CaloIsoVL_v*	$R \geq 167914$
HLT_Mu17_Ele8_CaloIdL_v*	$R \leq 175972$
HLT_Mu17_Ele8_CaloIdT_CaloIsoVL_v*	$R \geq 175973$

Table A.6: Triggers used for Monte Carlo events.

trigger name
di-electron trigger
HLT_Ele17_CaloIdL_CaloIsoVL_Ele8_CaloIdL_CaloIsoVL_v2
di-muon trigger
HLT_DoubleMu6_v1
electron-muon triggers
HLT_Mu8_Ele17_CaloIdL_v2 OR HLT_Mu10_Ele10_CaloIdL_v3

Bibliography

- [1] M. Gell-Mann and Y. Ne'Eman. *The Eightfold Way*. Advanced book classics. Perseus Pub., 2000. ISBN: 9780738202990.
- [2] S. Weinberg. “A Model of Leptons”. *Phys. Rev. Lett.* 19.21 (1967), pp. 1264–1266. DOI: 10.1103/PhysRevLett.19.1264.
- [3] M. Breidenbach et al. “Observed Behavior of Highly Inelastic Electron-Proton Scattering”. *Phys. Rev. Lett.* 23 (16 1969), pp. 935–939. DOI: 10.1103/PhysRevLett.23.935.
- [4] E. D. Bloom et al. “High-Energy Inelastic e-p Scattering at 6 and 10”. *Phys. Rev. Lett.* 23 (16 1969), pp. 930–934. DOI: 10.1103/PhysRevLett.23.930.
- [5] UA1 Collaboration. “Experimental Observation of Isolated Large Transverse Energy Electrons with Associated Missing Energy at $\sqrt{s} = 540$ GeV”. *Phys.Lett.* B122 (1983), pp. 103–116. DOI: 10.1016/0370-2693(83)91177-2.
- [6] UA1 Collaboration. “Experimental Observation of Lepton Pairs of Invariant Mass Around 95 GeV/ c^2 at the CERN SPS Collider”. *Phys.Lett.* B126 (1983), pp. 398–410. DOI: 10.1016/0370-2693(83)90188-0.
- [7] UA2 Collaboration. “Observation of Single Isolated Electrons of High Transverse Momentum in Events with Missing Transverse Energy at the CERN $\bar{p}p$ Collider”. *Phys.Lett.* B122 (1983), pp. 476–485. DOI: 10.1016/0370-2693(83)91605-2.
- [8] UA2 Collaboration. “Evidence for $Z^0 \rightarrow e^+e^-$ at the CERN $\bar{p}p$ Collider”. *Phys.Lett.* B129 (1983), pp. 130–140. DOI: 10.1016/0370-2693(83)90744-X.
- [9] M. Gell-Mann. “The Interpretation of the New Particles as Displaced Charge Multiplets”. *Il Nuovo Cimento (1955-1965)* 4.0 (1956), pp. 848–866. DOI: 10.1007/BF02748000.
- [10] P. W. Higgs. “Broken symmetries, massless particlees and gauge fields”. *Physics Letters* 12 (Sept. 1964), pp. 132–133. DOI: 10.1016/0031-9163(64)91136-9.
- [11] F. Englert and R. Brout. “Broken Symmetry and the Mass of Gauge Vector Mesons”. *Phys. Rev. Lett.* 13 (9 1964), pp. 321–323. DOI: 10.1103/PhysRevLett.13.321.
- [12] G. S. Guralnik, C. R. Hagen, and T. W. B. Kibble. “Global Conservation Laws and Massless Particles”. *Phys. Rev. Lett.* 13 (20 1964), pp. 585–587. DOI: 10.1103/PhysRevLett.13.585.

- [13] The CMS Collaboration. “Observation of a new boson at a mass of 125 GeV with the CMS experiment at the LHC”. *Physics Letters B* 716 (Sept. 2012), pp. 30–61. DOI: 10.1016/j.physletb.2012.08.021.
- [14] The ATLAS Collaboration. “Observation of a new particle in the search for the Standard Model Higgs boson with the ATLAS detector at the LHC”. *Physics Letters B* 716 (Sept. 2012), pp. 1–29. DOI: 10.1016/j.physletb.2012.08.020.
- [15] ATLAS Collaboration, CDF Collaboration, CMS Collaboration, D0 Collaboration. *First combination of Tevatron and LHC measurements of the top-quark mass*. Tech. rep. ATLAS-CONF-2014-008, CDF-NOTE-11071, CMS-PAS-TOP-13-014, D0-NOTE-6416. <http://cds.cern.ch/record/1669819>. Geneva: CERN, 2014.
- [16] J. Beringer et al. “Review of Particle Physics (RPP)”. *Phys.Rev.* D86 (2012), p. 010001. DOI: 10.1103/PhysRevD.86.010001.
- [17] A. Quadt. “Top quark physics at hadron colliders”. English. *The European Physical Journal C - Particles and Fields* 48.3 (2006), pp. 835–1000. DOI: 10.1140/epjc/s2006-02631-6.
- [18] Michelangelo L Mangano and Guido Altarelli. *Proceedings of the Workshop on Standard Model Physics (and more) at the LHC*. Geneva: CERN, 2000. DOI: 10.5170/CERN-2000-004.
- [19] The Durham HEP Databases. *Online Plotting and Calculation, Parton Distribution Function Server*. <http://hepdata.cedar.ac.uk/pdf/pdf3.html>. Accessed 27th January 2014.
- [20] The CMS Collaboration. “CMS Electroweak Public Physics Results” (). <https://twiki.cern.ch/twiki/bin/view/CMSPublic/PhysicsResultsEWK>.
- [21] Gregory Mahlon and Stephen Parke. “Angular correlations in top quark pair production and decay at hadron colliders”. *Phys. Rev. D* 53 (9 1996), pp. 4886–4896. DOI: 10.1103/PhysRevD.53.4886.
- [22] The CMS Collaboration. “Measurement of the $t\bar{t}$ production cross section in the dilepton channel in pp collisions at $\sqrt{s} = 7$ TeV”. English. *Journal of High Energy Physics* 2012.11, 67 (2012). DOI: 10.1007/JHEP11(2012)067.
- [23] CMS Collaboration. “Measurement of the $t\bar{t}$ production cross section and the top quark mass in the dilepton channel in pp collisions at $\sqrt{s} = 7$ TeV”. *Journal of High Energy Physics* 7, 49 (July 2011), p. 49. DOI: 10.1007/JHEP07(2011)049.
- [24] R. Schwienhorst on behalf of the ATLAS, CMS, CDF and D0 Collaborations. “Top Cross-Sections and Single Top”. *Int. Journal of Modern Physics Conf. Series* 31, 1460277 (May 2014), p. 60277. DOI: 10.1142/S2010194514602774.
- [25] Werner Bernreuther and Zong-Guo Si. “Top quark spin correlations and polarization at the LHC: Standard model predictions and effects of anomalous top chromo moments”. *Physics Letters B* 725.1-3 (2013), pp. 115–122. ISSN: 0370-2693. DOI: 10.1016/j.physletb.2013.06.051.

- [26] The ATLAS Collaboration. “Observation of Spin Correlation in $t\bar{t}$ Events from pp Collisions at $\sqrt{s} = 7$ TeV Using the ATLAS Detector”. *Physical Review Letters* 108.21, 212001 (May 2012), p. 212001. DOI: 10.1103/PhysRevLett.108.212001.
- [27] D0 Collaboration. “Measurement of spin correlation in $t\bar{t}$ production using dilepton final states”. *Physics Letters B* 702 (Aug. 2011), pp. 16–23. DOI: 10.1016/j.physletb.2011.05.077.
- [28] CDF Collaboration. “Measurement of $t\bar{t}$ spin correlation in $p\bar{p}$ collisions using the CDF II detector at the Tevatron”. *Phys. Rev. D* 83.3, 031104 (Feb. 2011), p. 031104. DOI: 10.1103/PhysRevD.83.031104.
- [29] W. Bernreuther et al. “Spin properties of top quark pairs produced at hadron colliders”. *Acta Phys.Polon.* B34 (2003). <http://inspirehep.net/record/617628>, pp. 4477–4490. arXiv: hep-ph/0304244 [hep-ph].
- [30] L. Sonnenschein. “The $t\bar{t}$ production in pp collisions at $\sqrt{s} = 14$ TeV”. Phd thesis. RWTH Aachen, 2001.
- [31] Stefano Frixione and Bryan R. Webber. “Matching NLO QCD computations and parton shower simulations”. *Journal of High Energy Physics* 0206 (2002), p. 029. DOI: 10.1088/1126-6708/2002/06/029.
- [32] S. Frixione, P. Nason, and B. R. Webber. “Matching NLO QCD and parton showers in heavy flavour production”. *Journal of High Energy Physics* 8, 007 (Aug. 2003), p. 7. DOI: 10.1088/1126-6708/2003/08/007.
- [33] Werner Bernreuther and Zong-Guo Si. “Distributions and correlations for top quark pair production and decay at the Tevatron and LHC.” *Nucl.Phys.* B837 (2010), pp. 90–121. DOI: 10.1016/j.nuclphysb.2010.05.001.
- [34] Werner Bernreuther and Zong-Guo Si. “Top quark spin correlations and polarization at the LHC: standard model predictions and effects of anomalous top chromo moments”. *Phys.Lett.* B725.1-3 (2013), pp. 115–122. DOI: 10.1016/j.physletb.2013.06.051.
- [35] Z. Han et al. “(Light) stop signs”. *Journal of High Energy Physics* 8, 83 (Aug. 2012), p. 83. DOI: 10.1007/JHEP08(2012)083.
- [36] W. Bernreuther, M. Flesch, and P. Haberl. “Signatures of Higgs bosons in the top quark decay channel at hadron colliders”. *Phys. Rev. D* 58 (11 1998), p. 114031. DOI: 10.1103/PhysRevD.58.114031.
- [37] Brüning, Oliver and others. *LHC Design Report Vol. I The LHC Main Ring*. LHC Design Report CERN-2004-003-V-1. Geneva: CERN, 2004. DOI: 10.5170/CERN-2004-003-V-1.
- [38] Lyndon Evans and Philip Bryant. “LHC Machine”. *Journal of Instrumentation* 3.08 (2008), S08001. DOI: 10.1088/1748-0221/3/08/S08001.
- [39] G L Bayatian et al. *CMS Physics: Technical Design Report Volume 1: Detector Performance and Software*. Technical Design Report CMS. <http://cds.cern.ch/record/922757>. Geneva: CERN, 2006.

- [40] The LEP Injector Study Group. “LEP Design Report: Vol. 1. The LEP Injector Chain” (1983). <http://cds.cern.ch/record/98881>.
- [41] European Organization for Nuclear Research. *LEP Design Report: Vol. 2. The LEP Main Ring*. <http://cds.cern.ch/record/102083>. Geneva: CERN, 1984.
- [42] The ATLAS Collaboration. *ATLAS detector and physics performance: Technical Design Report, 1*. Technical Design Report ATLAS. <http://cds.cern.ch/record/391176>. Geneva: CERN, 1999.
- [43] The ALICE Collaboration. *ALICE: Technical proposal for a Large Ion collider Experiment at the CERN LHC*. LHC Tech. Proposal. <http://cds.cern.ch/record/293391>. Geneva: CERN, 1995.
- [44] LHCb Collaboration. *LHCb : Technical Proposal*. Tech. Proposal. <http://cds.cern.ch/record/622031>, <http://lhcb.web.cern.ch/lhcb/TDR/TDR.htm>. Geneva: CERN, 1998.
- [45] O Adriani et al. *LHCf experiment: Technical Design Report*. Technical Design Report LHCf. <http://cdsweb.cern.ch/record/926196>. Geneva: CERN, 2006.
- [46] The TOTEM Collaboration. *Total cross-section, elastic scattering and diffraction dissociation at the Large Hadron Collider at CERN: TOTEM Technical Design Report*. Technical Design Report TOTEM CERN-LHCC-2004-002, TOTEM-TDR-001. <http://cdsweb.cern.ch/record/704349>. Geneva: CERN, 2004.
- [47] The CMS Collaboration. “Public CMS Luminosity Information”. *2011 Proton-Proton Collisions* (Accessed 17th September 2014). <https://twiki.cern.ch/twiki/bin/view/CMSPublic/LumiPublicResults>, picture: http://cms-service-lumi.web.cern.ch/cms-service-lumi/publicplots/int_lumi_per_day_cumulative_pp_2011.pdf.
- [48] Tevatron I Group. *Design Report Tevatron 1 project*. Tech. rep. FERMILAB-DESIGN-1984-01. <http://cds.cern.ch/record/1478620>. Batavia, Illinois: Fermi National Accelerator Laboratory, 1984.
- [49] C. Vellidis. “New Results from Tevatron”. *Proceedings of Science DIS2013* (2013), p. 009.
- [50] Serge Dailier. *Map of the Geneva region and of the LHC*. <http://cds.cern.ch/record/842399>. 1997.
- [51] Felix Höhle. “Untersuchung von Spinkorrelationen im semileptonischen Top-Paar-Zerfall mit dem CMS-Experiment”. <http://cds.cern.ch/record/1361036>. Diploma Thesis. RWTH Aachen, 2010.
- [52] Oliver Brüning et al. *LHC Design Report Vol.II The LHC Infrastructure and General Services*. LHC Design Report CERN-2004-003-V-2. Geneva: CERN, 2004. DOI: 10.5170/CERN-2004-003-V-2.
- [53] Michael Benedikt et al. *LHC Design Report Vol.III The LHC Injector Chain*. LHC Design Report CERN-2004-003-V-3. Geneva: CERN, 2004. DOI: 10.5170/CERN-2004-003-V-3.

- [54] Klaus Wille. *Physik der Teilchenbeschleuniger und Synchrotronstrahlungsquellen: eine Einführung*. Teubner Studienbücher Physik. Stuttgart: Teubner, 1992. ISBN: 978-3519030874.
- [55] The CMS Collaboration. “The CMS experiment at the CERN LHC”. *Journal of Instrumentation* 3.08 (2008), S08004–S08004. DOI: 10.1088/1748-0221/3/08/S08004.
- [56] V Karimki et al. *The CMS tracker system project: Technical Design Report*. Technical Design Report CMS. <http://cds.cern.ch/record/368412>. Geneva: CERN, 1997.
- [57] W. Adam et al. “The effect of highly ionising particles on the CMS silicon strip tracker”. *Nuclear Instruments and Methods in Physics Research Section A: Accelerators, Spectrometers, Detectors and Associated Equipment* 543.23 (2005), pp. 463–482. DOI: 10.1016/j.nima.2004.11.049.
- [58] Benedikt Christopher Hegner. “Studies on Spin-Spin-Correlations in dileptonic top pair-events at LHC”. eng. <http://ediss.sub.uni-hamburg.de/volltexte/2009/4011>. Phd thesis. Von-Melle-Park 3, 20146 Hamburg: Universität Hamburg, 2008.
- [59] The CMS Collaboration. “Description and performance of track and primary-vertex reconstruction with the CMS tracker”. *Journal of Instrumentation* 9.10 (2014), P10009. DOI: 10.1088/1748-0221/9/10/P10009.
- [60] The CMS Collaboration. “CMS tracking performance results from early LHC operation”. *European Physical Journal C* 70 (Dec. 2010), pp. 1165–1192. DOI: 10.1140/epjc/s10052-010-1491-3.
- [61] CMS Collaboration. *The CMS electromagnetic calorimeter project: Technical Design Report*. Technical Design Report CMS. <http://cds.cern.ch/record/349375>. Geneva: CERN, 1997.
- [62] CMS Collaboration. *The CMS hadron calorimeter project: Technical Design Report*. Technical Design Report CMS. <http://cds.cern.ch/record/357153>. Geneva: CERN, 1997.
- [63] CMS Collaboration. “Performance and operation of the CMS electromagnetic calorimeter”. *Journal of Instrumentation* 5.03 (2010), T03010. DOI: 10.1088/1748-0221/5/03/T03010.
- [64] M. Giffels. “Study of the Sensitivity of CMS to the Lepton Flavour Violating Neutrinoless τ Decay $\tau \rightarrow \mu\mu\mu$ ”. <http://cds.cern.ch/record/1292236>. Doktorarbeit. RWTH Aachen, 2009, p. 110.
- [65] The CMS Collaboration. “Energy calibration and resolution of the CMS electromagnetic calorimeter in pp collisions at $\sqrt{s} = 7$ TeV”. *Journal of Instrumentation* 8.09 (2013), P09009. DOI: 10.1088/1748-0221/8/09/P09009.

- [66] D. Froidevaux and P. Sphicas. “General-purpose detectors for the Large Hadron Collider”. *Ann.Rev.Nucl.Part.Sci.* 56 (2006), pp. 375–440. DOI: 10.1146/annurev.nucl.54.070103.181209.
- [67] CMS Collaboration. “Commissioning of the CMS Experiment and the Cosmic Run at Four Tesla”. *JINST* 5 (2010), T03001. DOI: 10.1088/1748-0221/5/03/T03001.
- [68] CMS Collaboration. “Performance of the CMS Hadron Calorimeter with Cosmic Ray Muons and LHC Beam Data”. *JINST* 5 (2010), T03012. DOI: 10.1088/1748-0221/5/03/T03012.
- [69] The CMS Collaboration. “The performance of the CMS muon detector in proton-proton collisions at $\sqrt{s} = 7$ TeV at the LHC”. *Journal of Instrumentation* 8, P11002 (Nov. 2013), 1002P. DOI: 10.1088/1748-0221/8/11/P11002.
- [70] CMS Collaboration. “Performance of the CMS drift tube chambers with cosmic rays”. *Journal of Instrumentation* 5 (Mar. 2010), p. 3015. DOI: 10.1088/1748-0221/5/03/T03015.
- [71] Sergio Cittolin, Attila Rcz, and Paris Sphicas. *CMS The TriDAS Project: Technical Design Report, Volume 2: Data Acquisition and High-Level Trigger. CMS trigger and data-acquisition project.* Technical Design Report CMS. <http://cdsweb.cern.ch/record/578006>. Geneva: CERN, 2002.
- [72] The CMS Collaboration. “The CMS high level trigger”. English. *The European Physical Journal C - Particles and Fields* 46.3 (2006), pp. 605–667. ISSN: 1434-6044. DOI: 10.1140/epjc/s2006-02495-8.
- [73] CMS Collaboration. “Performance of the CMS Level-1 Trigger during Commissioning with Cosmic Ray Muons”. *JINST* 5 (2010), T03002. DOI: 10.1088/1748-0221/5/03/T03002.
- [74] CMS Collaboration. “Commissioning of the CMS High-Level Trigger with Cosmic Rays”. *JINST* 5 (2010), T03005. DOI: 10.1088/1748-0221/5/03/T03005.
- [75] CMS Collaboration. *Measurement of CMS Luminosity.* Tech. rep. CMS-PAS-EWK-10-004. <http://cds.cern.ch/record/1279145>. Geneva: CERN, 2010.
- [76] CMS Collaboration. *Absolute Calibration of the Luminosity Measurement at CMS: Winter 2012 Update.* Tech. rep. CMS-PAS-SMP-12-008. <http://cds.cern.ch/record/1434360>. Geneva: CERN, 2012.
- [77] Nicholas Metropolis and Stanislaw Ulam. “The monte carlo method”. *Journal of the American statistical association* 44.247 (1949), pp. 335–341. DOI: 10.2307/2280232.
- [78] Stefano Frixione, Paolo Nason, and Giovanni Ridolfi. “A Positive-weight next-to-leading-order Monte Carlo for heavy flavour hadroproduction”. *Journal of High Energy Physics* 0709 (2007), p. 126. DOI: 10.1088/1126-6708/2007/09/126.

- [79] Stefano Frixione, Paolo Nason, and Carlo Oleari. “Matching NLO QCD computations with Parton Shower simulations: the POWHEG method”. *JHEP* 0711 (2007), p. 070. DOI: 10.1088/1126-6708/2007/11/070.
- [80] Simone Alioli et al. “A general framework for implementing NLO calculations in shower Monte Carlo programs: the POWHEG BOX”. English. *Journal of High Energy Physics* 2010.6, 43 (2010). DOI: 10.1007/JHEP06(2010)043.
- [81] Paolo Nason. “A New method for combining NLO QCD with shower Monte Carlo algorithms”. *JHEP* 0411 (2004), p. 040. DOI: 10.1088/1126-6708/2004/11/040.
- [82] T. Sjöstrand et al. “PYTHIA 6.4 Physics and Manual”. *Journal of High Energy Physics* 2006.05 (2006), p. 026. DOI: 10.1088/1126-6708/2006/05/026.
- [83] Johan Alwall et al. “MadGraph 5 : Going Beyond”. *JHEP* 1106 (2011), p. 128. DOI: 10.1007/JHEP06(2011)128.
- [84] Johan Alwall et al. “MadGraph/MadEvent v4: The New Web Generation”. *JHEP* 0709 (2007), p. 028. DOI: 10.1088/1126-6708/2007/09/028.
- [85] Johan Alwall et al. “A Standard format for Les Houches event files”. *Comput. Phys. Commun.* 176 (2007), pp. 300–304. DOI: 10.1016/j.cpc.2006.11.010.
- [86] S. Jadach et al. “The tau decay library TAUOLA: Version 2.4”. *Comput. Phys. Commun.* 76 (1993), pp. 361–380. DOI: 10.1016/0010-4655(93)90061-G.
- [87] Elisabetta Barberio and Zbigniew Was. “PHOTOS: A Universal Monte Carlo for QED radiative corrections. Version 2.0”. *Comput. Phys. Commun.* 79 (1994), pp. 291–308. DOI: 10.1016/0010-4655(94)90074-4.
- [88] The GEANT4 Collaboration. “GEANT4 - a Simulation Toolkit”. *Nuclear Instruments and Methods in Physics Research Section A: Accelerators, Spectrometers, Detectors and Associated Equipment* 506.3 (2003), pp. 250–303. DOI: 10.1016/S0168-9002(03)01368-8.
- [89] The Geant4 Collaboration. “Geant4 developments and applications”. *Nuclear Science, IEEE Transactions on* 53.1 (2006), pp. 270–278. DOI: 10.1109/TNS.2006.869826.
- [90] G. Corcella et al. “HERWIG 6: an event generator for hadron emission reactions with interfering gluons (including supersymmetric processes)”. *Journal of High Energy Physics* 1, 010 (Jan. 2001), p. 10. DOI: 10.1088/1126-6708/2001/01/010.
- [91] Rahmat Rahmat, Rob Kroeger, and Andrea Giammanco. “The Fast Simulation of The CMS Experiment”. *Journal of Physics: Conference Series* 396.6 (2012), p. 062016. DOI: 10.1088/1742-6596/396/6/062016.
- [92] The CMS Collaboration. “Performance of CMS muon reconstruction in pp collision events at $\sqrt{s} = 7$ TeV”. *Journal of Instrumentation* 7.10 (2012), P10002. DOI: 10.1088/1748-0221/7/10/P10002.
- [93] The CMS Collaboration. “Performance of CMS muon reconstruction in cosmic-ray events”. *Journal of Instrumentation* 5 (Mar. 2010), p. 3022. DOI: 10.1088/1748-0221/5/03/T03022.

- [94] R. Frühwirth. “Application of Kalman filtering to track and vertex fitting”. *Nucl. Instrum. Meth.* A262 (1987), pp. 444–450. DOI: 10.1016/0168-9002(87)90887-4.
- [95] W. Adam et al. “Reconstruction of electrons with the Gaussian-sum filter in the CMS tracker at the LHC”. *Journal of Physics G Nuclear Physics* 31 (Sept. 2005), p. 9. DOI: 10.1088/0954-3899/31/9/N01.
- [96] CMS Collaboration. *Electron reconstruction and identification at $\sqrt{s} = 7$ TeV*. Tech. rep. CMS-PAS-EGM-10-004. <http://cds.cern.ch/record/1299116>. Geneva: CERN, 2010.
- [97] S. Baffioni et al. “Electron reconstruction in CMS”. *Eur.Phys.J.* C49 (2007), pp. 1099–1116. DOI: 10.1140/epjc/s10052-006-0175-5.
- [98] CMS Collaboration. *Particle-Flow Event Reconstruction in CMS and Performance for Jets, Taus, and MET*. Tech. rep. CMS-PAS-PFT-09-001. <http://cds.cern.ch/record/1194487>. 2009. Geneva: CERN, 2009.
- [99] CMS Collaboration. *Commissioning of the Particle-Flow reconstruction in Minimum-Bias and Jet Events from pp Collisions at 7 TeV*. Tech. rep. CMS-PAS-PFT-10-002. <http://cds.cern.ch/record/1279341>. Geneva: CERN, 2010.
- [100] Matteo Cacciari, Gavin P. Salam, and Gregory Soyez. “The anti- k_t jet clustering algorithm”. *Journal of High Energy Physics* 2008.04 (2008), p. 063. DOI: 10.1088/1126-6708/2008/04/063.
- [101] The CMS Collaboration. *Plans for Jet Energy Corrections at CMS*. Tech. rep. CMS-PAS-JME-07-002. <http://cds.cern.ch/record/1194485>. 2008. Geneva: CERN, 2008.
- [102] CMS Collaboration. “Determination of Jet Energy Calibration and Transverse Momentum Resolution in CMS”. *JINST* 6 (2011), P11002. DOI: 10.1088/1748-0221/6/11/P11002.
- [103] Christian Weiser. *A Combined Secondary Vertex Based B-Tagging Algorithm in CMS*. Tech. rep. CMS-NOTE-2006-014. <http://cds.cern.ch/record/927399>. Geneva: CERN, 2006.
- [104] The CMS Collaboration. *Algorithms for b Jet identification in CMS*. Tech. rep. CMS-PAS-BTV-09-001. <http://cds.cern.ch/record/1194494>. 2009. Geneva: CERN, 2009.
- [105] The CMS collaboration. “Identification of b-quark jets with the CMS experiment”. *Journal of Instrumentation* 8.04 (2013), P04013. DOI: 10.1088/1748-0221/8/04/P04013.
- [106] CMS Collaboration. “Missing transverse energy performance of the CMS detector”. *Journal of Instrumentation* 6 (Sept. 2011), p. 9001. DOI: 10.1088/1748-0221/6/09/P09001.

- [107] CMS Collaboration. *Commissioning of the Particle-flow Event Reconstruction with the first LHC collisions recorded in the CMS detector*. Tech. rep. CMS-PAS-PFT-10-001. <http://cds.cern.ch/record/1247373>. 2010.
- [108] CMS Collaboration. *Particle-flow commissioning with muons and electrons from J/Ψ and W events at 7 TeV*. Tech. rep. CMS-PAS-PFT-10-003. <http://cds.cern.ch/record/1279347>. 2010. Geneva: CERN, 2010.
- [109] The CMS Collaboration. “EGamma Group: Conversion Rejection” (). <https://twiki.cern.ch/twiki/bin/view/CMS/ConversionBackgroundRejection>.
- [110] W. Andrews et al. “Study of photon conversion rejection at CMS”. *CMS Analysis Note* CMS AN-2009-159 (2010). http://cms.cern.ch/iCMS/jsp/openfile.jsp?tp=draft&files=AN2009_159_v4.pdf.
- [111] CMS Collaboration. *Performance of the b -jet identification in CMS*. Tech. rep. CMS-PAS-BTV-11-001. <http://cds.cern.ch/record/1366061>. Geneva: CERN, 2011.
- [112] CMS Collaboration. “Measurement of differential top-quark-pair production cross sections in pp collisions at $\sqrt{s} = 7$ TeV”. *The European Physical Journal C* 73.3 (2013). DOI: 10.1140/epjc/s10052-013-2339-4.
- [113] The CMS Collaboration. “Pile-up Monte Carlo Reweighting Utilities” (). <https://twiki.cern.ch/twiki/bin/view/CMS/PileupMCReweightingUtilities>.
- [114] Serguei Chatrchyan et al. “Measurement of the Inclusive W and Z Production Cross Sections in pp Collisions at $\sqrt{s} = 7$ TeV”. *JHEP* 1110 (2011), p. 132. DOI: 10.1007/JHEP10(2011)132.
- [115] CMS Collaboration. “Measurement of the Drell-Yan cross section in pp collisions at $\sqrt{s} = 7$ TeV”. *Journal of High Energy Physics* 10, 7 (Oct. 2011), p. 7. DOI: 10.1007/JHEP10(2011)007.
- [116] Andrews et al., W. “A method to measure the contribution of $DY \rightarrow ll$ to a dilepton + MET selection.” *CMS AN-2009/023* (2009).
- [117] Wouter Verkerke and David P. Kirkby. “The RooFit toolkit for data modeling”. *eConf* C0303241 (2003), MOLT007. arXiv: physics/0306116 [physics.data-an].
- [118] CMS Collaboration. “Search for new physics with same-sign isolated dilepton events with jets and missing transverse energy at the LHC”. *Journal of High Energy Physics* 6, 77 (June 2011), p. 77. DOI: 10.1007/JHEP06(2011)077.
- [119] Vardan Khachatryan et al. “First Measurement of the Cross Section for Top-Quark Pair Production in Proton-Proton Collisions at $\sqrt{s} = 7$ TeV”. *Phys.Lett. B* 695 (2011), pp. 424–443. DOI: 10.1016/j.physletb.2010.11.058.
- [120] CMS Collaboration. *Performance of Methods for Data-Driven Background Estimation in SUSY Searches*. Tech. rep. CMS-PAS-SUS-10-001. <http://cds.cern.ch/record/1279147>. 2010. Geneva: CERN, 2010.

- [121] I. Antcheva et al. “ROOT: A C++ framework for petabyte data storage, statistical analysis and visualization”. *Comput.Phys.Commun.* 180 (2009), pp. 2499–2512. DOI: 10.1016/j.cpc.2009.08.005.
- [122] Volker Blobel and Erich Lohrmann. *Statistische und numerische Methoden der Datenanalyse*. 1st ed. Teubner Verlag, 1998. ISBN: 3519032430.
- [123] F. James and M. Roos. “Minuit: A System for Function Minimization and Analysis of the Parameter Errors and Correlations”. *Comput.Phys.Commun.* 10 (1975), pp. 343–367. DOI: 10.1016/0010-4655(75)90039-9.
- [124] P. de Buyl and N. Varoquaux. “Proceedings of the 6th European Conference on Python in Science (EuroSciPy 2013)”. *ArXiv e-prints* (May 2014). arXiv: 1405.0166 [cs.PL].
- [125] Jorge J. More, Burton S. Garbow, and Kenneth E. Hillstom. “User Guide for Minpack-1” (1980).
- [126] Felix Höhle. “Measurement of Spin Correlations in Top Pair Events in the Dilepton Channels in pp Collisions at 7 TeV”. *J.Phys.Conf.Ser.* 452.1 (2013), p. 012049. DOI: 10.1088/1742-6596/452/1/012049.
- [127] CMS Collaboration. *Measurement of Spin Correlations in $t\bar{t}$ production*. Tech. rep. CMS-PAS-TOP-12-004. Geneva: CERN, 2012.
- [128] The CMS Collaboration. *Pileup Systematic Errors*. Tech. rep. <https://twiki.cern.ch/twiki/bin/viewauth/CMS/PileupSystematicErrors>. CERN.
- [129] CMS Collaboration. “Measurement of the inelastic proton-proton cross section at $\sqrt{s} = 7$ TeV”. *Phys.Lett.* B722 (2013), pp. 5–27. DOI: 10.1016/j.physletb.2013.03.024.
- [130] M. Botje et al. “The PDF4LHC Working Group Interim Recommendations”. *ArXiv e-prints* (Jan. 2011). arXiv:1101.0538. arXiv: 1101.0538 [hep-ph].
- [131] Hung-Liang Lai et al. “Uncertainty induced by QCD coupling in the CTEQ global analysis of parton distributions”. *Phys. Rev. D* 82 (5 2010), p. 054021. DOI: 10.1103/PhysRevD.82.054021.
- [132] Georges Aad et al. “Measurement of τ polarization in $W^- \rightarrow \tau\nu$ decays with the ATLAS detector in pp collisions at $\sqrt{s} = 7$ TeV”. *Eur.Phys.J.* C72 (2012), p. 2062. DOI: 10.1140/epjc/s10052-012-2062-6.
- [133] A. Stahl. “Physics with Tau Leptons”. *Tracts in Modern Physics* (2000). DOI: 10.1007/BFb0109618.
- [134] Kaoru Hagiwara, Alan D. Martin, and D. Zeppenfeld. “Tau Polarization Measurements at LEP and SLC”. *Phys.Lett.* B235 (1990), pp. 198–202. DOI: 10.1016/0370-2693(90)90120-U.
- [135] Andre Rouge. “Polarization observables in the 3 pi neutrino decay mode”. *Z.Phys.* C48 (1990), pp. 75–78. DOI: 10.1007/BF01565607.

- [136] The CMS Collaboration. “Data Data Certification” (). <https://cms-service-dqm.web.cern.ch/cms-service-dqm/CAF/certification/Collisions11/>.
- [137] The CMS Collaboration. *Data Aggregation System*. <https://cmsweb.cern.ch/das/>.
- [138] Ryan Gavin et al. “FEWZ 2.0: A code for hadronic Z production at next-to-next-to-leading order”. *Comput.Phys.Commun.* 182 (2011), pp. 2388–2403. DOI: 10.1016/j.cpc.2011.06.008.
- [139] John M. Campbell and R.K. Ellis. “MCFM for the Tevatron and the LHC”. *Nucl.Phys.Proc.Suppl.* 205-206 (2010), pp. 10–15. DOI: 10.1016/j.nuclphysbps.2010.08.011.

Abbreviations

BPIX	barrel pixel
BSM	beyond the Standard Model
CDF	Collider Detector at Fermilab
CKM	Cabibbo-Kobayashi-Maskawa
CMS	Compact Muon Solenoid
CSC	Cathode strip chambers
CSV	Combined Secondary Vertex
CSVL	loose working point
D0	DZero
DT	Drift tube
DY	Drell-Yan
ECAL	electromagnetic calorimeter
FPIX	forward pixel
FSR	final state radiation
GEN	generation
GSF	Gaussian Sum Filter
HB	barrel hadron
HCAL	hadronic calorimeter
HE	end-cap hadron
HF	hadron forward
HLT	High Level Trigger

HO	hadron outer
ISR	initial state radiation
JER	jet energy resolution
JES	jet energy scale
JSON	JavaScript Object Notation
L1	Level 1
LEP	Large Electron Positron
LHC	Large Hadron Collider
LHCf	LHC forward
LHE	Les Houches Event
Linac2	Linear Accelerator 2
LO	leading order
MC	Monte Carlo
ME	Matrix element
MET	Missing transverse energy
MNS	Maki-Nakagawa-Sakata
NLO	next-to-leading order
PDF	parton density function
PFLOW	particle flow algorithm
PS	Proton Synchrotron
PSB	Proton Synchrotron Booster
PU	pile-up
PVT	Physics Validation Team
RPC	resistive plate chambers
SM	Standard Model
SPS	Super Proton Synchrotron
TEC	Tracker End-cap

TIB	Tracker Inner Barrel
TID	Tracker Inner Discs
TOB	Tracker Outer Barrel
TOTEM	Total Elastic and Diffractive Cross Section Measurement